Magnetic and Electrostatic Interactions of Colloids and Polyelectrolytes

Inaugural–Dissertation
zur
Erlangung des Doktorgrades der
Mathematisch-Naturwissenschaftlichen Fakultät
der Heinrich-Heine-Universität Düsseldorf

vorgelegt von

NORMAN HOFFMANN

aus Lich

Düsseldorf, Dezember 2006

Aus dem Institut für Theoretische Physik II
der Heinrich-Heine Universität Düsseldorf

Gedruckt mit Genehmigung der
Mathematisch-Naturwissenschaftlichen Fakultät
der Heinrich-Heine-Universität Düsseldorf

Referent: Prof. Dr. C. N. Likos
Koreferent: Prof. Dr. H. Löwen

Tag der mündlichen Prüfung: im Januar 2007

This thesis is based on the following original papers:

Chapter 2 –

N. Hoffmann, C. N. Likos, and H. Löwen,
Microphase structuring in two-dimensional magnetic colloid mixtures,
J. Phys.: Condens. Matter **18**, 10193 (2006).

Chapter 3 –

H. Löwen, R. Messina, N. Hoffmann, C. N. Likos, C. Eisenmann, P. Keim, U. Gasser, G. Maret, R. Goldberg, and T. Palberg,
Colloidal layers in magnetic fields and under shear flow,
J. Phys.: Condens. Matter **17**, S3379 (2005).

N. Hoffmann, F. Ebert, C. N. Likos, H. Löwen, and G. Maret,
Partial Clustering in Binary Two-Dimensional Colloidal Suspensions,
Phys. Rev. Lett. **97**, 078301 (2006).

N. Hoffmann, C. N. Likos, and H. Löwen,
Microphase structuring in two-dimensional magnetic colloidal mixtures,
J. Phys.: Condens. Matter **18**, 10193 (2006).

Chapter 4 –

N. Hoffmann, C. N. Likos, and H. Löwen,
Pair correlations for anisotropic interactions,
(in preparation) (2006).

Chapter 5 –

N. Hoffmann, C. N. Likos, and J.-P. Hansen,
Linear screening of the electrostatic potential around spherical particles with non-spherical charge patterns,
Mol. Phys. **102**, 857 (2004).

Chapter 6 –

N. Hoffmann, and P. A. Pincus,
Multivalent counterion-condensation-induced collapse of end-grafted polyelectrolyte chains,
(in preparation) (2006).

Abstract

This thesis regards electrostatic and magnetic interactions in soft matter. There are three different parts.

First, we examine a strongly interacting binary mixture of superparamagnetic colloidal particles confined to a two-dimensional water-air interface. We employ liquid integral equation theory and computer simulation to investigate this system. This mixture exhibits, at equilibrium, a partial clustering. In the voids of a matrix of unclustered big particles, small particles form subclusters that are topologically sponge-like accompanied by a characteristic small-wave vector peak in the small-small structure factor. We investigate this pattern formation using tools from integral geometry, namely the Euler characteristic. The clustering behavior is ultimately a non-additive property of the system, stemming from the cross-interaction that is less repulsive than the direct interactions. We confirm these theoretical findings by confronting them to direct experimental data. Furthermore, we study the simpler one-component system of superparamagnetic particles in a tilted magnetic field. The particles align with the in-plane component of the magnetic field. The local ordering of the particles becomes more inhomogeneous with increasing tilt angle.

Second, by simplifying proteins as spherical particles with non-spherical charge patterns, we calculated their associated electrostatic potential. We derive analytical expressions for the screened electrostatic potential caused by a charged spherical colloid that contains point charges distributed in an arbitrary manner in its interior. We consider two cases: that of uniform and discontinuous dielectric media. The solution is based on an expansion of the electrostatic potentials on the various regions of space in spherical harmonics involving spherical Bessel functions of the third kind. Tetrahedral charge arrangements as well as a random charge distribution inside the confining sphere are considered explicitly as representative examples.

Last, we investigate polyelectrolyte chains end-grafted to a planar surface in the presence of multivalent counterions. Our theory is based on a variational free energy that is written as a sum of electrostatic, polymer, and entropic contributions. We minimize the free energy with respect to the chain length and the number of counterions in order to obtain the ground state. We observe a shrinking of the chain length with increasing electrostatic attraction of the monomeric units finally resulting into a collapsed state reminiscent of a first-order phase transition.

Zusammenfassung

Die vorliegende Doktorarbeit beschäftigt sich mit magnetischen und elektrostatischen Wechselwirkungen auf dem Gebiet der Weichen Matetrie. Die Doktorarbeit beinhaltet im wesentlichen drei Hauptprojekte.

Zuerst haben wir die Wechselwirkung von Mischungen aus superparamagnetischen Kolloiden unter dem Einfluß eines äußeren Magnetfeldes untersucht. Die Partikel können sich in einer zweidimensionalen Ebene frei bewegen und das Feld ist senkrecht zu dieser gerichtet. Die kleinen Teilchen formen Aggregate in den Zwischenräumen der großen Teilchen. Dies konnte durch einen zusätzlichen Peak im Strukturfaktor bei kleinen Wellenlängen beobachtet werden. Eine genaure Analyse mit Hilfe der Eulercharakteristik zeigt, daßdie kleinen Teilchen ein schwammartiges Muster bilden. Ein quantitativer Vergleich mit experimentellen Daten zeigt hervorragende Übereinstimmung mit unseren theoretischen Resultaten. Weiterhin haben wir das einkomponentige System bei geneigtem Magnetfeld untersucht. Die beobachtete Struktur ist in diesem Falle inhomogen und die Teilchen bevorzugen eine Ausrichtung in Richtung der Projektion des Magetfeldes auf die Ebene.

In dem zweiten Projekt haben wir das elektrostatische Potential von Proteinen berechnet, welche wir als sphärische Objekte mit einer nicht-sphärischen Ladungsverteilung modelliert haben. Wir konnten analytische Ausdrücke für das abgeschirmte Potential eines sphärischen Kolloids mit asymmetrischer Ladungsverteilung angeben. Die Lösung basiert auf einer Entwicklung des Potentials in sphärische Besselfunktionen der dritten Art. Tetraedische und zufällige Ladungsverteilungen dienen als direkte Anwendung unserer theoretisch abgeleiteten Ergebnisse.

Zuletzt haben wir Polyelektrolytketten untersucht, welche mit einem Ende an einer Wand befestigt sind. Die Gegenionen sind ausschießlich multivalent. Unsere Theorie basiert auf der Minimierung der Freien Energie des Systems, welche aus *polymeric*, elektrostatischen und entropischen Beiträgen besteht. Wir beobachten ein Schrumpfen der Kettenlänge mit wachsender anziehender Wechselwirkung der Monomore. Dies resultiert in einem Kollaps der Ketten, welcher an einen Phasenübergang erster Ordung erinnert.

Contents

Chapter 1

Introduction

The topic of the thesis at hand can be integrated into the overall context of *soft matter* [1–3]. The latter expression refers to a variety of different composites ranging from proteins, polymers, micelles, microemulsions, surfactants, membranes, dendrimers to colloids. These are all soft matter systems that have length scales between 1nm and several μm, categorizing them as *complex fluids.* Representative constituents of these systems are molecular aggregates in contrast to atomic systems. These are coarse-grained systems, and it is assumed the underlying microscopic basic units no longer play a crucial, physical role. Supposed we observe a system by a microscope of 10 Angstrøm resolution. For a atomic (molecular) system whose constituents have the spatial extent of just a few (less than 10) Angstrøm, the material looks completely homogeneous. We encounter a totally different situation for a soft matter system. In contrast to the former system its constituents are mostly still visible and the structure appears inhomogeneously.

Coarse-graining can be visualized observing just major ingredients instead of realizing every detail. For example, imagine the situation that you attend a play and that you got tickets for the first row. This location allows you to discern every single move of the actors: their facial expressions, and gestures. You may get a much better understanding of the story line by sitting close to the stage perceiving the emotional expression of the protagonists. In this case, the details of the motion in short length- and time-scales are relevant and the loss of discernment would be tremendous by taking a back row seat and perceiving the actors just as a diffuse ensemble. On the other hand, consider the opening of the Olympic Games. You do not gain much by occupying first row seats. On the contrary, a much better overview is captured by a more distant placement. You can enjoy that gala much more by perceiving the athletes as a group representing their country. The interplay of these national groups are more important than the movement of every single individual. In this case, you are more interested in the shape and pattern formations of each different group as a whole than in the movements of every single participant. The time scale for a performer to move his limbs is irrelevant. You do not pay attention to the athlete's behavior as an individual but to the groups' collective motion. The same holds for the short time length scales. They do not matter in the order of a human body dimension [4].

Soft matter systems exhibit a complexity of time and length scales. For example, complex fluids may be composed of larger particles dissolved in a atomic or molecular solvent. The solvent particles are much smaller and much faster than the solute. If you are just interested in the behavior of the larger (mesoscopic) aggregates, the short time and length scales are irrelevant. Therefore, an adequate description of the system might be to eliminate them. This elimination or *coarse graining* has its roots at the McMillan-Mayer [5] theory of solutions and its formulation by Kirkwood and Buff [6]. An application to colloids is given in a review article by van Megen and Snook [7]. *Coarse graining* also introduces the concept of *effective interactions* that encapsulates the atomic scale physics. A detailed, statistical derivation of these concepts and their implications can be found in Ref. [8]. This procedure bridges the gap between the microscopic and the mesoscopic regime, and the transition from the latter to the macroscopic realm can be performed by standard tools of statistical mechanics.

A decisive distinction of soft matter systems compared to their atomic or molecular counterparts is their striking low shear modulus. This property allows us to deform soft matter materials easily by applying a relatively low shear stress whereas molecular system substances such as metal bars require a substantial force to be bent. The key for understanding of that phenomenon lies in the different length scales of the crystal forming particles. The shear modulus scales with the ratio of the typical energy involved and the inverse volume of the elementary cell. Assuming the typical energy is of the order of the thermal energy for both, the complex as well as the atomic (molecular) system, the difference of the length scales amounts to the different softness of both systems. The size of ordinary molecules is typically of the order of Angstrøm which is a factor 10^4 smaller than the particles in the soft matter system, thus leading to shear modulus that is about 12 orders of magnitude smaller than that of usual crystals. Therefore complex fluids are extremely soft and can be destroyed by mechanical means very easily. This property which is intrinsic for the aforementioned underlying length scale accounts for embracing all these materials as soft matter. There are, of course, other states of matter than the solid one for soft matter systems. In that cases the softness can be understood in terms of a very low density of the system.

A remarkable aspect of soft matter lies in the fact that the interaction between the particles can be tailored in a controlled way. While for atomic systems the interaction between the particles is nature-given, mostly dictated by their electronic structure, the interaction potential of colloidal particles can almost be chosen at will, ranging from short ranged attraction to long ranged repulsion. That characteristic of soft matter systems renders them as perfect model systems to theory as well as experiment. Thus, they represent an ideal test bed for verifying theoretical models by direct experimental measurements. Soft matter systems can be studied simultaneously by using three different complementary approaches

(i) Developing accurate model systems appears a major challenge from a theoretical point of view. These model systems are further investigated by approved theoretical tools such as *density functional theory* or *liquid integral equation theory*. We especially make extensive use of the latter to explore the structure of our systems to be investigated.

(i) Due to the mesoscopic range of the involved length scales, real space analysis of the experimental setup turns out to be an excellent tool in understanding complex fluids. In the course of this thesis we consistently check some of our results to experimental data confirming the correctness of our theoretical model.

(iii) Further insight can be gained by performing simulations to test the validity and accuracy of the theory. To this end we have carried out *Brownian dynamics simulations*.

Apart from a purely theoretical interest in soft matter there are many technical, food technological, pharmaceutical and biological applications including paint, ink, detergents, adhesives, drilling fluids, lubricants, milk, mayonnaise, blood, viruses, drug delivery into cells, trans-cell-membrane transport, protein crystallization and DNA recognition [1,9–12]. Due to the abundance of industrial products in daily life, there is a urgent need for understanding the mechanism by which the mutual interplay of the particles influences the macroscopic properties of soft matter systems.
The thesis at hand deals primarily with colloidal dispersions. The term *colloid* has been used up to now without further specification. In the literature the expression *colloidal dispersions* often refers to soft matter systems synonymously. We understand by *colloidal dispersions* mesoscopic solid particles with a stable core dissolved in a molecular solvent. The term *colloid* has been introduced by Graham Thomas in the year 1861 which marks the beginning of the systematic research on colloidal systems. Graham observed two different kinds of solutions. He distinguished them by the characteristic of the dissolved species to diffuse through a membrane. Graham named dissolved particles that did not diffuse through the membrane colloids. The term colloid derives from the Greek words $\kappa\grave{o}\lambda\lambda\alpha$ (glue) and $\epsilon\grave{\iota}\delta$os (kind) and was coined by Graham as well. Nowadays colloids are strictly defined by their spatial extent. We call a particle with size within a certain range from 1nm up to several μm a colloid. A detailed knowledge of the internal degrees of freedom is not needed. That does not mean that the chemical structure of the constituent atoms

or molecules is irrelevant, but in order to describe a colloid we do not need the microscopic arrangement of these constituents. Many properties of colloidal system can be extracted without knowing the specific microscopic structure. Due to the specific size range, colloidal particles exhibit thermal motion which is commonly referred to as *Brownian motion* and was discovered by R. Brown in 1827. That irregular motion comes about by random collisions of the solvent molecules with the colloidal particles. Therefore colloidal particles are often referred to as *Brownian particles* [3, 8, 13].

In this thesis the focus lies on the theoretical investigation of three different physical systems. The first project deals with superparamagnetic colloids in an external magnetic field. In the second project, we extend the well-known DLVO theory to asymmetric charge patterns. The last project investigates polyelectrolyte chains end-grafted to a planar surface.

In the first project we analyze from a theoretical point of view the correlations and structure of superparamagnetic colloids exposed to an external magnetic field. Spherical colloids are confined by gravity to a water-air interface formed by a cylindrical drop suspended by surface tension in a top-sealed ring. Their movement takes place almost exclusively in that planar surface and the setup can therefore be regarded as a nearly ideal two-dimensional system. The external magnetic field induces magnetic dipoles onto the particles along its direction, whose strength can be controlled by the amplitude of the external field. By tilting that field starting from a alignment perpendicular to the surface, the mutual interplay between the colloids can be tuned from a purely repulsive interaction to an attractive one appearing beyond a certain threshold angle. The particles are superparamagnetic due to their doping with Fe_2O_3, *i.e.* for a sufficient strong field the magnetic moments align perfectly along the external magnetic field and any thermal fluctuations can be neglected. The colloids' movements can be observed in the experiment by video microscopy allowing thereby to confront our theoretical findings with direct experimental data.

The above described system has been extensively studied under a variety of theoretical and experimental aspects different from those we address to.

The one-component system of almost monodisperse particles has been extensively studied in the past by Maret and coworkers. The experimental setup has been used to determine elastic moduli of two-dimensional colloidal crystals [14, 15] and has turned out to be an ideal check for verifying th KTHNY theory [16]. The measurement of Young's modulus is in perfect agreement with the theoretical prediction. Furthermore the successive transition from the solid to the liquid phase with an intermediate hexatic phase has been observed experimentally by tilting the external field [17–19]. That melting transition has been analyzed on the basis of long-time behavior of a modified Lindemann parameter and the bond-angular correlation function [20]. The system has been proven apt to study the influence of hydrodynamic interactions on self-diffusion. The diffusion is enhanced by explicitly including hydrodynamic interactions [21, 22]. Only recently two-component mixtures were investigated. The amorphous solid state of the system has been studied lately [23]. The close similarity of the partial pair-distribution functions, mean-square displacements as well as self-intermediate scattering functions with those of 3d glass formers indicates that our 2d colloidal system at hand can be considered as a typical glass former [24, 25].

Additionally static and diffusional properties of the strongly asymmetric binary mixture have been investigated by theory and experiment. By tilting the external field a non-isotropic interaction between the particles is induced leading to unusual features in the partial pair distribution functions, and to significantly enhanced tracer-diffusion [26]. Combining theoretical and experimental work, it is found that the anisotropy of the mean-square displacement behaves non-monotonically as a function of the tilt angle and does not correlate with the structural anisotropy of the crystal [27]. On the theoretical level, a phase diagram at zero temperature has been calculated by varying the tilt angle, the colloidal density, and the strength of the magnetic field. A host of stable crystal lattices has been found [28].

Despite of all these earlier findings, there is a richness of features for the system at hand yet to be explored. We are especially interested in the structural behavior of the binary mixture by varying the field strength, the susceptibility ratio as well as density ratio of the two species. Due to the negative non-additivity of the mixture, we expect a partial clustering of the species of lower susceptibility. A very colorful situation helps to understand that phenomenon. Imagine a certain number of human beings and mice enclosed together in a locked room. The small mice are scared to death from the much bigger human beings that themselves dislike the animals. Due to the innate aloof demeanor of the human beings to their own species, they try to keep away from each other as far as possible. The mice fearing the human beings much more than their fellows try to maximize the distance to the men by huddling together in smaller groups.

When dealing with the real physical system, we face a similar situation. The particles with lower susceptibility form cluster in the voids of the matrix of the unclustered particles with higher susceptibility. Our motivation for studying the cluster behavior of binary mixtures is twofold. First, any realistic sample consists of several components and hence considering a binary mixture is an important step towards a control of composite materials. Second, and more fundamentally, mixtures exhibit much richer behavior than their one-component counterparts in general. Thus, there is need to explore whether and how the scenario of equilibrium clustering occurs in two-component systems. The cluster formation of colloidal systems has recently attracted great deal of interest. The work of Likos *et al.* [29] on purely repulsive soft spheres marks a milestone in soft matter physics. For the first time stable cluster solids have been observed by means of a density functional theory and advanced

Monte Carlo simulations. That scientific achievement has evoked great attention in the scientific world [30] as well as in the broad public [31]. For further reference on clusters, we direct the reader to chapter 3.

The second coherent part of that thesis focuses on the modeling of the electrostatic interaction of proteins by colloidal spheres with asymmetric charge patterns.

Proteins are biological macromolecules. They are assembled from a sequence of amino acids with DNA and RNA as their most prominent representatives and play a crucial role in all biological processes of our body. They assume a variety of diverse functions in bodily activities such as the regulation of cellular processes, immune protection against diseases, enzymatic catalysis, growth control, cell differentiation, transport and storage of other substances. Thus, there is a profound interest in understanding of the mechanisms by which proteins interact with each other.

For the sake of simplicity, we model the proteins as globular objects with a certain charge distribution. The Derjaguin-Verwey-Landau-Overbeek (DLVO) theory proves as a reliable concept to incorporate electrostatic interactions for colloidal dispersions. Charged colloids dispersed in a fluid solvent repel each other. Due to the presence of the free ions, the pair-interaction potential is not a pure Coulomb repulsion, but screened to some extent by the ions. A negatively charged macroion expels oppositely charged ions while ions with positive charge are attracted to it. By that mechanism a charge distribution is formed around the colloidal particle, the so-called *double layer*, which partly screens the bare charge. The asymptotic form of the pair-interaction for large distances, where the potential energy is not too large, is a screened Coulomb potential, or equivalently, a *Yukawa potential* taking the form $\exp(-\kappa r)/r$. κ^{-1} is the so-called screening length and measures the extent of the aforementioned double layer. For larger potential energies the potential is a much more complicated function of the distance. The DLVO theory includes van der Waals as well as electrostatic interaction contributions to the overall potential [13]. The assumption in DLVO theory of a uniformly distributed surface charge is reasonable on the colloidal scale in view of highly charged colloids resulting from typical surface charges of up to an elementary charge per nm^2. This is no longer true when one turns to the nanometer scale relevant for most biomolecules. Therefore, we extend the DLVO theory to asymmetric charge patterns holding for particles on length scales smaller than the mesoscopic one. We perform the derivation of the potential in the realm of *linearized Poisson-Boltzmann theory.*

The third project deals with polyelectrolyte brushes. When a polymer chain with ionizable groups is immersed in a polar solvent, these groups dissociate into the solvent. They leave behind an equally, but oppositely charged backbone which is called polyelectrolyte (PE). A PE brush consists of a high density of charged polymers grafted on a planar or curved surface. The end-grafting is achieved either by covalently binding end groups or block copolymers. The high grafting density guarantees a strong interaction between neighboring chains.

Because of their technological applications, such as enhanced stabilization against colloidal flocculation, PE brushes have attracted a great deal of attention by theory [32–41] as well as by experiment [42–45]. Charge stabilization turns out to be quite sensitive to dissolved salts or other electrolytes and can lead to a break-down of the stabilization effect in these cases. Therefore, there is an increasing interest in steric stabilization sustained by PE brushes.

Recently a collapse transition of spherical PE brushes in the presence of multivalent counterions has been found by experiment and simulation [46]. Initiated by this finding, we investigate theoretically PE brushes end-grafted to a planar surface in the presence of multivalent counterions. Our theory is based on a variational free energy consisting of electrostatic, polymer, and entropic contributions. While the polymer and entropic contributions are identical to the case of neutral chains, the electrostatic interaction poses an intricate and complex problem. We address it by the use of Poisson-Boltzmann theory. The existence of multivalent counterions induces an attraction between neighboring chains. This *bridging* effect is described by a simple mean-field term. We observe a shrinking of the chain length with increasing electrostatic attraction of the monomeric units resulting finally into a collapsed state reminiscent of a first-order phase transition in agreement with previous results [47].

The rest of the thesis is organized as follows: in chapter 2 we introduce the model of superparamagnetic particles in a magnetic external field. Standard tools for the further investigation of the system, specifically liquid integral equation theory and Brownian dynamics simulations are presented. The external field is aligned perpendicular to the confining surface. A first application to the one-component system is performed, primarily to get familiar with the system as well as the tools and check their accuracy.

In chapter 3 we extend the methods presented in the preceding section to the two-component system and compare our findings to experimental results. The clustering of species is found by theory, simulation as well as experiment and is further investigated by a topological analysis.

In chapter 4 we tilt the external field with respect to the confining plane and explore correlations between the particles by means of the radial distribution function.

In chapter 5 we calculate the electrostatic potential around colloidal spheres with non-spherical charge patterns in the regime of linearized Poisson-Boltzmann theory.

In chapter 6 we theoretically investigate the collapse transition of end-grafted PE brushes in the presence of multi-valent counterions.

Chapter 7 gives a brief summary of the main accomplishments and discusses possible extensions of this work for future investigations.

We present each chapter in a more or less self-contained manner facilitating the reader to focus on specific sections without additional knowledge of the other parts. Therefore, we precede each chapter with a general introductory part. The theoretical model for the superparamagnetic particles is however presented once and for all in chapter 2.

Chapter 2

One-component Superparamagnetic Colloids

In this chapter we introduce the model for two-dimensional superparamagnetic colloids exposed to an external magnetic field. We shortly review the basics of liquid integral equation theory. Then, we compare results obtained by that theory to those of Brownian dynamics simulations. The good agreement between Brownian dynamics simulation and the Rogers-Young closure singles out the latter as an appropriate tool for the further investigation of the system at hand.

2.1 The theoretical model

We consider a two-dimensional system of superparamagnetic colloidal particles that are confined to a planar water-air interface and exposed to an external magnetic field perpendicular to the interface (see fig. (2.1)). The magnetic field induces a magnetic dipole moment onto the particles, resulting into an effective repulsion between all parallely oriented dipole moments, which scales with the inverse cube of the particle distance. This system enables a direct comparison between theories and computer simulations based on a pairwise dipole-dipole interaction potential and renders these suspensions into an ideal model system [21], allowing thereby to additionally confront the theoretical findings with direct experimental data.

More specifically, we consider a two-dimensional system of N colloidal particles in a plane of surface area A. With $\rho = N/A$ denoting the area density of the particles, we introduce the average interparticle distance $a \equiv 1/\sqrt{\rho}$ as a characteristic length scale of the system. The motion of the particles is confined by a water-air interface wherein they can move freely. We expose the system to an external static magnetic field $\mathbf{B_0}$ that induces on each particle a magnetic moment $\mathbf{m}$. We restrict ourselves to the case of a magnetic field perpendicular to the plane. The particles are assumed

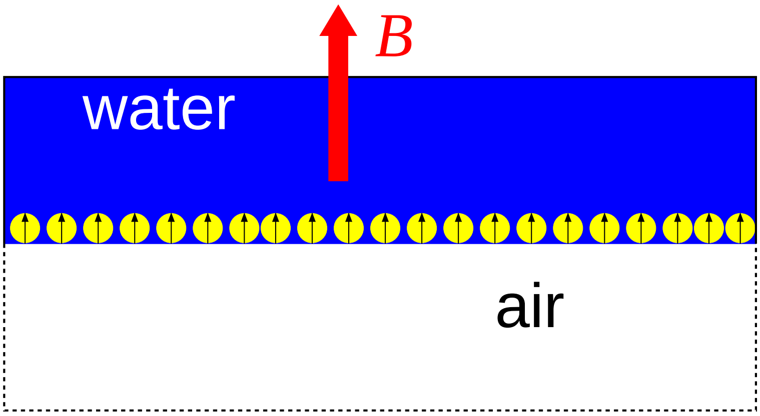

Figure 2.1: Sketch of the set-up. Superparamagnetic particles are confined to an air-water interface. The external magnetic field acting perpendicular to the surface induces a magnetic moment onto each particle.

to be superparamagnetic, *i.e.*, the magnetic dipole of each particle aligns perfectly with the external field and any fluctuations due to thermal motion can be neglected. Thus, it holds

$$\mathbf{m} = \chi \mathbf{B_0}, \tag{2.1}$$

whereas the proportionality constant χ is the particles' magnetic susceptibility. For the system at hand, the dipole-dipole interaction between two particles with dipole moments $\mathbf{m}_i = \chi \mathbf{B_0}$ and coordinates $\mathbf{r}_i$, $i = 1, 2$, respectively, reads as [28, 48][1]

$$u(\mathbf{r}_1, \mathbf{r}_2) = \frac{(\chi B_0)^2}{|\mathbf{r}_1 - \mathbf{r}_2|^3}(1 - 3\sin^2\omega\cos^2\theta), \tag{2.2}$$

where ω is the angle between the field and the normal vector of the confining plane and θ the angle between $\mathbf{m}_i$ and the direction of the connecting vector, $(\mathbf{r}_1 - \mathbf{r}_2)$. For the case at hand (perpendicular field), we have $\omega = 0$ and $\theta = \pi/2$, thus eq. (2.2) simplifies into

$$u(r) = \frac{(\chi B_0)^2}{r^3}, \tag{2.3}$$

where $r = |\mathbf{r}_1 - \mathbf{r}_2|$. For the purely repulsive potential at hand, the system is thermodynamically stable on the basis of the dipole-dipole interaction alone; an additional, short-range repulsion is not necessary to stabilize the system at the relevant experimental densities, as the typical interparticle distances are large enough (compared

---

[1] Eq. (2.2) above holds for two permanent magnetic dipoles. For two induced magnetic dipoles, the expression must be multiplied by a factor 1/2. We ignore this factor because it only leads to a trivial rescaling of the coupling strength Γ, see, e.g., Ref. [28].

to their physical size) and only the dipole-dipole interaction is felt.[2] Comparisons with experimental results [27, 49] fully support the above modeling of the interactions and confirm its realistic character. The particles are thus treated as point-like. Using the aforementioned length scale a, we introduce the dimensionless coupling strength Γ, defined as

$$\Gamma = \beta \frac{(\chi B_0)^2}{a^3}, \tag{2.4}$$

where $\beta = 1/(k_{\mathrm{B}}T)$, with k_{B} being Boltzmann's constant and T being the temperature. Clearly, Γ expresses the ratio of the kinetic versus the typical potential energy of a particle and allows for the distinction of the weak ($\Gamma \lesssim 1$), intermediate ($\Gamma \cong 1$) and strong ($\Gamma > 1$) regimes. Rescaling the particle coordinates with the interparticle distance, $\mathbf{r_i} \rightarrow \mathbf{x_i} \equiv \mathbf{r_i}/a$ and using eqs. (2.1) and (2.4), we can re-write the interaction potential, eq. (2.3), in the form:

$$\beta u(x) = \frac{\Gamma}{x^3}, \tag{2.5}$$

with $x = |\mathbf{x}_1 - \mathbf{x}_2|$. All structural and thermodynamic properties of such a system depend *solely* on the coupling strength Γ and *not* separately on temperature and density.

The system at hand presents a host of novel features: it is a two-dimensional system, it has clearly defined interactions between all its constituent particles, which take a simple form and are steered by a single and readily tunable external field; it is experimentally realizable and allows direct comparison with theory; and, finally, it is apt to direct visual observation. A detailed description of the experimental setup and references for further reading are given in chapter 3.

2.2 Basics of liquid integral equation theory

The overall goal of liquid integral equation theory is the determination of the pair structure of a uniform fluid. The following concepts presented in this section hold strictly only for homogeneous, isotropic and one-component systems. The one-particle density operator is defined as

$$\hat{\rho}(\mathbf{r}) = \sum_{i=1}^{N} \delta(\mathbf{r} - \mathbf{r}_i). \tag{2.6}$$

---

[2] The argument applies as long as the field does not deviate from the vertical direction by more than, roughly, 30°. In the contrary, dipole-dipole *attractions* that lead to chain formation arise and a short-range steric repulsion is necessary to stabilize the system [28].

The one-particle density can be expressed by the canonical ensemble average of the one-particle density operator

$$\rho = \langle \hat{\rho} \rangle = \frac{N}{\Omega}. \tag{2.7}$$

Thus, for a homogeneous and isotropic system the density ρ can be written as the ratio of particle number of the system and its volume Ω.
For theses system the two-particle density $\rho^{(2)}(\mathbf{r}_1, \mathbf{r}_2)$ is merely a function of the distance $|\mathbf{r}_1 - \mathbf{r}_2|$ of two particles

$$\rho^{(2)}(\mathbf{r}_1, \mathbf{r}_2) = \left\langle \sum_{i=1}^{N} \sum_{i \neq j=1}^{N} \delta(\mathbf{r}_1 - \mathbf{x}_i)\delta(\mathbf{r}_2 - \mathbf{x}_j) \right\rangle. \tag{2.8}$$

The product $\rho^{(2)}(|\mathbf{r}_1 - \mathbf{r}_2|)\mathrm{d}\mathbf{r}_1\mathrm{d}\mathbf{r}_2$ is proportional to the probability of finding one particle in the volume $[\mathbf{r}_1, \mathbf{r}_1 + \mathrm{d}\mathbf{r}_1]$ and the other in the volume $[\mathbf{r}_2, \mathbf{r}_2 + \mathrm{d}\mathbf{r}_2]$, irrespective of the positions of the remaining particles and irrespective of all momenta. The radial distribution function $g(\mathbf{r})$ plays a central role in physics of classical fluids and it is defined in terms of the two-particle density

$$\rho^{(2)}(|\mathbf{r}_1 - \mathbf{r}_2|) = \rho^2 g(|\mathbf{r}_1 - \mathbf{r}_2|). \tag{2.9}$$

It measures the extent to which the structure of the fluid deviates from complete randomness. Alternatively, it predicts the conditional probability of a particle at a distance r if an other particle is located at the origin. Its fundamental importance attributes not only to describe pair correlations, but also allows to calculate macroscopic thermodynamic properties such as the internal energy of the fluid or its pressure. Finally, the determination of the pair structure of a uniform fluid amounts to the calculation of the radial distribution function (rdf) $g(r)$ and the direct correlation function (dcf) $c(r)$. By introducing the total correlation function $h(r) = g(r) - 1$, the former two quantities are connected via the Ornstein-Zernike (OZ) relation [50]

$$h(r) = c(r) + \rho \int \mathrm{d}\mathbf{r}' c(|\mathbf{r} - \mathbf{r}'|)h(\mathbf{r}'). \tag{2.10}$$

The OZ relation is exact and couples two unknown functions via an integral equation. The physical interpretation of that relation can easily be understood. The total correlations between the positions of two particles is the sum of their direct correlation, due to their mutual interaction, and of indirect correlations mediated by other neighboring particles. These indirect correlations, involving one or several 'intermediate' particles, are embodied in the convolution term in eq. (2.10), which can be rewritten formally as

$$h = c + \rho c * c + \rho^2 c * c * c + \dots \tag{2.11}$$

At very low density the influence of the 'intermediate' particles can be neglected, so that $h(r) \simeq c(r)$, as implied by eq. (2.10) in the limit $\rho \to 0$. In this limit $h(r)$ reduces to the Mayer function $c_0(r)$

$$c_0(r) = \exp[-\beta u(r)] - 1, \tag{2.12}$$

whereas $u(r)$ denotes the pair potential. The key assumption is that the range of $c(r)$ remains the same, *i.e.*, equal to the range of $-\beta u(r)$ at all densities, while the range of the total correlation function $h(r)$ may increase dramatically near the critical point [52].

A second equation is required in order to determine these both unknown function $g(r)$ and $c(r)$. The radial distribution function can be expressed in terms of the direct correlation function, as

$$g(r) = \exp[-\beta u(r) + g(r) - 1 - c(r) + B(r)], \tag{2.13}$$

with $B(r)$ being the so-called bridge function. By introducing certain approximations for the bridge function, we supply an additional, approximate equation to the OZ relation. The former equation is called closure. Closures are approximate relations which arise from exact diagrammatic expansions of $g(r)$ in terms of $c(r)$, but with certain classes of diagrams ignored. The system is now fully determined and both the rdf as well as the dcf can be obtained by solving the two coupled equations numerically. By setting the bridge function equal to zero, we obtain the so called hypernetted chain (HNC) closure. This closures has proven to yield good results for long-ranged pair potentials in three dimensions. The Percus-Yevick (PY) closure arises by choosing the following expression for the bridge function

$$B_{\mathrm{PY}} = -[g(r) - c(r)] + 1 + \ln[g(r) - c(r)]. \tag{2.14}$$

The PY closure furnishes accurate results for short-range interactions (such as the hard-sphere potential) in three dimensions. Once $g(r)$ is known, another interesting and important quantity to describe the structure of the system is the structure factor. It simply can be expressed by means of the Fourier transform of the total correlation function $\tilde{h}(\mathbf{k})$:

$$S(\mathbf{k}) = 1 + \rho \tilde{h}(\mathbf{k}). \tag{2.15}$$

For isotropic systems, the structure factor is just a function of the absolute value of the wave vector $\mathbf{k}$.

It is strictly defined as the autocorrelation function of the Fourier components of the density $\rho(\mathbf{r})$

$$S(\mathbf{k}) = \frac{1}{N} \langle \hat{\rho}_{\mathbf{k}} \hat{\rho}_{-\mathbf{k}} \rangle, \tag{2.16}$$

with

$$\hat{\rho}_{\mathbf{k}} = \int \mathrm{d}\mathbf{r} \exp(-i\mathbf{k}\cdot\mathbf{r})\hat{\rho}(\mathbf{r}). \tag{2.17}$$

Eq. (2.15) can easily be verified by rearranging eq. (2.16) [51].

The structure factor $S(k)$ turns out to be a paramount quantity of interest because it allows to access experimental data due to its direct measurement in scattering experiments. The scattering intensity is proportional to $S(k)$ bestowing an excellent opportunity to compare theory and experiment. Moreover, the structure factor offers a path to thermodynamics, as its $k = 0$ value is proportional to the isothermal compressibility χ_{T} of the system

$$S(k = 0) = \rho k_{\mathrm{B}} T \chi_{\mathrm{T}}. \tag{2.18}$$

The Ornstein-Zernike relation, supplied with a closure, allows to calculate $g(r)$, $c(r)$ and $S(k)$ for a fixed pair potential $u(r)$ and given thermodynamic conditions. Various other thermodynamic quantities can be gained by the knowledge of the radial distribution function. These quantities can be written as integrals over this function. Exemplary, we indicate the pressure

$$P = k_{\mathrm{B}} T \rho - \frac{\pi}{2}\rho^2 \int_0^\infty \mathrm{d}r\, r^2 \frac{\partial u(r)}{\partial r} g(r) \tag{2.19}$$

and the internal energy

$$\frac{U}{N} = k_{\mathrm{B}} T + \pi\rho \int_0^\infty \mathrm{d}r\, r u(r) g(r). \tag{2.20}$$

The free energy F can then be determined by thermodynamic integration of P (the pressure route) or of U (the energy route) as given in eqs. (2.19) and (2.20). A third possibility makes use of eq. (2.18) and the relation

$$\chi_T = \left(\Omega \frac{\partial^2 F}{\partial \Omega^2}\right)^{-1}. \tag{2.21}$$

This constitutes the so-called fluctuation route.

If the closures were exact, all the three different routes would yield the same free energy. Due to the inherent approximation of closures, we obtain different free energies by each route. This problem is called thermodynamic inconsistency [8]. The thermodynamic inconsistency is addressed by modifying the closure relation. One or several parameters are included in the closure relation which can be tuned in order to achieve thermodynamic consistency. The Rogers-Young closure makes use of that concept and reads as

$$g(r) = \exp[-\beta v(r)] \left[1 + \frac{\exp[\gamma(r) f(r)] - 1}{f(r)}\right], \tag{2.22}$$

with $\gamma(r) = c(r) - h(r)$ and $f(r) = 1 - \exp(-\alpha r)$. The additional parameter α is varied until the free energy of the virial and the compressibility route coincide. For $\alpha = 0$ the RY closure reduces to the PY closure and for $\alpha \to \infty$ the HNC closure is recovered. Usually the RY closure does not only match the free energies of the two different routes, but also improves the accuracy of the pair structure.

For convenience it proves easier to match the two different compressibilities κ_T^{vir} and κ_T^{fl} instead of the corresponding free energies. The latter is given according to eq. (2.18)

$$\rho k_{\mathrm{B}} \kappa_T^{fl} = S(k = 0; \rho, \alpha) \tag{2.23}$$

where we have explicitly written the density and α dependence. The virial route instead uses the following thermodynamic definition

$$\rho k_{\mathrm{B}} \kappa_T^{vir} = \left[\frac{\partial(\beta P)}{\partial \rho}\right]^{-1} \tag{2.24}$$

where P is the pressure of the fluid given in eq. (2.19). Pertaining to this equation, $g(r)$ attains a explicit α dependence and an implicit one via the density. Combining eqs. (2.19) and (2.24) we obtain

$$\begin{aligned}\left[\rho k_{\mathrm{B}} T \kappa_T^{\mathrm{vir}}\right]^{-1} \simeq 1 \quad &+ \quad 3\pi\Gamma \int_0^\infty \mathrm{d}x \frac{g(r;\Gamma,\alpha)}{x^2} \\ &+ \quad \frac{9\pi}{4}\Gamma^2 \int_0^\infty \mathrm{d}x \frac{1}{x^2}\frac{\partial g(x;\Gamma,\alpha)}{\partial \Gamma} \\ &+ \quad \frac{3\pi}{4}\Gamma \int_0^\infty \mathrm{d}x \frac{1}{x}\frac{\partial g(x;\Gamma,\alpha)}{\partial \alpha}\end{aligned} \tag{2.25}$$

whereas the last term in eq. (2.25) arises from the ρ-dependence of the self-consistency parameter α. It can be neglected because it is smaller than the other terms by orders of magnitude.

In order to calculate the direct correlation function $c(r)$, we proceed in an iterative fashion as follows [53]:

1. Make an initial guess for $c(r)$ and introduce an iteration index i. At this point we have $i = 0$ but we call in general the value of the function $c(r)$ at the i-th iteration $c_i(r)$. For $i = 0$, start with the Mayer function $c_0(r)$ as given in eq. (2.12) and make sure the density is low enough.

2. Fourier transform $c_i(r)$ in order to obtain $\tilde{c}_i(k)$.

3. Use the Ornstein-Zernike relation to get $\tilde{\gamma}_i(k)$.

4. Apply the inverse Fourier transform to that function in order to get its values in real space.

5. Use a closure to obtain a function that could be now the next step in the iteration business but it turns out to be numerically unstable to employ it at the next iteration step. So, let us call the result of the closure at this stage $c_i^{\mathrm{new}}(r)$.

6. Mix the old and new result

$$c_{i+1}(r) = \alpha c_i^{\mathrm{new}}(r) + (1-\alpha)c_i(r), \tag{2.26}$$

with the mixing parameter $0 < \alpha < 1$.

7. Check whether the convergence criterion for $c(r)$ is fulfilled. For a positive answer, you are done and you can proceed anew by gradually increasing the density starting with the converged $c_i(r)$ of the previous cycle. For a negative answer, set $i+1 \rightarrow i$ and return to step **2.**

There is a variety of possibilities to implement the convergence criterion. We rely on the following one

$$|c_{i+1}(r) - c_i(r)| < \epsilon \tag{2.27}$$

for all r. The Rogers-Young closure can easily be incorporated into the iterative scheme above by the following steps

1. Choose some value α (start usually from $\alpha = 1$) and calculate $g(r;\rho,\alpha)$, $S(k,\rho,\alpha)$ as well as $g(r;\rho+\epsilon,\alpha)$, where ϵ is a small number, typically $\epsilon = 10^{-2}$.

2. Calculate κ_T^{fl} from eq. (2.23).

3. Calculate numerically the density derivative of $g(r)$ as

$$\frac{\partial g(r;\rho,\alpha)}{\partial \rho} \simeq \frac{g(r;\rho+\epsilon,\alpha) - g(r;\rho,\alpha)}{\epsilon}. \tag{2.28}$$

4. Use eq. (2.25) to calculate κ_T^{vir}.

5. Form the difference $\kappa_T^{\mathrm{fl}} - \kappa_T^{\mathrm{vir}}$. If it is smaller than some tolerance, you are done. If not, choose now another $\alpha' = \alpha + \delta$ and go to step **1.** You can apply then the Newton-Raphson procedure to converge to the sought-for value α_* that satisfies thermodynamic consistency.

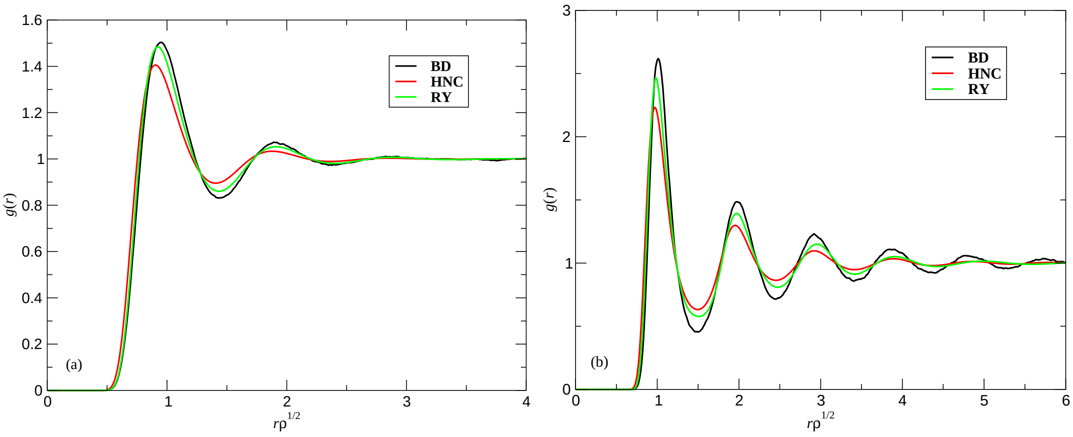

Figure 2.2: The radial distribution functions for the one-component system at (a) $\Gamma = 1.44$ and (b) $\Gamma = 8.2$. The Brownian dynamics (BD) results are compared to the hypernetted chain (HNC) and Rogers-Young (RY) closures.

2.3 Results

In this section, we present results for the structure for the one-component two-dimensional system of super-paramagnetic colloids exposed to a perpendicular, static external magnetic field. To corroborate the (approximate) results of the numerical solutions of the liquid integral equation theory derived in section 2.2, we also have performed extensive Brownian Dynamics (BD) computer simulations [54]. We employed a square box with periodic boundary conditions.[3] We varied the size of the simulation box in order to check carefully for finite-size effects. Typically, we found about 2000 particles to be sufficient for the latter to be negligible. The timestep for the integration of the overdamped Langevin equation of motion was $\Delta t = 10^{-4}\rho D$, where D is the short-time diffusion constant of the particles. A total of 10 000 timesteps were used to equilibrate the system and during further 10^6 timesteps statistics was gathered. In fig. (2.2), typical results for the $g(r)$ at strong coupling, $\Gamma = 1.44$ and $\Gamma = 8.2$, are shown. It is somewhat surprising that the agreement between HNC and BD is rather poor; based on experience for long-range interactions in three dimensions, one might have expected a better agreement. Apparently, space dimensionality is relevant. As the HNC implicitly contains elements of a 'mean-field picture' [56], it is plausible to assert that its quality worsens as d diminishes. The Rogers-Young closure provides much better agreement, although also in this case the

---

[3] We underline that the dipole-dipole interaction in two dimensions is integrable and that is why we do not have to use more sophisticated schemes to treat this interaction, as it is common in three dimensions [55].

amount of correlation is slightly underestimated. The agreement between the RY closure and the simulation worsens somewhat as the coupling grows but it should be kept in mind that at $\Gamma \cong 10$ the system crystallizes [57], thus for $\Gamma = 8.2$ we are already dealing with a strongly correlated fluid. As far as experiments are concerned, we refer the reader to Ref. [21] where nearly identical results for $g(r)$ have been obtained by video microscopy.

2.4 Conclusions

In this chapter, we have derived the basic tools for investigating superparamagnetic colloids in two dimensions. The RY closure turned out to be in good agreement with BD results to describe the fluid structure. Therefore, we will use that closure for the two-component system in the next chapter.

Chapter 3

Binary Mixtures of Superparamagnetic Colloids

Strongly interacting binary mixtures of superparamagnetic colloidal particles confined to a two-dimensional water-air interface are examined by integral equation theory, computer simulation and experiment. In this chapter we investigate the structural behavior of two-component mixtures of such particles. The interparticle interactions are tunable through the application of a magnetic field perpendicular to the air-water surface. Further, they can be influenced by the choice of the relative magnetic susceptibilities of the two colloidal species. For all susceptibility ratios studied, no macroscopic phase separation takes place; the fluid phase remains macroscopically homogeneous but microphase structuring occurs: The interactions with the large particles lead to a clustering of the smaller particles. We combine structural information in reciprocal space together with morphological measures in real space to characterize the ordering of the two species in the binary mixture. The mixture exhibits a partial clustering in equilibrium: in the voids of the matrix of unclustered big particles, the small particles form subclusters with a sponge-like topology which is accompanied by a characteristic small-wave vector peak in the small-small structure factor. This partial clustering is a general phenomenon occurring for strongly coupled negatively non-additive mixtures.

3.1 Introduction

Super-paramagnetic colloidal particles that are confined by gravity on the two-dimensional water-air interface of a pendant droplet are excellent realizations of strictly two-dimensional (2d) classical many-body systems; Refs. [58, 59] provide recent reviews on the new physics in these 2d systems. An external magnetic field, directed perpendicularly to the droplet surface, induces magnetic moments on these particles that align themselves parallel to the applied field. Due to the super-paramagnetic character of the particles, thermal fluctuations of the magnetic moment around the preferred direction are negligible, thus the magnetic moments of the particles are fixed in the direction prescribed by the external field. The strength of the induced dipole moment, on the other hand, can conveniently be tuned by the magnitude of the external magnetic field. This leads to an effective repulsion between the spheres through their induced parallel dipole moments.

While a one-component system of almost monodisperse particles has been extensively studied both for the fluid and for the crystalline phases [14–20, 27, 28, 57, 60] only recently have *two-component mixtures* of such systems been investigated [26,61]. It is of particular interest here to tune, via control of the the susceptibility asymmetry, the so-called non-additivity of the mutual interaction potentials between the species of the mixture. For positive non-additivity, macroscopic phase separation may take place [62,63] whereas, for negative values of the same, microphase separation and clustering of the particle species in domains within the fluid might occur - qualitatively similar to results obtained in three spatial dimensions and effective one-component systems [64–70]. A wide variety of systems displaying circular and striped pattern formation have been analyzed such as magnetic garnets, Langmuir monolayers and thin films of adsorbates [71, 72]. Stable cluster formation has been observed in systems interacting via the competition between a short-ranged attraction and a long-ranged repulsion [73] and it can occur even in the complete absence of attractions, provided that the repulsive potential is bounded and decays sufficiently rapidly to zero at large interparticle distances [74]. The competition between a short-ranged Lennard-Jones-like and a long-ranged repulsive Yukawa potential leads to a cluster formation that has been proven by ground-state energy calculations [75]. This system even exhibits a gel phase driven by the inherent self-generated cluster polydispersity [76]. Also nanoparticles deposited at the air-water interface show spontaneous patterning in a cluster-like structure [77].

In this chapter, we investigate the liquid structure and local ordering in a 2d binary mixture interacting via dipole-dipole repulsions. We use integral equation theories and computer simulations that compare very well with each other and confront our theoretical findings with direct experimental data. Macrophase separation (demixing) does not take place for any combination of physical parameters, a property that can be traced back to the fact that the non-additivity parameter of the interactions is negative irrespective of the value of the magnetic susceptibility ratio. Instead, microphase structuring with a partial clustering of the species with lower interaction strength takes place, with a sponge-like structure emerging. Partial structure factors and a morphological characterization of the particle positions obtained in computer simulations and employing the Euler characteristic [78, 79] are used to characterize the ordering of the two species in the uniform mixture. This partial clustering has been confirmed experimentally. We compare structure factors, parti-

cle snapshots and the Euler characteristic obtained by simulation to the equivalent quantities obtained by experiment.
The rest of this chapter is organized as follows: in sec. 3.2 we extend our one-component model to the two-component case and briefly describe the experimental realization. The integral equation theory for the mixture is concisely presented in sec. 3.3. Results for the partial structure factors are presented in sec. 3.4 and the morphological analysis in sec. 3.5. In sec. 3.5 we compare our theoretical findings to the experimental data. Finally, in sec. 3.7 we summarize and draw our conclusions. Some technical details on fast two-dimensional Fourier transforms are relegated to Appendix A and mathematical material on the derivation of the Euler characteristic on a square lattice is presented in Appendix B.

3.2 Extension of the model and its experimental realization

Generalizing the ideas of chapter 2, we now allow for a second component to be present in the system (see fig. 3.1).

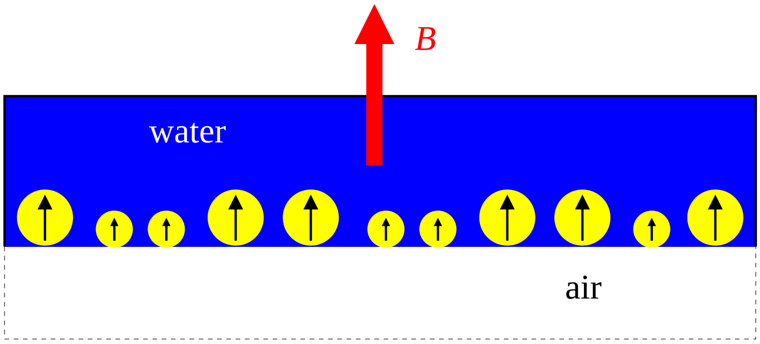

Figure 3.1: Schematic view of the setup: binary mixture of superparamagnetic colloidal particles at an air-water interface in an external magnetic field **B** perpendicular to the plane.

Each component is characterized by its partial density ρ_1, ρ_2 and its susceptibility χ_1, χ_2, respectively. We model all particles as point-like but refer thereafter to the particles having the larger susceptibility as the ‘big’ (species 1) and those with smaller susceptibility as ‘small’ (species 2). In the experimental setup, the particles acquire their superparamagnetic character through doping with Fe_2O_3. For a given doping density, the bigger the particle is, the larger its susceptibility. Therefore, in what follows, we refer to the particles having the larger susceptibility as the ‘big’ particles, although the *physical* size of the colloids does not enter in the pair potentials. Accordingly, we are now dealing with three different interactions:

$$\beta u_{ij}(x) = \frac{\Gamma_{ij}}{x^3}, \quad i,j = 1,2. \tag{3.1}$$

In eq. (3.1) above, x stands for the distance between any two particles scaled over the average interparticle distance between *big* particles, $x \equiv r/a_{11}$, where $a_{11} = 1/\sqrt{\rho_1}$. Therefore, the expressions for the interaction strengths Γ_{ij} are generalized to

$$\Gamma_{ij} = \frac{\beta \chi_i \chi_j B_0^2}{a_{11}^3}, \quad i,j = 1,2. \tag{3.2}$$

The two-component system is completely characterized by three quantities: the density ratio ρ_2/ρ_1, the susceptibility ratio χ_2/χ_1 and one of the three interaction strengths, which we pick as Γ_{11} in what follows. We address in this chapter exclusively an external magnetic field acting perpendicular to the confining plane.

The experimental system is fully described by the theoretical model introduced above and is explained in detail elsewhere [17,21]. We use superparamagnetic particles [80] with susceptibilities $\chi_1 = 6.2 \times 10^{-11}\,\mathrm{Am^2/T}$ and $\chi_2 = 6.6 \times 10^{-12}\,\mathrm{Am^2/T}$, which are suspended in a free-hanging, flat water droplet attached to a top-sealed glass ring (diameter 8 mm, see fig. 3.1). The particles are made from porous polystyrene spheres that are doped with small Fe_2O_3 clusters to make them superparamagnetic and are further sealed with an epoxy layer. Stabilization with sodium dodecyl sulfate prevents the particles from aggregation. Due to high mass density ($d_1 = 1.3\,\mathrm{kg/dm^3}$, $d_2 = 1.5\,\mathrm{kg/dm^3}$), both types of particles are pinned down to the water-air interface by gravity and form an ideal, two-dimensional monolayer of binary dipoles. The relatively small gravitational lengths of $l_1 = 8\,\mathrm{nm}$ and $l_2 = 62\,\mathrm{nm}$ for big and small particles, respectively, compared to the particle diameters of $4.7\,\mu\mathrm{m}$ and $2.8\,\mu\mathrm{m}$ ensure an almost perfect realization of a 2d-system. The flatness of the interface can be controlled in the range of less than $1\,\mu\mathrm{m}$. Inclination control of the whole setup guarantees a nearly horizontal alignment of the flat surface, ruling out the occurrence of any density gradients in the sample. We control the interaction strengths Γ_{ij} between the dipoles by applying an external magnetic field up to 4 mT, perpendicular to the interface. The dipole interaction dominates all other interactions in this colloidal system [21]. The sample was conserved for months and measurements were taken for a duration of up to 24 hours. All necessary data were recorded by video microscopy. Typically, about 1300 particles were observed in a box of $689\,\mu\mathrm{m} \times 505\,\mu\mathrm{m}$, with a total amount of 10^6 particles in the whole sample. The density ratio ρ_2/ρ_1 was varied between 0.67 and 1. Local and statistical properties of the sample are gathered at a rate of about 1 frame/second on all relevant time and length scales.

3.3 Multi-component liquid integral equation theory

The extension from the one-component system to the multi-component system is straightforward. Consider a two-component system consisting of N_1, N_2 particles enclosed in a macroscopic area A and described by the three pair interactions $u_{ij}(r)$, $i, j = 1, 2$, r denoting the distance between any two particles. The pair structure is fully determined by three correlation functions $h_{ij}(r)$, $i \leq j = 1, 2$; due to symmetry, $h_{ij}(r) = h_{ji}(r)$. The generalization of the OZ relation for multicomponent mixtures reads as

$$\tilde{\mathbf{H}}(k) = \tilde{\mathbf{C}}(k) + \tilde{\mathbf{C}}(k) \cdot \mathbf{D} \cdot \tilde{\mathbf{H}}(k), \tag{3.3}$$

where $\tilde{\mathbf{H}}(k)$ and $\tilde{\mathbf{C}}(k)$ are 2×2 symmetric matrices with elements,

$$[\tilde{\mathbf{H}}(k)]_{ij} = \tilde{h}_{ij}(k) \text{ and } [\tilde{\mathbf{C}}(\mathrm{k})]_{\mathrm{ij}} = \tilde{\mathrm{c}}_{\mathrm{ij}}(\mathrm{k}), \tag{3.4}$$

and $\mathbf{D}$ is a 2×2 diagonal matrix of the partial densities,

$$[\mathbf{D}]_{ij} = \rho_i \delta_{ij}. \tag{3.5}$$

More specifically, the Ornstein-Zernike relation can be expressed for the two-component case as

$$\tilde{h}_{ij}(k) = \frac{\tilde{c}_{ij}(k) - \Delta_{ij}/\rho_i}{1 + \Delta - E}, \tag{3.6}$$

where $\Delta = \rho_1\rho_2[\tilde{c}_{11}(k)\tilde{c}_{22}(k) - \tilde{c}_{12}^2(k)]$ and $E = \rho_1\tilde{c}_{11}(k) + \rho_2\tilde{c}_{22}(k)$. The linear algebraic system (3.3) provides three independent equations with 6 unknown functions $\tilde{h}_{ij}(k)$ and $\tilde{c}_{ij}(k)$. Therefore, three closure relations have to be supplied to determine the unknown functions. Apart from the generalizations of the aforementioned HNC- and PY-closures, a particularly reliable relation is provided by the Rogers-Young closure [81] that 'interpolates' between the two and has the form:

$$h_{ij}(r) = \exp[-\beta u_{ij}(r)] \left[1 + \frac{\exp[\gamma_{ij}(r) f_{ij}(r)] - 1}{f_{ij}(r)}\right] - 1, \tag{3.7}$$

whereas $\gamma_{ij}(r) = h_{ij}(r) - c_{ij}(r)$ and the 'mixing functions' $f_{ij}(r) = 1 - \exp(-\alpha_{ij} r)$ include tunable parameters α_{ij} that are chosen in order to enforce thermodynamic consistency. This turns to be sufficient to bring about agreement with simulation and experiment and it guarantees the equality between the *total* virial and fluctuation compressibilities.[1] The pressure takes now the form

$$\beta P = \rho - \frac{\pi}{2}\rho^2 \sum_{i=1}^{2}\sum_{j=1}^{2} x_i x_j \int_0^\infty \mathrm{d}r r^2 \frac{\partial \beta u_{ij}(r)}{\partial r} g_{ij}(r; \rho, \zeta) \tag{3.8}$$

---

[1] An alternative approach is to use all three α_{ij}'s to match also the partial compressibilities [83].

with $\rho = \rho_1 + \rho_2$ and $x_i = \rho_i/\rho$. The compressibility can be calculated using eq. (2.24), where x_i $(i = 1, 2)$ is kept constant. The compressibility can be written as [82]

$$\rho k_{\mathrm{B}} T \chi_T^{\mathrm{fl}} = \frac{S_{11}(0)S_{22}(0) - S_{12}^2(k)}{x_2 S_{11}(0) + x_1 S_{22}(0) - 2\sqrt{x_1 x_2} S_{12}} \tag{3.9}$$

for the specific case of a two-component mixture.

We rely on a single self-consistency parameter $\alpha \equiv \alpha_{ij}$. The parameter α_{ij} is determined by the requirement to achieve thermodynamic consistency, *i.e.*, to match the total virial and fluctuation compressibility. The three partial structure factors for the two component system read as

$$S_{ij}(k) = \delta_{ij} + \sqrt{\rho_i \rho_j}\tilde{h}_{ij}(k) \tag{3.10}$$

In solving the two coupled integral equations, the OZ-relation and the closure, one has to invoke an iterative procedure that requires the repeated calculation of convolution integrals. These are evaluated most efficiently and rapidly in reciprocal space, by invoking the tool of fast Fourier transforms. Although this procedure is straightforward in three dimensions, in which the Fourier transform of a spherosymmetric function takes the form of a one-dimensional sine transformation, in two dimensions things are more complicated. We have circumvented this problem by applying the procedure of Caillol et al. [84]. A short account of the latter technique is given in Appendix A.

3.4 Theoretical and simulation results

For the rest of this chapter, we turn our attention to the results of the much richer two-component case. For all tested parameter combinations, the RY closure almost perfectly matches the structural correlations predicted by the simulations. As a representative result, we provide one parameter combination in fig. 3.2: it shows excellent agreement between the simulation data and the RY closure whereas, as could be anticipated from the one-component case, the HNC fails to be as accurate. Excellent agreement with experimental structural data for a different parameter combination will be shown later in this chapter. Therefore, in what follows, we rely on the RY closure to analyze the pair structure of the fluid regime. We vary the relevant system parameters, Γ_{11}, ρ_2/ρ_1 and χ_2/χ_1 and discuss the concomitant effects on the structural correlations.

Let us first increase the coupling strength, covering a range from $\Gamma_{11} = 1.0$ to $\Gamma_{11} = 9.0$. Results for the radial distribution functions $g_{ij}(r)$ are shown in fig. 3.3; for all these values, the system remains fluid. At the same time, we keep the density and susceptibility ratio fixed at $\rho_2/\rho_1 = 0.5$ and $\chi_2/\chi_1 = 0.5$. For increasing interaction

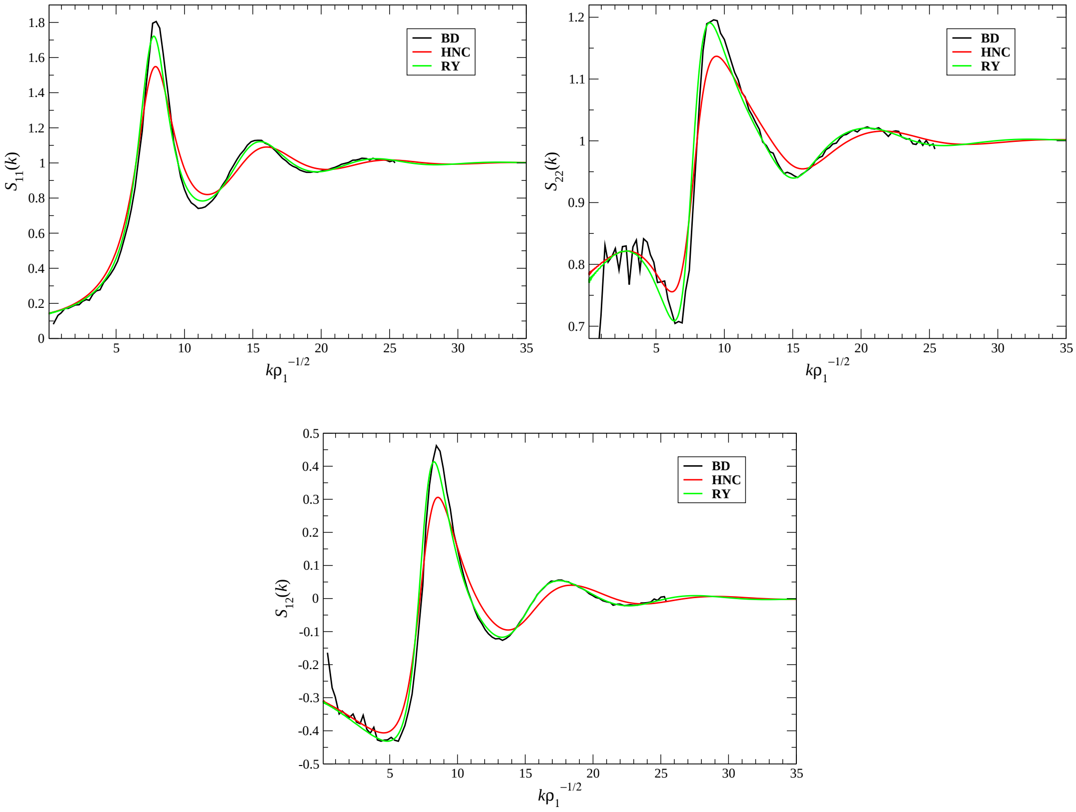

Figure 3.2: The partial structure factors $S_{11}(k)$, $S_{22}(k)$, and $S_{12}(k)$ for the two-component system. Computer simulation results obtained by Brownian dynamics (BD) are compared to the HNC and RY closure. The parameter combinations here read as $\Gamma_{11} = 3.0$, $\rho_2/\rho_1 = 0.5$ and $\chi_2/\chi_1 = 0.5$.

strength, the height of the main peak of all three distribution functions increases steadily, whereas the peak position r, measured in units of a_{11}, does not shift. The result is physically reasonable: we can assume that Γ_{11} is increased by turning the external field $\mathbf{B}_0$ stronger but otherwise leaving the particle numbers untouched. Then, the typical interparticle distances within the first coordination shell remain unchanged and only the degree of local ordering is affected, due to the increasingly strong repulsions. Note also that the extent of the 'correlation holes' b_{ij}, i.e., the small-r region for which $g_{ij}(r) \cong 0$, differs between the three distribution functions. Indeed, the ordering $u_{22}(r) < u_{12}(r) < u_{11}(r)$ leads to the inequalities $b_{22} < b_{12} < b_{11}$.

These features are reflected in the structure factors, shown in fig. 3.4. In reciprocal space, the height of the principal peak position grows as the coupling increases. At the same time, the structure factors reveal a striking feature that cannot be

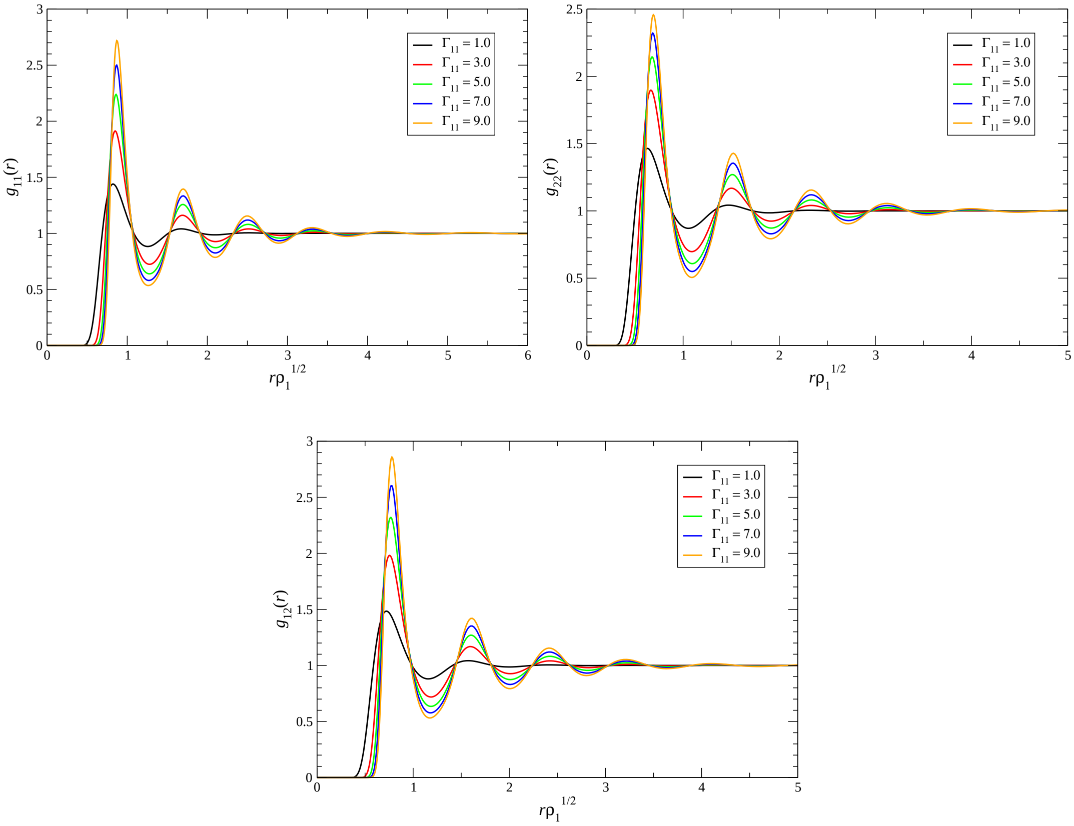

Figure 3.3: Partial radial distribution functions for the two-component system. Varying the interaction strength Γ_{11}, we keep the other parameters fixed: $\rho_2/\rho_1 = 0.5$ and $\chi_2/\chi_1 = 0.5$.

distinguished by looking at the real-space distribution functions alone: the structure factor $S_{22}(k)$ shows a pre-peak at, roughly, $k_{\rm clus}/\sqrt{\rho_1} \cong 3.5$ that precedes the main peak, located at $k_{\rm part}/\sqrt{\rho_1} \cong 8.5$. The latter signals ordering with a length scale $\lambda_{\rm part} = 2\pi/(8.5\sqrt{\rho_1}) \cong 0.5/\sqrt{\rho_2}$, whereas the former points to the existence in the system of spatial structures formed by the small particles that have a larger typical length scale $\lambda_{\rm clus} \cong 1.27/\sqrt{\rho_2}$. Note that $\lambda_{\rm part}$ is smaller than the typical interparticle distance $a_{22} = 1/\sqrt{\rho_2}$ between the small particles by about a factor 2. This implies that the latter are 'squeezed together' due to the influence of the big ones. Thus, $\lambda_{\rm part}$ corresponds to the small-small interparticle distance, whereas $\lambda_{\rm clus} > \lambda_{\rm part}$ describes, as will be explicitly demonstrated shortly, the extent of *clusters* of tightly squeezed small particles, nested in the voids formed by the big ones. The fact that the $k_{\rm clus}$-pre-peak height is not particularly prominent, points to rather diffuse clusters with an ill-defined boundary. Yet, their presence is clearly signaled by the

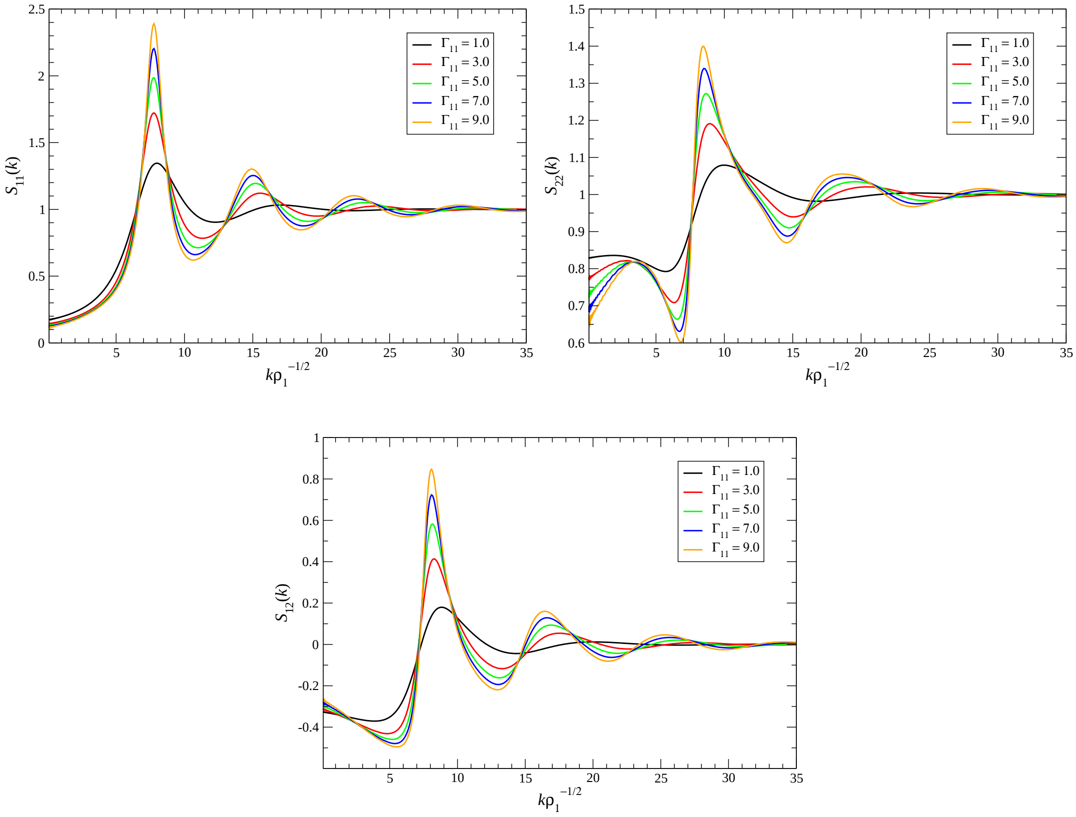

Figure 3.4: The partial structure factors $S_{11}(k)$, $S_{22}(k)$, and $S_{12}(k)$ for the two-component system. The interaction strength Γ_{11} is varied whereas the other parameters are kept fixed: $\rho_2/\rho_1 = 0.5$, $\chi_2/\chi_1 = 0.5$.

pre-peak, whose position (and hence the cluster size) is insensitive on the coupling. We emphasize here that this is a novel phenomenon, which persists for a wide range of parameter combinations. Of particular importance is the *absence* of any similar feature in the big-big structure factor $S_{11}(k)$ and in the cross-structure factor $S_{12}(k)$. The physical origin of this *partial clustering* can be traced to the particular form of the interactions. A moderate amount of negative non-additivity (see below) as well as the ordering $u_{22}(r) < u_{12}(r) < u_{11}(r)$ are necessary, which explains the fact that partial clustering is absent both for additive hard-sphere mixtures [87] and for the positively non-additive Asakura-Oosawa model [88], to mention some of the most popular models of liquid-state and soft matter theory.

Let us now investigate the evolution of the structural characteristics when the other two free parameters of the mixture are varied. In order to examine the influence of the composition, we keep the coupling constant fixed at $\Gamma_{11} = 3.0$ and the sus-

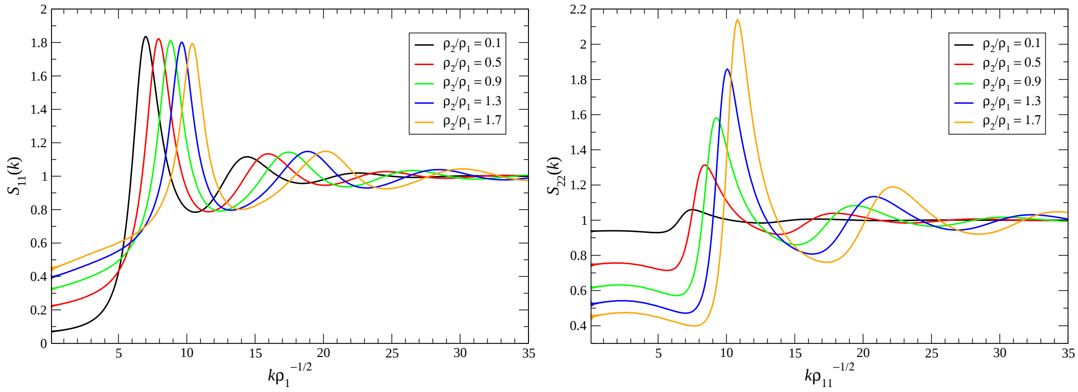

Figure 3.5: Partial structure factors for the two-component system. Here the density ratio is varied and the other two parameters are fixed at $\Gamma_{11} = 3.0$ and $\chi_2/\chi_1 = 0.7$.

ceptibility ratio at $\chi_2/\chi_1 = 0.7$. Subsequently, we vary the density ratio starting from a majority of big particles and ending up with a majority of the small ones. Results for the structure factors are shown in fig. 3.5. The height of the main peak of the structure factor remains roughly unchanged for the big particles, however its position moves clearly to the right as small particles are added. This points to a tendency of the big particles to move closer upon addition of the small ones, a feature explicitly confirmed by the evolution of their partial distribution function $g_{11}(r)$, shown in fig. 3.6. The small particles require space for themselves and are thus 'pushing' the big ones closer to each other; the interaction $u_{11}(r)$ is becoming effectively softer, a feature also confirmed by the increase in the partial compressibility $\chi_1 = S_{11}(k = 0)/(k_{\mathrm{B}}T\rho_1)$, see fig. 3.5. However, this partial compressibility never diverges, thus no macrophase separation occurs. Therefore, the reordering of the big particles in the presence of the small ones is more subtle: big particles are coming closer together and they open up in this way space for the small ones. The two regions of space, however, are closely intertwined with each other, as no macrophase separation takes place.

Let us now turn our attention to $S_{22}(k)$ shown in fig. 3.5. The shift of the 'particle peak' k_{part} to higher k-values upon increasing ρ_2 simply describes the decreasing interparticle separation between the small particles as their population grows. The 'cluster prepeak' k_{clus} is also present, albeit weak, and its position remains unchanged as ρ_2 grows. The physical interpretation is that more and more small particles are squeezed into the voids left by the big ones but the size of these voids (small-particle clusters) is insensitive to ρ_2. Note that for $\rho_2/\rho_1 = 0.1$ both the cluster prepeak and the particle peak are weak, due to the low partial concentration. However, the

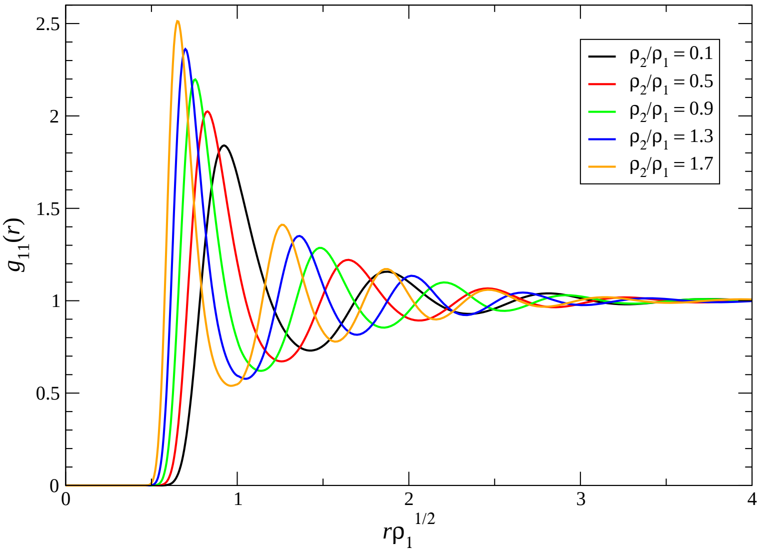

Figure 3.6: The radial distribution function $g_{11}(r)$ of the big particles for the parameter combination of fig. (3.5).

cluster prepeak survives also when the small particles are in the majority.

Finally, let us fix the coupling strength and the density ratio at $\Gamma_{11} = 3.0$ and $\rho_2/\rho_1 = 0.5$ and vary the susceptibility ratio. The corresponding structure factors can be seen in fig. 3.7. For all investigated parameter combinations, the partial structure factors remain finite for $k = 0$, therefore a fluid-fluid demixing is not expected for the system at hand. Again, however, the cluster pre-peak in the structure factor $S_{22}(k)$ is visible, whereas no such signature appears in $S_{11}(k)$. Note that for low susceptibility ratio, $\chi_2/\chi_1 = 0.1$, the pre-peak is at least as pronounced as the 'main' peak: as the direct interaction scales as χ_2^2 but the cross-interaction as $\chi_1\chi_2$, the particle-particle correlations are weaker than the cluster ones. At the other extreme, $\chi_2/\chi_1 = 0.7$, the prepeak is still present but clearly subdominant to the main peak. Indeed, there are two trivial limits for the two-component system, when it is looked upon through its dependence on the susceptibility ratio $\xi \equiv \chi_2/\chi_1$, where $0 \leq \xi \leq 1$. At $\xi = 0$, the small particles are ideal and experience no forces, neither among themselves nor with the big particles. In this case, $S_{22}(k) = 1$ and we are dealing with a one-component system at $\Gamma = \Gamma_{11}$. At the other extreme, $\xi = 1$, the two species become identical and there is just one structure factor at a rescaled coupling parameter $\Gamma = \Gamma_{11}(1 + \alpha)^{3/2}$, where $\alpha \equiv \rho_2/\rho_1$. Also in this case there is no subclustering phenomenon. We expect, therefore, that the pre-peak in $S_{22}(k)$ exists in some domain $\xi \in [\xi_1, \xi_2] \subset [0, 1]$. We were able to show that ξ_1 is at least as small as 0.1 and ξ_2 at least as large as 0.7.

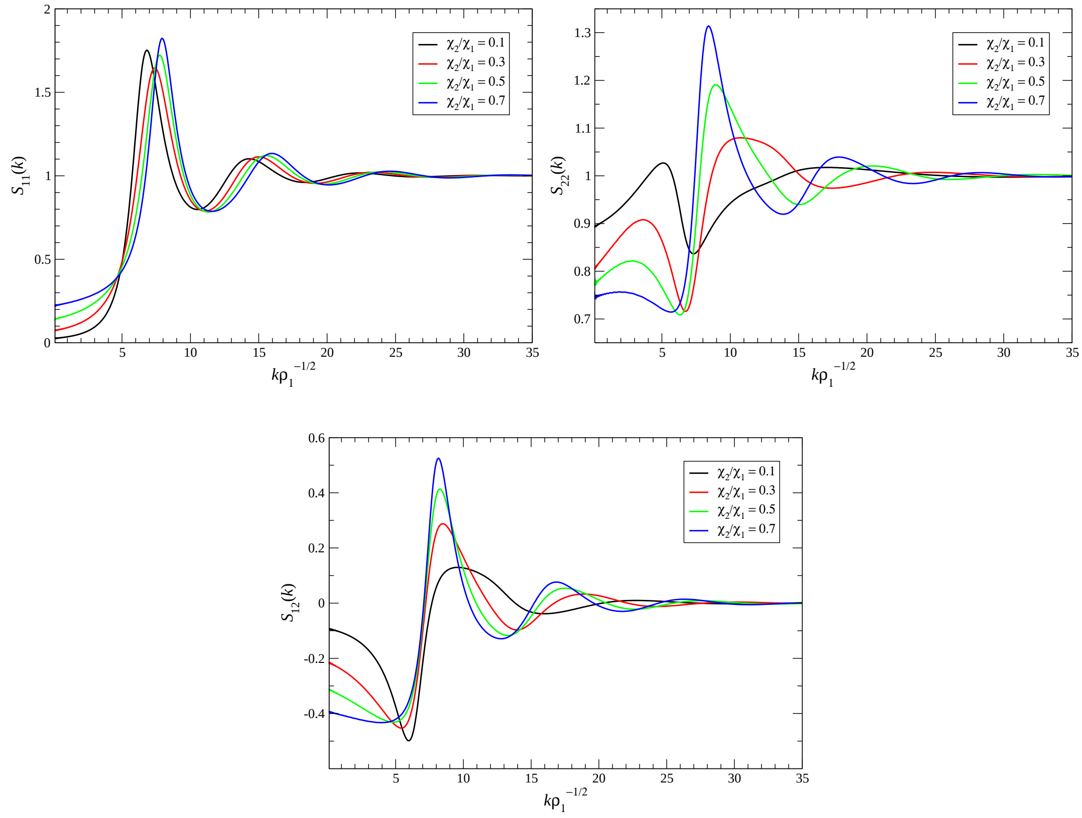

Figure 3.7: Partial structure factors for the two-component system and their dependence on the susceptibility ratio χ_2/χ_1. The other two parameters are fixed at $\Gamma_{11} = 3.0$ and $\rho_2/\rho_1 = 0.5$.

A key quantity to understand the phenomena at hand is the so-called *non-additivity parameter* Δ [86], which can be derived from the interaction potentials $u_{ij}(r)$ as follows. First, a mapping onto effective hard-disk diameters σ_{ij} is performed according to the Barker-Henderson procedure [51]:

$$\sigma_{ij} = \int \mathrm{d}r \, \{1 - \exp[-u_{ij}(r)/k_{\mathrm{B}}T]\} \,. \tag{3.11}$$

Then, Δ is defined as

$$\Delta = 2\sigma_{12} - (\sigma_{11} + \sigma_{22}). \tag{3.12}$$

The dependence of $\tilde{\Delta} \equiv \Delta/(\sigma_{11}+\sigma_{22})$ on ξ is shown in fig. 3.8. Clearly, the case $\xi = 0$ leads to $\tilde{\Delta} = -1$, whereas $\xi = 1$ corresponds to $\tilde{\Delta} = 0$. The negativity of $\tilde{\Delta}$ for all ξ-values provides an explanation for the absence of macrophase separation because it expresses the physical fact that the particles *on average* dislike the ‘opposite’

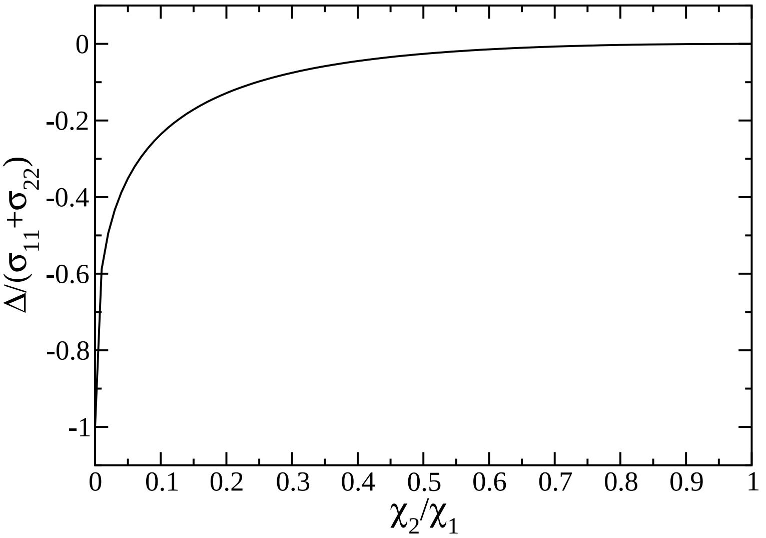

Figure 3.8: The non-additivity parameter Δ of the two-component magnetic mixture [eq. (3.12)] against the susceptibility ratio χ_2/χ_1.

species less than they dislike their own. The negativity of $\tilde{\Delta}$ *together* with the property $u_{22}(r) < u_{12}(r) < u_{11}(r)$ for all r lies in the heart of the subclustering phenomenon for the small particles. Indeed, by trying to create many contacts between the small particles, the system is reducing its energy due to the first part of the inequality above. At the same time, a full separation between big and small is also unfavorable, since the big particles would then have mostly contacts with each other, a feature that is disfavored by the second part of the inequality. The system finds then the best compromise by creating irregular clusters of the small particles, which are nested in the voids formed by the big ones. As the topology and morphology of this mutual arrangement cannot be unambiguously determined based on the reciprocal-space information alone, we proceed in the following section with a complementary morphological analysis in real space.

3.5 Morphological analysis

A real-space perspective of the spatial arrangements of the two components is shown in fig. 3.9, a typical simulation snapshot of the big and small particles, respectively, for the parameter combination $\Gamma_{11} = 3.0$, $\chi_2/\chi_1 = 0.5$ and $\rho_2/\rho_1 = 0.5$. Here, the total system contains 1200 big and 600 small particles. It can be seen that the big particles have a semi-compact arrangement: whereas in most parts of the snapshot they are close to each other, there exist also void regions in which the small particles perfectly fit. Note that the void sizes in the left part of fig. 3.9 are *not* visible in reciprocal space: the only length scale featuring prominently as a peak in $S_{11}(k)$ is the one corresponding to the typical interparticle separation. Since the big particles have to make space for the voids, this scale is smaller than a_{11} (which is the typical interparticle distance without small particles), hence the shift of the peak of $S_{11}(k)$ at larger k-values can be observed in figs. 3.5 and 3.6.

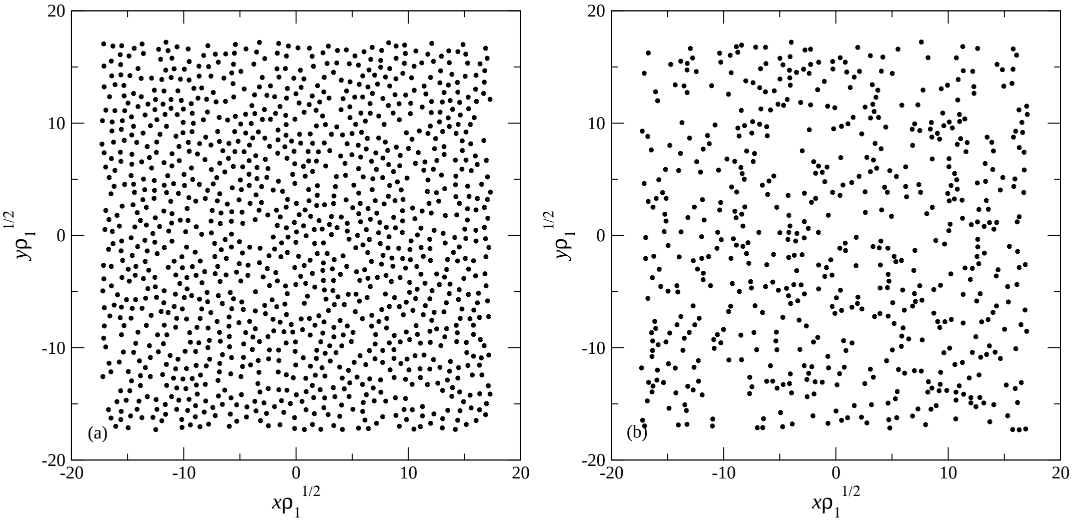

Figure 3.9: Simulation snapshot of the big particles (left panel) and the small particles (right panel) for the following parameters: $\Gamma_{11} = 3.0$, $\rho_2/\rho_1 = 0.5$, $\chi_2/\chi_1 = 0.5$.

The mutual arrangement and the nesting of the irregular clusters of small particles in the voids of the big ones is made manifest in fig. 3.10, where we show big and small particles together. It is evident that small particles cluster in the holes formed by the 'sponge-like' structure of the big ones. Yet, an inspection with the bare eye is dangerous and it can lead to erroneous results. It is pertinent that we quantify the morphology of the mixture and for this purpose we employ in what follows a robust measure borrowed by integral geometry, namely a topological invariant of the pattern formed by the particles, the Euler characteristic X [78, 79].

The Euler characteristic is first defined for any *closed*, *bounded*, and *convex* set (closed body) K in an d-dimensional space $\mathbf{E}^d$ with a regular boundary. We denote the set of all such bodies as $\mathcal{K}$. For such bodies, X is defined as

$$X(K) = \begin{cases} 1, & \text{for convex } K \in \mathcal{K} \subset \mathbf{E}^d,\ K \neq \emptyset, \\ 0, & \text{for } K = \emptyset. \end{cases} \tag{3.13}$$

The definition can be extended to bodies with irregular boundaries (such as polygons

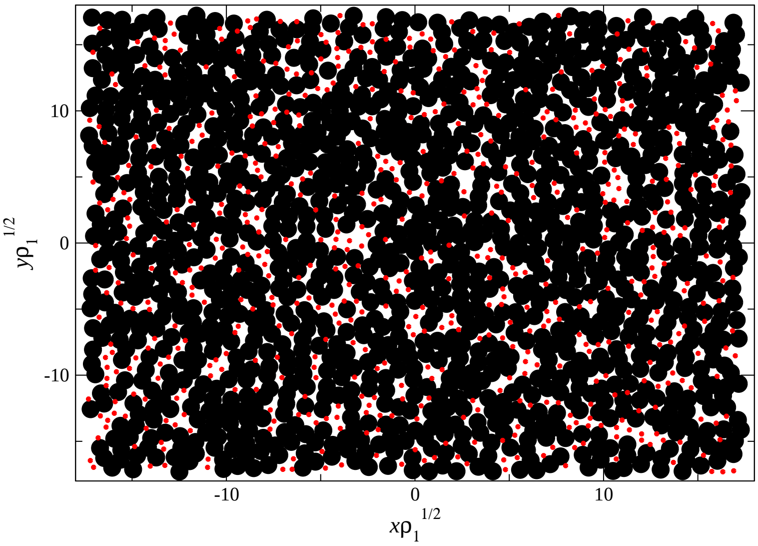

Figure 3.10: Simulation snapshot of big particles and small particles together, for the parameter combination of fig. (3.9).

in two dimensions) by considering the smooth ϵ-parallel body, K_ϵ, consisting of the union of K and all points within a distance $\leq \epsilon$ from the boundary of K [78]. By expanding the d-dimensional volume of K_ϵ, in powers of ϵ, the Euler characteristic of the irregular body is then proportional to the coefficient of the power ϵ^d. It has precisely the same value, 1 for convex bodies and 0 for the empty set, as given by eq. (3.13) above for bodies with a smooth boundary. Further, the definition of X can be extended to non-convex shapes containing an arbitrary number of holes and belonging to the set $\mathcal{R}$ of subsets of $\mathbf{E}^d$ that are constructed from finite unions and intersections of convex bodies including the empty set $\emptyset$ (clearly, $\mathcal{K} \subset \mathcal{R}$). The extension of X to such sets follows from the property of *sub-additivity*:

$$X(A \cup B) = X(A) + X(B) - X(A \cap B), \tag{3.14}$$

for any A, $B \in \mathcal{R}$. Notice that the Euler characteristic of the union of two sets A and B is the sum of the individual ones *minus* the Euler characteristic of the intersection.[2]

The morphological analysis of the spatial pattern formed by the particles was carried out as follows. The particle positions of any snapshot were marked and covering

---

[2] In fact, the Euler characteristic is just one of the $d+1$ Minkowski functionals [78,79] of a body embedded in d-dimensional Euclidean space, and all share the sub-additivity property; in three dimensions, the four Minkowski functionals are the volume, exposed area, integral mean curvature and Euler characteristic X; in two dimensions, they are the covered area, exposed line length and, again, X. For the volume, area and length the sub-additivity property is evident.

circles of *varying radii* R_0 were superimposed on the position of each particle. The circles were filled, resulting thereby in a spatial black-and-white pattern whose appearance depends on R_0 as well as on the original particle positions. Interpreting the black parts as 'full' and the white parts as 'empty', the pattern consists, for any choice of R_0, of a number of mutually disconnected components $D(R_0)$ as well as a number of holes $H(R_0)$. The Euler characteristic $X(R_0)$ is an integer number and *in two dimensions* it is simply expressed as:[3]

$$X(R_0) = D(R_0) - H(R_0). \tag{3.15}$$

For instance, $X = 1$ for a circle but $X = 0$ for a ring, $X = -1$ for an eight-shaped union of two rings and so on. For the system at hand, we have at small R_0 as many mutually disconnected components as particles, $D = N$, there are no holes ($H = 0$) and hence $X/N = 1$. For very large covering radii, the whole pattern is black, $D = 1$, $H = 0$ and $X/N \to 0$ for $N \to \infty$. Information on the topology of the mixture is gained by the behavior of the X/N vs. R_0-curve at intermediate R_0 values.

The recognition of disconnected components and holes may appear straightforward at first yet it is a challenging problem of image analysis and processing. The problem can be simplified by digitizing the image created by the covering circles. To this end, we have imposed a fine quadratic grid on the picture, with lattice constant $l = 0.05\,R_0$. Any quadratic pixel was assigned the value 'empty' or 'full' according to the following criterion: if the center of a pixel is closer to the center of any circle than the radius of the latter, the pixel is 'full'; otherwise, it is 'empty'. We assign now 'Ising-like spin variables' $u(i,j)$ that live on the dual lattice, characterized by a binary 'emptiness variable', $u(i,j) = 1$ if the pixel at which $u(i,j)$ is centered is empty and $u(i,j) = 0$ if it is full. Here, i, j are integer indices sequentially labeling the lattice sites in the horizontal and vertical directions, respectively; $i, j = 1, 2, \ldots, L$ in an $L \times L$ square lattice. The digitized image generates therefore a morphological lattice model and the Euler characteristic $X[u]$ of each configuration $[u] = \{u(i,j)\}$, $i, j = 1, 2, \ldots, L$, can be calculated *locally* and involves up to four-spin interactions only. It is given by the expression:

$$\begin{aligned} X[u] = \; \textstyle\sum_i \sum_j \; & \{-u(i,j) + u(i,j)\,[u(i+1,j) + u(i,j+1)] \\ & -u(i,j)u(i+1,j)u(i,j+1)u(i+1,j+1)\} \end{aligned} \tag{3.16}$$

The double sum runs over all lattice sites. Periodic boundary conditions were employed for the pixels at the borderlines of the $L \times L$-square. For a sketch of the

---

[3] We emphasize the space dimensionality because in three dimensions the situation is different: although X remains an integer, it has there the form $X = D + C - T$, where C is the number of cavities (as in a hollow sphere) and T the number of tunnels (holes). Note also that our definition of X differs by the one used in other contexts by a trivial factor 2.

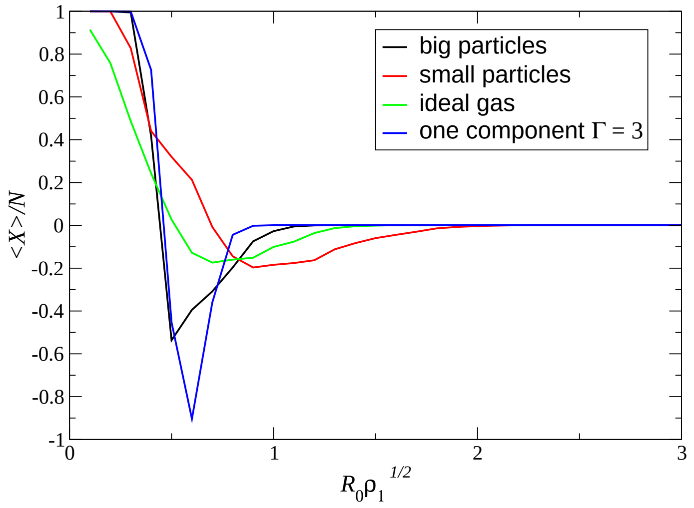

Figure 3.11: The expectation value of the Euler characteristic (per particle) plotted against the covering radius for a binary mixture of 1200 big and 600 small particles and for the parameters $\Gamma_{11} = 3.0$ and $\chi_2/\chi_1 = 0.5$. The results are averaged over several simulation snapshots. For comparison, the corresponding curves of the ideal gas and a one-component system are also shown.

derivation of eq. (3.16) above, we refer the reader to Appendix 3.5 and for a more general discussion to the Appendix of Ref. [78]. The analysis was carried out for a large number of simulation snapshots and the expectation value $\langle X\rangle/N$ was calculated as a function of R_0.[4]

Results of this procedure are shown in fig. 3.14 for a particular parameter combination ($\Gamma_{11} = 3.0, \chi_2/\chi_1 = 0.5$, and $\rho_2/\rho_1 = 0.5$) for which the structural data featured a cluster prepeak at $S_{22}(k)$. The quantity shown is always $\langle X\rangle/N$, where N is the number of big or small particles, depending on the curve. A useful comparison is provided by considering also the same curves drawn for an one-component system at the same Γ_{11}-value as well as for an ideal gas. Comparing the Euler characteristic-curve of the small particles with that of the ideal gas, we see that the former decays to zero much slower than the latter; and the most negative part of the former occurs for larger covering radii than that of the latter. Ideal particles form 'clusters' just by accident, as a result of the Poisson process of their insertion in the plane. Interacting particles form clusters in order to optimize the free energy of the mixture. The latter are thus larger and hence a larger covering radius is necessary to create holes between them.

---

[4] Note that the quantity $\langle X\rangle$ is extensive, a property that qualifies the latter to be used as a 'topological order parameter' in morphological models [78].

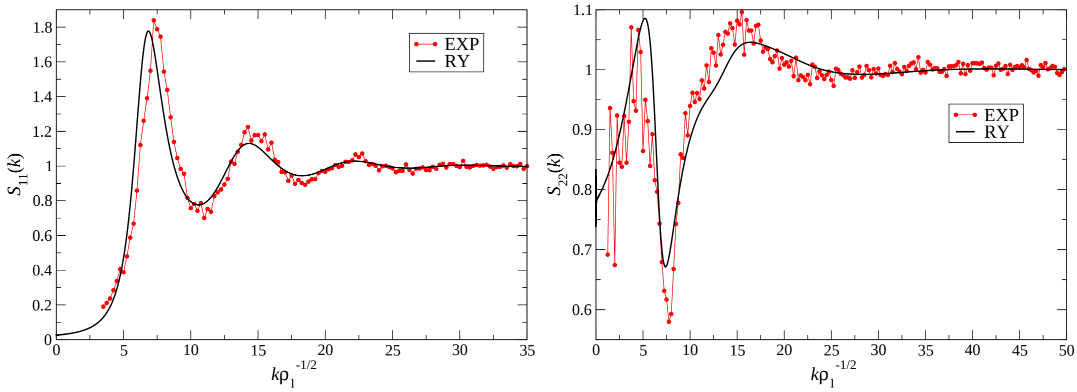

Figure 3.12: Partial structure factors $S_{11}(k)$ for the big particles and $S_{22}(k)$ for the small particles. Experimental results (EXP) are compared to theoretical ones (RY) for the parameters: $\Gamma_{11} = 4.05$, $\rho_2/\rho_1 = 0.89$, $\chi_2/\chi_1 = 0.1$.

The position of the most negative value of $\langle X \rangle/N$ for the small particles occurs at $R_0\sqrt{\rho_1} \cong 1$ and can be identified with half the typical cluster size, $\lambda_{\text{clus}}/2$. Thus $\lambda_{\text{clus}}\sqrt{\rho_1} \cong 2$, a value agreeing well with the structural data extracted from fig. 3.4. There, the estimate $\lambda_{\text{clus}}\sqrt{\rho_2} \cong 1.27$ was made, thus $\lambda_{\text{clus}}\sqrt{\rho_1} \cong 1.8$ for the density ratio at hand. The morphological estimate is based on the consideration that, when the covering circles attain a value equal to half the cluster size, covering patches from neighboring clusters overlap, leaving one or more holes in the space in between. And since every hole contributes -1 to the Euler characteristic, the minimum of $\langle X \rangle$ is expected for such values of R_0. Closing now these holes requires a much larger cover radius than in the ideal gas system wherein particles are more or less evenly dispersed over the whole area.

The $\langle X \rangle/N$ vs. R_0 curves for the big particles reveal that the gaps between them are *smaller* than for the one-component case. This is consistent with the fact that the big particles are rearranging and open small voids in which the small ones are accommodated. In addition, the most negative value of $\langle X \rangle/N$ is achieved for the one-component system. This is also reasonable, since the large voids that open up for the small particles constitute a single hole and thus drive $\langle X \rangle/N$ less negative than the many smaller holes present in the absence of the voids. The $\langle X \rangle$ vs. R_0 curves of the big and the small particles have very different shapes; there is no way to scale one on top of the other. This reveals also from the morphological point of view the very different spatial arrangements of the two species in the presence of one another.

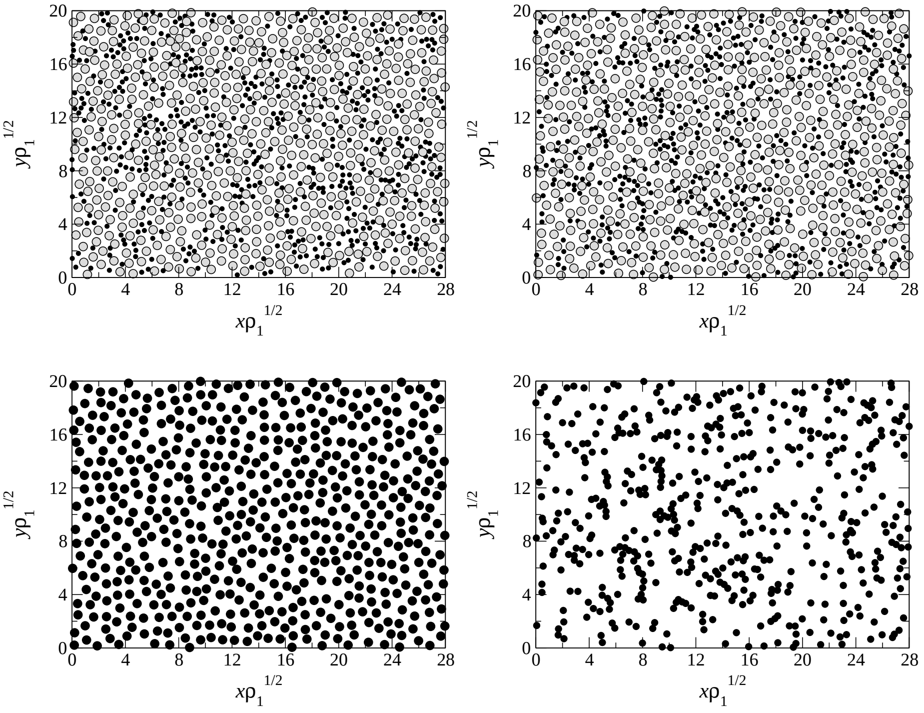

Figure 3.13: Snapshots of the binary magnetic mixture from experiment and simulation for the parameter combination $\Gamma_{11} = 4.05$, $\rho_2/\rho_1 = 0.89$, $\chi_2/\chi_1 = 0.1$. The big particles are denoted gray and the small ones black. Clockwise from the upper left panel: experiment, simulation (both species), simulation (small particles only) and simulation (big particles only).

3.6 Comparison: experiment vs. theory

A comparison between the theoretical and experimental structure factors is shown in fig. 3.12, pertaining to susceptibility ratio $\chi_2/\chi_1 = 0.1$ and corresponding to the real experimental situation. The representative results are shown here for density ratio $\rho_2/\rho_1 = 0.89$ and coupling constant $\Gamma_{11} = 4.05$. Very good agreement between theory and experiment is achieved, supporting the modeling of the system by means of dipolar interactions exclusively; evidently, all other residual forces in the colloidal suspension are much weaker and can be neglected. A pre-peak is seen in the small-particle structure factor $S_{22}(k)$, whose height is comparable with that of the second peak due to the small value of χ_2. Indeed, as the second peak arises from pure small-small interactions, its height is suppressed since the latter scale as χ_2^2. The prepeak trivially disappears in both limits $\chi_2/\chi_1 \to 0$ and $\chi_2/\chi_1 \to 1$.

Further evidence of the subclustering phenomenon is provided by real-space data.

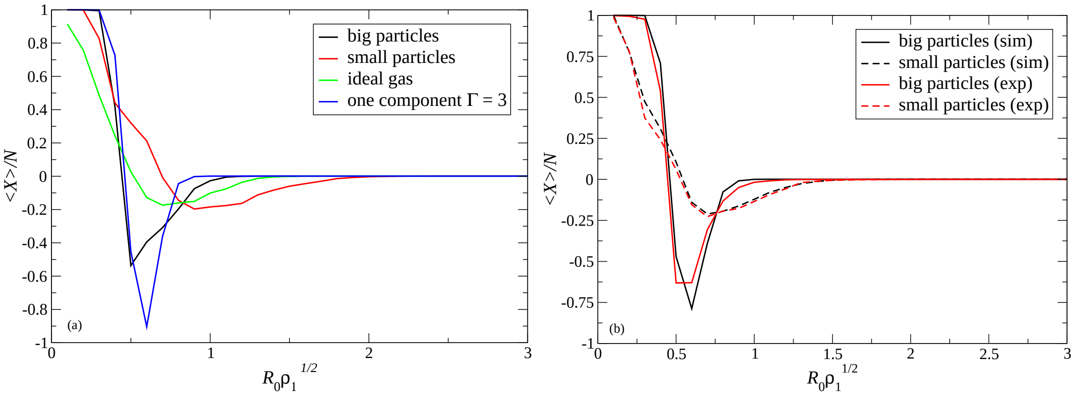

Figure 3.14: (a) Euler characteristic per particle, $\langle X \rangle / N$, as obtained from simulation for $\Gamma_{11} = 3.0$, $\rho_2/\rho_1 = 0.5$, $\chi_2/\chi_1 = 0.5$; (b) Comparison of the theoretical (black lines) and experimental (gray lines) results for the same quantity for the parameters $\Gamma_{11} = 4.05$, $\rho_2/\rho_1 = 0.89$, $\chi_2/\chi_1 = 0.1$. Solid lines: big particles; dashed lines: small particles.

In fig. 3.13 we show experimental and simulation snapshots of the system under consideration. We observe a cluster structure of the smaller particles that perfectly fits in the voids shaped by the big particles. To better quantify the morphology of the spatial patterns, we employ tools from integral geometry, and in particular the Euler characteristic X, which describes the topology of the pattern [78] and has been introduced in the last section.

In fig. 3.14(a), we show the X-curves of the two components of a binary mixture, compared to a one-component and an ideal gas system. The underlying snapshots are taken from simulation data. The Euler characteristic of the small component tends to zero much more slowly than the ideal gas curve. For the ideal gas, the particles are more or less evenly spread over the area, so the vacant space between the particles can be filled much faster than in the two-component case where the inter-aggregate space between the small particles is larger. A comparison between the big component and the one-component system reveals that the Euler characteristic of the former becomes less negative and tends to zero much more slowly due to the larger voids caused by the aggregation of the small component. Fig. 3.14(b) refers to the parameter combination of the experimental sample. There, the $\langle X \rangle / N$ vs. R_0-curves from simulation and experiment are compared, showing very good agreement. The pre-peak position in fig. 3.12(b) points to a typical cluster size $\lambda_{\mathrm{cl}} \sqrt{\rho_1} \cong 1.26$ which agrees well with the position of the most negative value of $\langle X_2 \rangle$ from fig. 3.14(b) and is consistent with the large holes left there when the covering circle radius $R_0 \cong \lambda_{\mathrm{cl}}/2$. The partial clustering is caused by the interplay between the successively stronger repulsive interactions $u_{22}(r) < u_{12}(r) < u_{11}(r)$, which preclude macrophase separation and favor the nesting of small particles in the voids of the big ones.

3.7 Conclusions

We have investigated partial cluster formation in a two-component colloidal model system characterized by simple dipole-dipole interactions. The system is experimentally accessible and our results have been confirmed by measurements for specific parameter combinations. The small-particle clusters do not form well-separated, monodisperse domains with a well-defined geometrical shape, such as those seen for interactions with a short-range attraction and a long-range repulsion [67]. They are rather diffuse, possess a percolating, sponge-like topology, with a significant number of holes. We have analyzed this phenomenon in terms of the non-additivity parameter of the mixture and we put forward the assertion that it is a general property for all mixtures with $\Delta < 0$, whose interactions are purely repulsive and additionally obey the inequalities $u_{22}(r) < u_{12}(r) < u_{11}(r)$.

Chapter 4

Superparamagnetic Colloids with Anisotropic Interaction

In this chapter we outline the formalism of liquid integral equation theory for anisotropic interaction in two dimensions. We apply this theory to one-component superparamagnetic particles exposed to a tilted magnetic field. Inhomogeneous local ordering of the particles is observed for different in-plane directions. The anisotropy of the interaction as well as of the liquid structure is increased by increasing the tilt angle. Furthermore, the particles favor an alignment in direction of the in-plane component of the magnetic field.

4.1 Theory

We consider a two-dimensional system of N colloidal particles in a plane of surface area A. With $\rho = N/A$ denoting the system's density we define the characteristic length as $a \equiv 1/\sqrt{\rho}$. The particles are exposed to an external magnetic field $\mathbf{B}$ that can be tilted with respect to the two-dimensional plane. This external field induces a magnetic moment $\mathbf{m}_i$ onto each particle. The colloids are assumed to be superparamagnetic, *i.e.*, the magnetic moment of each particle aligns perfectly with the external field

$$\mathbf{m} = \chi \mathbf{B_0}, \tag{4.1}$$

with the proportionality constant χ being the particle's susceptibility. For strong fields, this assumption proves to be reasonable and valid. The colloids are of finite extent with a hard core radius σ. The particles interact with each other via a dipole-dipole pair potential, valid for point-like magnetic dipoles,

$$u_{\mathrm{dd}}(\mathbf{r}, \mathbf{m_i}, \mathbf{m_j}) = \frac{\mathbf{m_i} \cdot \mathbf{m_j} - \mathbf{3}(\mathbf{m_i} \cdot \hat{\mathbf{n}})(\mathbf{m_j} \cdot \hat{\mathbf{n}})}{\mathbf{r^3}}, \tag{4.2}$$

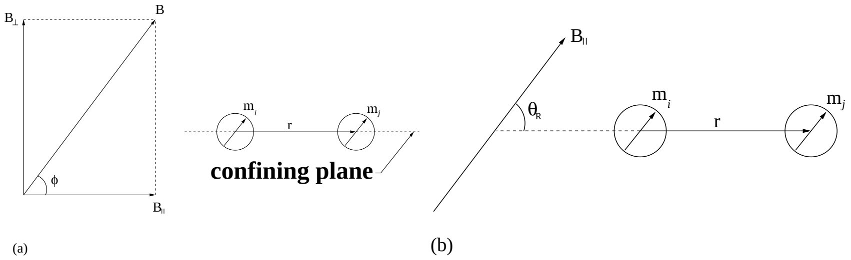

Figure 4.1: A schematic view of two superparamagnetic colloids to a plane exposed to a tilted external magnetic field **B**: (a) side view; (b) top view.

for distances larger than or equal to their hard core radius; $\hat{\mathbf{n}}$ is the unit vector connecting the centers of a pair of discs. For distances smaller than the hard core radius the interaction is described by a hard core repulsion. Using the aforementioned length scale a, we introduce the so-called coupling strength, a dimensionless parameter that reads as

$$\Gamma = \beta \frac{(\chi B_0)^2}{a^3}, \tag{4.3}$$

where $\beta = 1/(k_{\mathrm{B}}T)$, with k_{B} being Boltzmann's constant and T being the absolute temperature. Rescaling the particle coordinates with the interparticle distance, $r_i \rightarrow x_i \equiv r_i/a$, and using eqs. (4.1) and (4.3), we can re-write the dipole-dipole interaction potential, eq. (4.2), as

$$\beta u(x) = \frac{\Gamma}{x^3}(1 - 3\cos^2\phi\cos^2\theta_R), \tag{4.4}$$

with $x = |\mathbf{x}_1 - \mathbf{x}_2|$ and $\cos\theta_R = \mathbf{r} \cdot \mathbf{B}_{\|}/(rB_{\|})$, $\mathbf{B}_{\|}$ is the in-plane component of the magnetic field. ϕ denotes the angle between the magnetic field and its projection to the confining plane.

4.2 Liquid integral equation theory for anisotropic interactions

The radial distribution function $g(\mathbf{r})$, or equivalently the indirect correlation function

$$h(\mathbf{r}) = g(\mathbf{r}) - 1 \tag{4.5}$$

is a quantity of central interest for classical fluids in equilibrium. The radial distribution function measures the extent to which the structure of a fluid deviates from complete randomness and expresses the ordering of the rest of the system around a given particle of the liquid. It plays a key role in liquid theory because some important thermodynamic properties, such as the internal energy of the system, can be written as integrals over $g(r)$.

4.2.1 Basics

The liquid integral equation theory consists of the Ornstein-Zernike (OZ) relation

$$h(\mathbf{r}) = c(\mathbf{r}) + \rho \int \mathrm{d}\mathbf{r}' h(\mathbf{r} - \mathbf{r}') c(\mathbf{r}') \tag{4.6}$$

coupled with a closure relation. We have settled for the hypernetted chain closure (HNC) for reasons to become clear in what follows. The HNC can be written in the form

$$c(\mathbf{r}) = h(\mathbf{r}) - \ln g(\mathbf{r}) - \beta u(\mathbf{r}), \tag{4.7}$$

with $c(\mathbf{r})$ denoting the direct correlation function and $\beta u(\mathbf{r})$ the pair interaction potential as explained above. The eqs. (4.6) and (4.7) cannot be solved analytically, but a solution can be obtained numerically by an iterative scheme. For convenience we introduce the function

$$\gamma(\mathbf{r}) = h(\mathbf{r}) - c(\mathbf{r}) \tag{4.8}$$

in order to cast the OZ relation in the following form

$$\gamma(\mathbf{r}) = \rho \int \mathrm{d}\mathbf{r}' [\gamma(\mathbf{r} - \mathbf{r}') + c(\mathbf{r} - \mathbf{r}')] c(\mathbf{r}'). \tag{4.9}$$

For potentials with a hard core part, $h(\mathbf{r})$ and $c(\mathbf{r})$ are separately discontinuous at the hard core radius. The incorporated function $\gamma(\mathbf{r})$ is devoid of that discontinuity, and therefore a strictly continuous function. Nevertheless, solving eqs. (4.7) and (4.9) is very difficult because each function depends on four variables and the integration in eq. (4.9) goes over all the four position and angular coordinates. In order to simplify and solve the equations, we expand the correlation function into a basis set of orthogonal functions. This expansion leads to an easily tractable form of the OZ equation. Then, it is possible to expand the HNC closure analytically to all orders in the same basis set, hence allowing a solution of eq. (4.7) and (4.9).

4.2.2 Expansion

In order to reduce the complexity of solving the two coupled integral equations, we expand all correlation functions into a set of orthogonal functions. Because we are working in a two-dimensional system, the complex exponential function seems a natural choice for an orthogonal basis set. Exemplary, we just show the direct correlation function as a representative for all correlation functions

$$c(\mathbf{r}) = \sum_m c_m(r) \exp(-im\theta_R) \tag{4.10}$$

with θ_R denoting the angle between $\mathbf{r}$ and the x-axis aligned along $\mathbf{B}_\parallel$ as introduced in sec. 4.1 and identifying $\mathbf{r} \equiv (r, \theta_R)$. Due to symmetry, this expansion can be rewritten as

$$c(\mathbf{r}) = c_0(r) + \sum_{|m|\neq 0} c_{|m|}(r) \cos(m\theta_R) \tag{4.11}$$

with

$$c_{|m|}(r) = \begin{cases} \frac{1}{\pi} \int\limits_0^\pi \mathrm{d}\theta_R \, c(\mathbf{r}) & \text{for } m = 0 \\ \frac{2}{\pi} \int\limits_0^\pi \mathrm{d}\theta_R \, c(\mathbf{r}) \cos(m\theta_R) & \text{for } m \neq 0 \end{cases}$$

whereas m has to be an even number.

The interaction potential can be expanded in the same basis set as the correlation functions and is fully determined by the first two coefficients with the remaining terms vanishing:

$$\beta u_0(r) = \beta \frac{(\chi B_0)^2}{r^3} \left(1 - \frac{3}{2} \cos^2 \phi\right), \tag{4.12}$$

$$\beta u_2(r) = -\beta \frac{3}{2} \frac{(\chi B_0)^2}{r^3} \cos^2 \phi. \tag{4.13}$$

Solving eqs. (4.7) and (4.9) simultaneously requires the expansion of the HNC closure in the same set of basis functions as all the other correlation functions. At first sight, it seems that the logarithmic term in eq. (4.7) causes trouble, but this problem has been overcome in a surprisingly simple manner by Fries and Patey [89].

Partial differentiation of eq. (4.7) with respect to r yields

$$\frac{\partial c(r, \theta_R)}{\partial r} = -h(r, \theta_R) \frac{\partial W(r, \theta_R)}{\partial r} - \beta \frac{\partial u(r, \theta)}{\partial r}, \tag{4.14}$$

with introducing $W(r, \theta_R) \equiv -\gamma(r, \theta) + \beta u(r, \theta_R)$ as the dimensionless angle-dependent potential of mean force. Now, since $c(r, \theta_R) \to -\beta u(r, \theta_R)$ as $r \to \infty$, it is clear that

$$\int_r^\infty \mathrm{d}r' \frac{\partial c(r', \theta_R)}{\partial r'} = [c(r = \infty, \theta_R) - c(r, \theta_R)] = -c(r, \theta_R). \tag{4.15}$$

Combining eqs. (4.14) and (4.15), the HNC closure reads as

$$c(r,\theta_R) = \int_r^\infty \mathrm{d}r' h(r',\theta_R)\frac{\partial W(r',\theta_R)}{\partial r'} - \beta u(r,\theta_R). \tag{4.16}$$

The advantage of writing the HNC closure like this amounts to the analytical expansion of the binary product $-h(r,\theta_R)[\partial W(r,\theta_R)/\partial r]$ in the common basis set. After some algebra, we obtain

$$c(r,\theta_R) = \sum_m \sum_{n=0}^{m} I_{n,m-n}(r)\exp(-im\theta_R) - \beta\sum_m u_m(r)\exp(-im\theta_R), \tag{4.17}$$

with

$$I_{m,n}(r) = \int_r^\infty \mathrm{d}r' h_m(r',\theta_R)\frac{\partial W_n(r',\theta_R)}{\partial r'}. \tag{4.18}$$

For distances smaller than the hard core radius σ the radial distribution function is zero, hence the direct correlation function can be calculated by means of eq. (4.8) as

$$c(r,\theta) = -1 - \gamma(r,\theta_R) \ \text{ for } r < \sigma \tag{4.19}$$

4.2.3 Fourier transform

The OZ relation can be significantly simplified by expanding the correlation function in a basis set of orthogonal functions. In solving the two coupled integral equations, the OZ and the HNC closure invoke an iterative procedure that requires the repeated calculation of convolution integrals. These are evaluated most efficiently and rapidly in reciprocal space. Therefore we first transform the OZ relation to reciprocal space in order to render the convolution integral into a simple product. Then, we plug the expansion of correlation functions in reciprocal space into the OZ relation.

We define the Fourier transform for an arbitrary, physically smooth function $f(\mathbf{r})$ in 2d as follows

$$f(\mathbf{r}) = \frac{1}{(2\pi)^2}\int \mathrm{d}\mathbf{k}\, \tilde{f}(\mathbf{k})\exp(-i\mathbf{k}\mathbf{r}) \tag{4.20}$$

and its inverse

$$\tilde{f}(\mathbf{k}) = \int \mathrm{d}\mathbf{r}\, f(\mathbf{r})\exp(i\mathbf{k}\mathbf{r}). \tag{4.21}$$

Then, the OZ relation (4.9) can be written in Fourier space as

$$\tilde{\gamma}(\mathbf{k}) = \rho\tilde{c}(\mathbf{k})[\tilde{\gamma}(\mathbf{k}) + \tilde{c}(\mathbf{k})]. \tag{4.22}$$

The correlation functions in reciprocal space are obtained by applying the Fourier transform (4.20) to the corresponding ones in real space. Exemplary, we show the direct correlation function

$$\tilde{c}(\mathbf{k}) = \int \mathrm{d}\mathbf{r}\, c(\mathbf{r}) \exp(i\mathbf{k}\mathbf{r}). \tag{4.23}$$

The expansion in Fourier space can be written as

$$\tilde{c}(\mathbf{k}) = \sum_m \tilde{c}_m(k) \exp(-im\theta_K) \tag{4.24}$$

with

$$\tilde{c}_m(k) = 2\pi i^m \int_0^\infty \mathrm{d}r\, r c_m(r) J_m(kr). \tag{4.25}$$

Here, θ_K in Fourier space is the equivalent to θ_R in real space and $J_m(r)$ is the m-th order Bessel function of the first kind. Conversely, the coefficients of the expansion in reciprocal space are obtained by a simple Hankel transform of the coefficient in real space. Thus, it holds

$$c_m(r) = (2\pi)^{-1} i^m \int_0^\infty \mathrm{d}k\, k\tilde{c}_m(k) J_m(kr). \tag{4.26}$$

We see that the coefficients of the expansion in Fourier and real space are connected by a simple Hankel transform. In the appendix, we show a strict derivation of the interconnection between the coefficients in real and Fourier space.

We want to point out explicitly that the angle θ_R in the real space expansion and the angle θ_K in the reciprocal space expansion are different. In each system, it is the in-plane angle between the in-plane magnetic field and the r- and k-vector, respectively.

The problem of calculating the Hankel transform of m-th order

$$\tilde{f}(\mathbf{k}) = 2\pi i^m \int_0^\infty \mathrm{d}r\, r f(r) J_m(kr), \tag{4.27}$$

can be reduced to the 0-th order Hankel transform,

$$\tilde{f}(\mathbf{k}) = 2\pi i^m \int_0^\infty \mathrm{d}r\, r f(r) J_0(kr). \tag{4.28}$$

Lado developped a numerically accurate algorithm for that procedure [93] and for the calculation of the 0-th order Hankel transform in an efficient way [90]. For the reduction, we need two recurrence relations for the Bessel functions [91],

$$\begin{aligned} \frac{\mathrm{d}}{\mathrm{d}x}\left[\frac{J_{m-1}(x)}{x^{m-1}}\right] &= -\frac{J_m(x)}{x^{m-1}}, && (4.29) \\ \frac{\mathrm{d}}{\mathrm{d}x}\left[x^m J_{m-1}(x)\right] &= x^m J_{m-2}(x). && (4.30) \end{aligned}$$

Exploiting the first recurrence relation, eq. (4.29), in eq. (4.27) and an integration by parts leads to the following expression with $f(k)$ vanishing sufficiently rapidly at infinity:

$$\tilde{f}(k) = \frac{1}{k}\int_0^\infty \mathrm{d}r \frac{\mathrm{d}}{\mathrm{d}r}\left[r^m f(r)\right]\frac{J_{m-1}(kr)}{r^{m-1}}. \tag{4.31}$$

We set $f(r) \equiv f^{(m)}(r)$ and define a new function $f^{(m-2)}(r)$ such that

$$\frac{\mathrm{d}}{\mathrm{d}r}\left[r^m f^{(m)}(r)\right] = r^{2m-2}\frac{\mathrm{d}}{\mathrm{d}r}\left[\frac{f^{(m-2)}(r)}{r^{m-2}}\right]. \tag{4.32}$$

Plugging eq. (4.32) into eq. (4.31) leads to

$$\begin{aligned} \tilde{f}(k) &= \frac{1}{k}\int_0^\infty \mathrm{d}r r^{2m-2}\frac{\mathrm{d}}{\mathrm{d}r}\left[\frac{f^{(m-2)}(r)}{r^{m-2}}\right]\frac{J_{m-1}(kr)}{r^{m-1}} \\ &= \int_0^\infty \mathrm{d}r \frac{1}{r}\frac{\mathrm{d}}{\mathrm{d}r}\left[\frac{f^{(m-2)}(r)}{r^{m-2}}\right]\int_0^r \mathrm{d}x x^m J_{m-2}(kx) \\ &= -\int_0^\infty \mathrm{d}r r f^{(m-2)}(r) J_{m-2}(kr), \end{aligned} \tag{4.33}$$

where in the first step we used the second recurrence relation, eq. (4.29), and in the next step we integrated by parts.

Finally, we have to identify the function $f^{(m-2)}(r)$ from $f^{(m)}(r)$. Therefore, we integrate eq. (4.32)

$$\int_r^\infty \mathrm{d}r' \frac{\mathrm{d}}{\mathrm{d}r'}\left[(r')^m f^{(m)}(r')\right] = \int_r^\infty \mathrm{d}r'(r')^{2m-2}\frac{\mathrm{d}}{\mathrm{d}r'}\left[\frac{f^{(m-2)}(r')}{(r')^{m-2}}\right]. \tag{4.34}$$

Performing the integration yields

$$f^{(m-2)}(r) = f^{(m)} - 2(m-1)r^{m-2}\int_r^\infty \mathrm{d}r' \frac{1}{(r')^{m-1}} f^{(m)}(r'). \tag{4.35}$$

We apply repetitively this 'step-down' operation until we reach

$$f^{(0)}(r) = f^{(2)} - 2\int_r^\infty \mathrm{d}r' \frac{1}{r'} f^{(2)}(r'). \tag{4.36}$$

Then, we transform $f^{(0)}(r)$ by a 0th-order Hankel transform [90].
Similarly, it can be shown that for the inverse m-th order Hankel transform the following scheme holds:

(1) First, we transform the original function $\tilde{f}(k) \equiv \tilde{f}^{(0)}(k)$ by a simple 0-th order Hankel transform in order to obtain $f^{(0)}(r)$.

(2) Then, we apply the following expression repetitively until the desired order of m is reached

$$f^{(m)}(r) = f^{(m-2)}(r) - \frac{2(m-1)}{r^m} \int_0^r \mathrm{d}x \, x^{m-1} f^{(m-2)}(x). \tag{4.37}$$

The latter integral as well as the integral in eq. (4.35) can be calculated using a simple trapezoidal rule.
Because the direct correlation function $c(r)$ behaves asymptotically as the potential,

$$c(r) \sim -\beta u(r) \sim \frac{1}{r^3}, \quad (r \to \infty), \tag{4.38}$$

the long-range nature of the correlation function may adversely affect the Fourier transform due to a necessary truncation of the former one at a finite cut-off value. We can bypass that problem by subtracting a function with equal long-range behavior and an analytically known Hankel transform. The Fourier transform of that difference does not entail any difficulties and the Hankel transform of the subtracted function is added back in reciprocal space.
For the coefficient $c_0(r)$, we subtract

$$\begin{aligned} \beta u_{\mathrm{LR},0}(r;\alpha) &= \frac{\Gamma}{r^3}\left[1 - \exp(-\alpha r)\left(1 + \alpha r + \frac{1}{2}\alpha^2 r^2\right)\right] \\ &= \frac{1}{2}\Gamma\alpha^3 \int_0^1 \mathrm{d}x x^2 \exp(-\alpha r x), \end{aligned} \tag{4.39}$$

with the analytical Hankel transform

$$\widetilde{\beta u_{\mathrm{LR},0}}(k;\alpha) = \pi\Gamma_0 \left[\frac{2k^2 + \alpha^2}{\sqrt{k^2 + \alpha^2}} - 2k\right]. \tag{4.40}$$

For the coefficient $c_2(r)$, the following function proves to be apt:

$$\begin{aligned} \beta u_{\mathrm{LR},2}(r;\alpha) &= \frac{\Gamma}{r^3}\left[1 - \exp(-\alpha r)\left(1 + \alpha r + \frac{1}{2}\alpha^2 r^2 + \frac{1}{6}\alpha^3 r^3\right)\right] \\ &= \frac{1}{6}\Gamma\alpha^4 r \int_0^1 \mathrm{d}x x^3 \exp(-\alpha r x), \end{aligned} \tag{4.41}$$

whose Hankel transform reads as

$$\widetilde{\beta u_{\mathrm{LR},2}}(k;\alpha) = -\frac{\pi}{3}\Gamma k^2 \left(\frac{2}{k} - \frac{3\alpha^2 + 2k^2}{(\alpha^2 + k^2)^{3/2}}\right) \tag{4.42}$$

The parameter α can freely be chosen.
It is worth noting to treat the discontinuity in $c(r)$ carefully by doing the Fourier transform. We apply the Dirichlet condition at this position to guarantee correct results. This condition says that for a function with a discontinuity at r_0 the Fourier transform at this position is just the Fourier transform of the mean value of the lower and upper value.

4.2.4 Ornstein-Zernike relation

Our initial goal was to cast the Ornstein-Zernike relation in a numerically tractable form. First, we broke up its integral in a simple product by passing over to Fourier space. Then, we outlined the series expansion in Fourier space. The final step comprises plugging the series expansion in reciprocal space, eq. (4.24), into the Fourier transformed Ornstein-Zernike relation, eq. (4.22), yielding the following result:

$$\tilde{\gamma}_p(k) = \rho \sum_m \tilde{c}_m(k)\tilde{\gamma}_{(p-m)} + \tilde{c}_m(k)\tilde{c}_{(p-m)}. \tag{4.43}$$

Restricting to a limited number M of coefficients in the series expansion, the Ornstein-Zernike relation provides a $M \times M$ linear algebraic system which can be solved by standard numerical algorithms.

4.2.5 Algorithm

The elements developed above are necessary ingredients in analyzing the two coupled integral equations (4.6) and (4.7). The whole procedure to solve these equations is best presented in summary form. One iteration for calculating the $c_m(r)$ consists of the following steps:

1. Subtract from the coefficients $c_0(r)$ and $c_2(r)$ the functions

$$\beta u_{\mathrm{LR},0}(r;\alpha) = \frac{\Gamma_0}{r^3}\left[1 - \exp(-\alpha r)\left(1 + \alpha r + \frac{1}{2}\alpha^2 r^2\right)\right] \tag{4.44}$$

and

$$\beta u_{\mathrm{LR},2}(r;alpha) = \frac{\Gamma_0}{r^3}\left[1-\exp(-\alpha r)\left(1+\alpha r+\frac{1}{2}\alpha^2 r^2+\frac{1}{6}\alpha^3 r^3\right)\right], \quad (4.45)$$

respectively.

2. Lower the coefficients $c_m(r)$ to get

$$c^{(m-2)}(r) = c^{(m)} - 2(m-1)r^{m-2}\int_r^\infty \mathrm{d}r' \frac{1}{r'^{m-1}} c^{(m)}(r') \quad (4.46)$$

starting from $c_m^{(l)}(r) \equiv c_m(r)$ and ending up with $c_m^{(0)}(r)$.

3. Convert $c_m^{(0)}(r)$ by a 0-th order Hankel transform due to the procedure outlined in ref [90] to get $\tilde{c}_m(k)$. Be aware of the discontinuity at the hard core radius and apply the Dirichlet condition described at the end of section 4.2.3.

4. Add the analytically calculated Hankel transforms

$$\widetilde{\beta u_{\mathrm{LR},0}}(k;\alpha) = \pi\Gamma_0\left[\frac{2k^2+\alpha^2}{\sqrt{k^2+\alpha^2}} - 2k\right] \quad (4.47)$$

and

$$\widetilde{\beta u_{\mathrm{LR},2}}(k;\alpha) = -\frac{\pi}{3}\Gamma_2 k^2\left(\frac{2}{k} - \frac{3\alpha^2+2k^2}{(\alpha^2+k^2)^{3/2}}\right) \quad (4.48)$$

back to the coefficients $c_0(k)$ and $c_2(k)$.

5. Plug $c_m(k)$ into the Ornstein-Zernike relation

$$\tilde{\gamma}_p(k) = \rho\sum_m \tilde{c}_m(k)\tilde{\gamma}_{(p-m)} + \tilde{c}_m(k)\tilde{c}_{(p-m)} \quad (4.49)$$

to get $\tilde{\gamma}_m(k) \equiv \tilde{\gamma}_m^{(0)}(k)$.

6. Apply to these the inverse 0-th order Hankel transform to get the $\gamma_m^{(0)}(r)$

7. Raise these according to:

$$\gamma^{(m)}(r) = \gamma^{(m-2)}(r) - \frac{2(m-1)}{r^m}\int_0^r \mathrm{d}x x^{m-1}\gamma^{(m-2)}(x). \quad (4.50)$$

8. Plug these into

$$c(r,\theta_R) = \int_r^\infty \mathrm{d}r' h(r',\theta_R)\frac{\partial W(r',\theta_R)}{\partial r'} - \beta u(r,\theta_R). \tag{4.51}$$

for distances larger than oder equal to the hard core diameter and

$$c(r,\theta_R) = -1 - \gamma(r,\theta_R) \tag{4.52}$$

for distances smaller than that diameter. For the derivative in the first equation, we apply a 7-point derivative scheme for unevenly spaced notes [92].

This iterative scheme is repeated until convergence for $c_m(r)$ is achieved. To guarantee convergence, we mix the new $c_m(r)$ with the result of the former iterative step

$$c_{\text{new}}(r) = \zeta c_{\text{new}}(r) + (1-\zeta)c_{\text{old}}(r). \tag{4.53}$$

The so-called mixing parameter $0 < \zeta < 1$ is chosen empirically to assure convergence. The whole iterative scheme is best started with the Mayer function $f(r)$

$$f(r) = \exp(-\beta u(r)) - 1 \tag{4.54}$$

which is exact in the zero density limit. We recommend starting the above scheme with a small density and proceeding through the outlined steps until convergence is reached, and then we slightly increase the density, repeat the iterative scheme again and then further increase the density until the desired density is obtained.

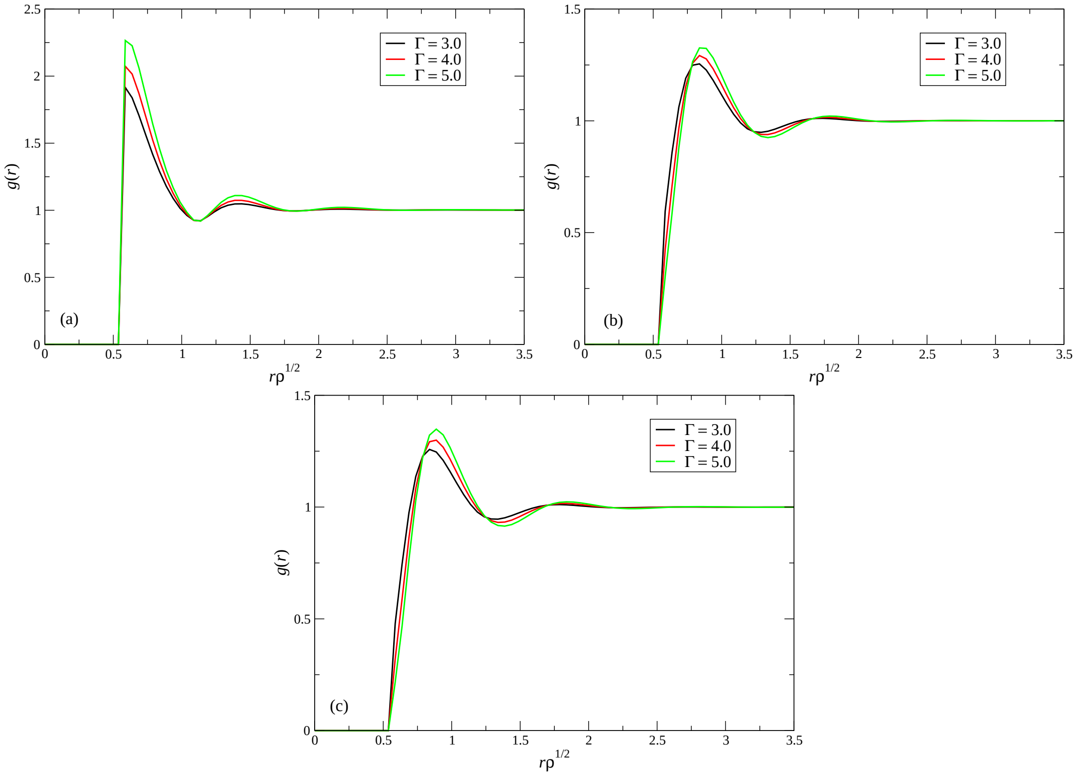

Figure 4.2: The radial distribution function for different tilt and in-plane angles (a) $\phi = 60°$, $\theta_\mathrm{R} = 0°$, (b) $\phi = 75°$, $\theta_\mathrm{R} = 30°$, and (c) $\phi = 85°$, $\theta_\mathrm{R} = 60°$.

4.3 Results

We numerically solve the two coupled integral equations (eqs. (4.6) and (4.7)), according to the theory outlined in the previous section.
First, we increase the interaction strength Γ for a host of arbitrary parameter combinations of the tilt angle ϕ and the in-plane angle θ_R. The results are shown in fig. 4.2. For the same parameters the peak heights increase with increasing interaction strength while the peak positions remain nearly unchanged. This behavior is physically plausible: we can assume that the interaction strength is increased by turning the magnetic field $\mathbf{B_0}$ stronger while the number of particles remains unchanged. Therefore, the typical interparticle distance is not altered, but the degree of local ordering is affected, leading to a more pronounced liquid structure.

Now, we are interested in the local ordering of the particles for different in-plane directions while keeping the interaction strength and the tilt angle fixed. The results are shown in fig. 4.3 for different fixed tilt angles. In contrast to the case of

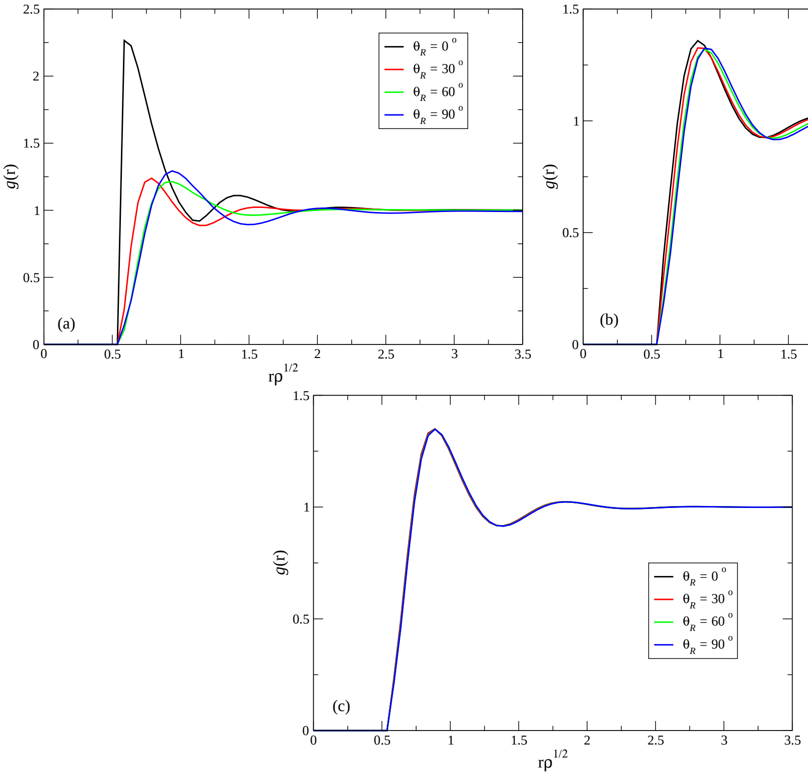

Figure 4.3: The radial distribution function for fixed $\Gamma = 5.0$ and different tilt angles (a) $\phi = 60°$, (b) $\phi = 75°$, and (c) $\phi = 85°$.

a perpendicular field, the radial distribution functions for different in-plane angles do not coincide anymore. This effect is clearly traced back to the anisotropy of the interaction induced by the tilted magnetic field. We realize for all tilt angles that the local structure is most pronounced in direction of the in-plane component of the external field. The dipole-dipole interaction favors fully aligned moment, *i.e.*, head-to-tail configuration, in agreement with previous results [28]. Furthermore, the deviation among the different local radial distribution functions increases with increasing tilt angle. The differences are most obviously observed for $\phi = 60°$ whereas for $\phi = 85°$ we barely recognize any significant distinctions. We can understand this by the growth of anisotropy with larger tilt angles.

Now, we explicitly compare different tilt angles ϕ for fixed interaction strength and fixed in-plane angles θ_{R}. We present the results in fig. 4.4 for different fixed in-plane angles. Only for the in-plane direction of the magnetic field the structure is more pronounced the more the field is tilted. While always working in the repulsive regime, the repulsion between head-to-tail configurations become weaker, leading to

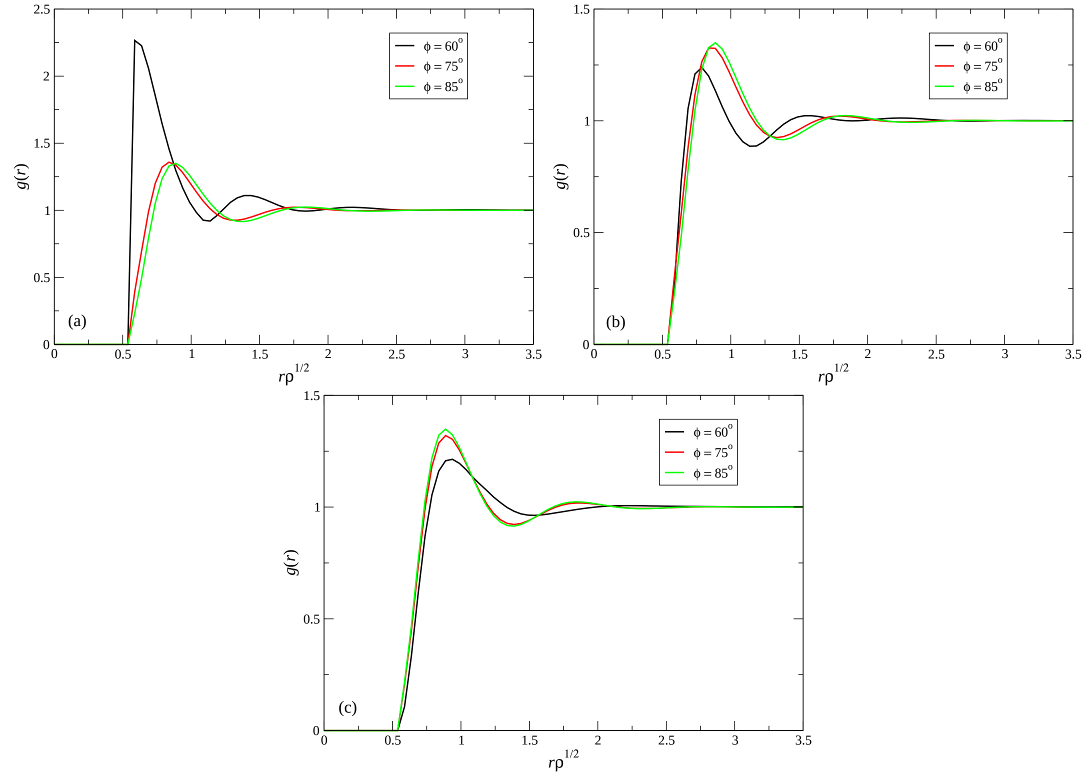

Figure 4.4: The radial distribution function for fixed $\Gamma = 5.0$ and different in-plane angles (a) $\theta_{\mathrm{R}} = 0°$, (b) $\theta_{\mathrm{R}} = 30°$, and (c) $\theta_{\mathrm{R}} = 60°$.

a stronger alignment among the particles in the field in-plane direction. This does not hold true for any other in-plane direction and therefore no predictions of the heights of the different local ordering can be made.

4.4 Conclusions

In this chapter, we have derived the formalism of integral equation theory for an anisotropic interaction. We have expanded all correlation functions in a set of orthogonal functions to cast the integral equation in a numerically accessible form. The cumbersome task of a two-dimensional, fast Fourier transform has been tackled by the introduction of Hankel transforms of higher orders. These could be in turn reduced to easily calculable 0th-order Hankel transforms.

Due to the anisotropy of the interaction with tilted magnetic field, the local ordering of the particles becomes inhomogeneous. The local structure of the liquid turns more inhomogeneous with increasing tilt angle. An alignment of particles in direction of the in-plane component of the magnetic field is observed.

Chapter 5

Proteins

In this chapter we calculate the electrostatic potential of proteins by assuming them as spherical particles with non-spherical charge patterns. We derive analytical expressions for the screened electrostatic potential caused by a charged spherical colloid that contains point charges distributed in an arbitrary manner in its interior. We consider both the cases of uniform and discontinuous dielectric constants. The solution is based on an expansion of the electrostatic potentials on the various regions of space in spherical harmonics involving spherical Bessel functions of the third kind. Tetrahedral charge arrangements as well as a random charge distribution inside the confining sphere are considered explicitly as representative examples.

5.1 Introduction

Electrostatic interactions play a crucial role in determining the structure and stability of colloidal dispersions or biomolecular aggregates [50]. In the much studied case of aqueous dispersions of micron-sized spherical colloidal particles, the traditional Derjaguin-Landau-Verwey-Overbeek (DLVO) [94] description is based on the explicit assumption of a spherically symmetric charge distribution carried by the particles. According to Gauss' law such a distribution is equivalent to having the total charge of the particle located at its centre, implying a purely radial effective interaction between colloidal particles which is usually calculated within Poisson-Boltzmann, or linearized Poisson-Boltzmann (LPB) theory. The fact that microscopic co- and counterions cannot penetrate the spherical polyions is incorporated in a simple geometric factor in the DLVO potential, equivalent to enhancing the bare charge Ze of the polyions to an effective charge $Z_{\text{eff}} > Z$ [94]. The assumption of a uniformly distributed surface charge is reasonable on the colloidal scale in view of the high values of Z resulting from typical surface charges of up to an elementary charge per nm^2. This is no longer true when one goes down to the nanometer scale relevant for most biomolecules. We shall be more specifically concerned with globular proteins, which will be modeled by spherical particles carrying typically of the order of 10 charged sites distributed in a non spherically symmetric pattern over the particle volume. The ultimate goal of our work is to determine the screened Coulomb interaction between two globular proteins carrying arbitrary discrete charge patterns in the presence of co- and counterions, taking proper account of excluded volume effects and of dielectric discontinuities. These calculations will still be carried out within the framework of the "primitive model", *i.e.*, the aqueous solvent will be considered to be a mere dielectric continuum. Discrete solvent effects can have a dramatic influence on effective interactions between charged proteins [95], but recent Molecular Dynamics simulations clearly show that switching from continuous to discrete charge patterns in model spherical proteins already leads to highly significant differences between the resulting screened Coulomb interactions reflected, *e.g.*, in different concentration dependences of the calculated second virial coefficients [96].

Screened electrostatic interactions between non-spherically symmetric charged particles have been calculated recently for the case of charged platelets [97, 98]. There, however, due to the infinitely thin shape of the platelets, the charge on the colloids is immediately exposed to the solvent and no 'finite-size corrections' to the effective potential are necessary. As to spherical particles, much work has been devoted to, among others, the interaction between a protein and a charged sphere [99], a planar surface and a charged sphere [100], as well as between two proteins characterised by surface patchiness [101]. Sometimes the protein charge pattern can be approximated by a simple dipole [102], leading to analytical expressions for the multipolar expansion of the protein-protein interaction. Very recently, the same problem has been studied by means of Monte Carlo computer simulations [103].

The present chapter focuses on the first steps towards the above goal, namely a systematic calculation of the screened electrostatic potential around a single spherical particle carrying an arbitrary number of positively or negatively charged sites distributed in a non-spherically symmetric discrete pattern inside the particle. The calculation is carried out within the LPB approximation, which allows for fully analytic results and is better justified than in the case of a single site carrying the total charge Ze of the particle, since the latter is divided into n well-separated sites carrying each only an elementary charge.

5.2 Debye-Hückel theory for a symmetric charge distribution

We shortly review the major steps in deriving the Debye-Hückel theory for a symmetric charge distribution of a spherical particle. A realistic situation represents a globular colloid dispersed in a fluid solvent and supplied with a symmetric negative charge distribution homogeneously smeared over its surface. Due to Gauss' law the total charge Q of the colloid can be assumed to be located into the center of the sphere. The negatively charged sphere expels the negative ions of the solvent ('coions') while the ions with positive charge ('counterions') feel attracted. In this way, a charge distribution is formed around the macromelecular particle, the so-called double layer, which partly screens the bare charge. The situation is visualized in fig. 5.1.

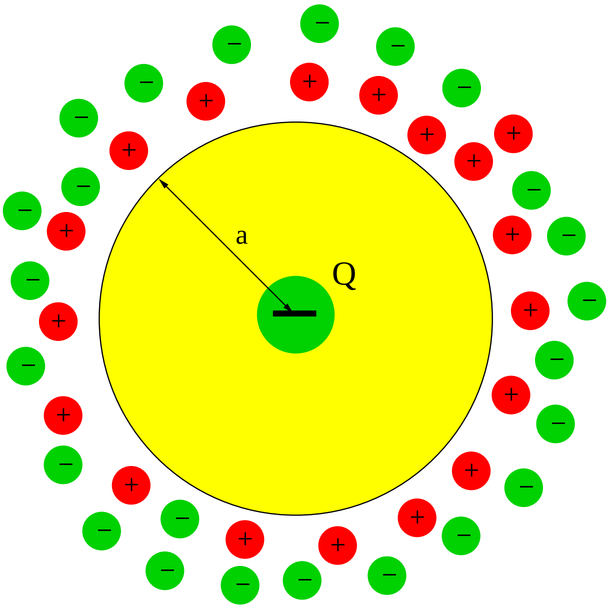

Figure 5.1: Plot of a colloid with a negative charge in its center. The monovalent counter- and coions form a double layer around the macromolecular entity screening the bare charge.

The Poisson equation is well-known from classical electrodynamics and relates the electrostatic potential $\Phi(\mathbf{r})$ to the charge distribution $\rho(\mathbf{r})$ spread throughout the space

$$\nabla^2\Phi(\mathbf{r}) = -4\pi\rho(\mathbf{r})/\epsilon. \tag{5.1}$$

The subsequent derivation is carried out in the framework of the primitive model. Therefore the dielectric constant ϵ accounts for the electrostatic solvent effects. Within Poisson-Boltzmann theory, the distribution of the counter- and coions is assumed to follow the Boltzmann equation

$$n_i(\mathbf{r}) = n_i^0 \exp(-z_i e\Phi(\mathbf{r})/k_{\mathrm{B}}T) \tag{5.2}$$

where n_i^0 is the number of ions of type i per unit volume in the bulk solution far from the colloid , k_B is the Boltzmann constant, T is the absolute temperature, z_i the valency of the adequate ion species and e the elementary charge. For the sake of simplification we assume $z_i = z_+ = -z_- = z$. Combining the Poisson equation (5.1) with the Boltzmann equation (5.2) leads to the Poisson-Boltzmann equation

$$\nabla^2\Phi(\mathbf{r}) = -4\pi\frac{1}{\epsilon}ze\sum_i n_i^0 \exp(-ze\Phi(\mathbf{r})/k_\mathrm{B}T). \tag{5.3}$$

It is a second-order nonlinear differential equation which cannot be solved analytically for a spherical geometry. However, by expanding the exponential to first order, an analytical solution can be obtained in the limits of this approximation. But before doing so, we write the Laplacian explicitly in spherical coordinates for eq. (5.3)

$$\frac{1}{r^2}\frac{\mathrm{d}}{\mathrm{d}r}\left(r^2\frac{\mathrm{d}\Phi(\mathbf{r})}{\mathrm{d}r}\right) = \frac{8\pi ze\sum_i n_i^0}{\epsilon}\sinh[ze\Phi(\mathbf{r})/k_\mathrm{B}T]. \tag{5.4}$$

Due to symmetry, all angle dependent derivatives of the Laplacian drop out. We linearize the equation (5.4) to cast it in an analytically tractable form

$$\frac{1}{r^2}\frac{\mathrm{d}}{\mathrm{d}r}\left(r^2\frac{\mathrm{d}\Phi(\mathbf{r})}{\mathrm{d}r}\right) = \kappa^2\Phi(\mathbf{r}) \tag{5.5}$$

with

$$\kappa = \left(\frac{8\pi z^2e^2\sum_i n_i^0}{\epsilon k_\mathrm{B}T}\right)^{1/2} \tag{5.6}$$

the so-called inverse screening length. Its inverse is often referred to as the spatial extent of the double layer. The approximation holds true as long as $ze\Phi(\mathbf{r}) \ll k_\mathrm{B}T$. The resulting differential equation can be solved analytically and yields the physically reasonable solution

$$\Phi(r) = \alpha\frac{\exp(-\kappa r)}{r}. \tag{5.7}$$

The yet unknown constant α is determined by imposing electroneutrality onto the system

$$-Q = \int_a^\infty \mathrm{d}r\, 4\pi r^2 ze\sum_i n_i(r) \tag{5.8}$$

furnishing

$$\alpha = \frac{Q}{\epsilon}\frac{\exp(\kappa a)}{1+\kappa a}. \tag{5.9}$$

Finally, the potential of a symmetric charge distribution reads in the framework of linearized Poisson-Boltzmann theory, or equivalently Debye-Hückel theory, as

$$\Phi(r) = \frac{Q}{\epsilon} \frac{\exp(\kappa a)}{1+\kappa a} \frac{\exp(-\kappa r)}{r}. \tag{5.10}$$

We point out once again that the last equation was derived under the condition of a symmetric charge distribution. It does not encompass asymmetric charge arrangements. That brings us to the next section.

5.3 Debye-Hückel theory for a asymmetric charge distribution

5.3.1 Posing the electrostatic problem

Consider a spherical particle (the "protein") of radius R carrying n discrete charged sites unevenly distributed over the volume of the particle, and surrounded by ν species of co- and counterions each of radius R_α and carrying charge $Z_\alpha e$ ($1 \leq \alpha \leq \nu$). For the sake of simplicity, all R_α will be assumed to be equal ($R_\alpha = \bar{R}$). Due to the superposition principle in a linearised theory, the total potential $\Phi(\mathbf{r})$ around the protein will be the sum of the potentials generated by each of the n charged sites. Hence it is sufficient to solve the electrostatic problem for a single site, say α, carrying charge $Z_\alpha e$. The situation is schematically represented in fig. 5.2.
The position $\mathbf{r}'$ of site α is characterised by the polar coordinates (r', θ', ϕ') with respect to a laboratory-fixed set of axes, while the potential $\Phi(\mathbf{r})$ is to be calculated at a point $\mathbf{r} = (r, \theta, \phi)$. We distinguish between three concentric regions of space around the protein. Region I ($r < R$) corresponds to the interior of the protein, of dielectric permittivity ϵ_1. Region II ($R < r < \sigma$) is the spherical shell of radius $\sigma = R + \bar{R}$ from which the centres of the microions are excluded due to their finite radius (they are of course also excluded from region I); a permittivity ϵ_2 is associated with that region, reflecting the fact that the implicit solvent's permittivity is expected to be significantly reduced in the immediate vicinity of the protein surface ($\epsilon_2 < \epsilon$, where ϵ is the bulk permittivity of the solvent). Finally region III ($\sigma < r$) contains all microions, and a permittivity $\epsilon_3 = \epsilon$ is associated with it. The electrostatic potential $\Phi(\mathbf{r})$ satisfies the following partial differential equations within the three regions:

1. Region I only contains the point charge $Z_\alpha e$ at $\mathbf{r}'$, so that $\Phi(\mathbf{r})$ satisfies Poisson's equation:

$$\nabla^2 \Phi^{\mathrm{I}}_\alpha(\mathbf{r}) = -\frac{4\pi}{\epsilon_1} Z_\alpha e \delta(\mathbf{r} - \mathbf{r}'). \tag{5.11}$$

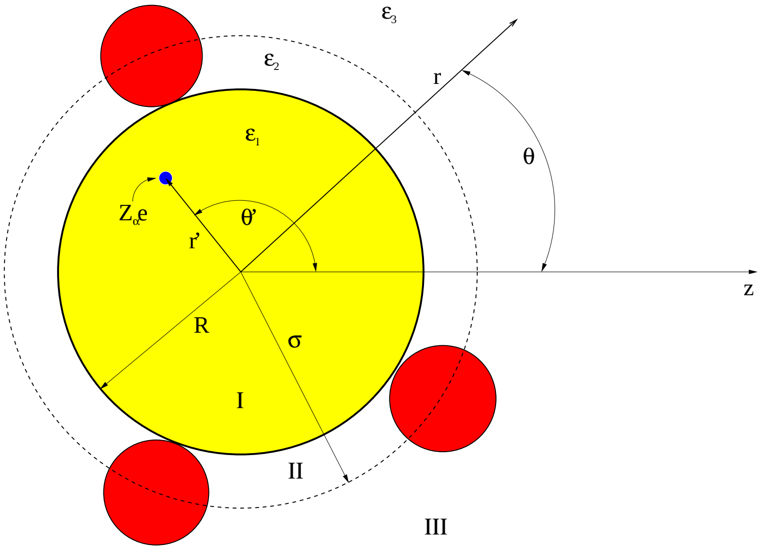

Figure 5.2: Two-dimensional plot of a model protein surrounded by the solvent and the counterions. The big sphere denotes the protein with a charge at r' and θ' inside. The smaller spheres are the counter- and co-ions.

2. Region II is free of charges, so that $\Phi(\mathbf{r})$ satisfies Laplace's equation in that region:

$$\nabla^2 \Phi_\alpha^{\mathrm{II}}(\mathbf{r}) = 0. \tag{5.12}$$

3. Region III contains the microions which, within mean-field theory, are assumed to follow Boltzmann distributions:

$$\begin{aligned} \rho_\beta(\mathbf{r}) &= \rho_\beta^{(0)} \exp\left(-\frac{Z_\beta e \Phi_\alpha(\mathbf{r})}{\epsilon_3 k_\mathrm{B} T}\right) \\ &\simeq \rho_\beta^{(0)} [1 - Z_\beta e \Phi_\alpha(\mathbf{r})/\epsilon_3 k_\mathrm{B} T] \end{aligned} \tag{5.13}$$

where $\rho_\beta^{(0)}$ is the bulk density of species β, and the linearisation is rigorously justified only provided $|Z_\beta e \Phi_\alpha(\mathbf{r})/\epsilon_3 k_\mathrm{B} T| < 1$ for $r > \sigma$.

The total charge density due to the microions being $\rho(\mathbf{r}) = \sum_\beta Z_\beta e \rho_\beta(\mathbf{r})$, global charge neutrality $(\sum_\beta Z_\beta e = 0)$ then implies that $\Phi_\alpha(\mathbf{r})$ satisfies the following Helmholtz (or LPB) equation in region III:

$$\nabla^2 \Phi_\alpha^{\mathrm{III}}(\mathbf{r}) - \kappa^2 \Phi_\alpha^{\mathrm{III}}(\mathbf{r}) = 0, \tag{5.14}$$

where $\kappa^2 = 4\pi e^2 \sum_\beta \rho_\beta^{(0)} Z_\beta^2 / \epsilon_3 k_\mathrm{B} T$ is the square of the inverse Debye screening length.

In spherical polar coordinates, the solution of Poisson's equation (5.11) is the superposition of the Coulomb potential due to charge $Z_\alpha e$ at $\mathbf{r}'$ and of the general solution of Laplace's equation for $(r < R)$, *i.e.*:

$$\Phi_\alpha^{\mathrm{I}}(\mathbf{r}) \equiv \Phi_\alpha^{\mathrm{I}}(r,\theta,\phi) = \sum_{l=0}^{\infty}\sum_{m=-l}^{l}\left(A_{lm}r^l + \frac{B_{lm}}{r^{l+1}} + \frac{Z_\alpha e}{\epsilon_1}\frac{4\pi}{2l+1}\frac{r_<^l}{r_>^{l+1}}Y_{lm}^*(\theta',\phi')\right)Y_{lm}(\theta,\phi). \tag{5.15}$$

where $r_>$ $(r_<)$ is the larger (smaller) of r and r', and the Y_{lm} are the usual spherical harmonics. The general solution of Laplace's equation (5.12) in region II reads:

$$\Phi_\alpha^{\mathrm{II}}(\mathbf{r}) = \sum_{l=0}^{\infty}\sum_{m=-l}^{l}\left(C_{lm}r^l + D_{lm}r^{-(l+1)}\right)Y_{lm}(\theta,\phi), \tag{5.16}$$

while the general solution of the Helmholtz equation (5.14) in region III may be expressed in terms of the modified spherical Bessel functions $I_{l+1/2}(z)$ and $K_{l+1/2}(z)$ of the third kind, as:

$$\Phi_\alpha^{\mathrm{III}}(\mathbf{r}) = \sum_{l=0}^{\infty}\sum_{m=-l}^{l}\frac{1}{\sqrt{r}}\left(E_{lm}I_{l+1/2}(\kappa r) + F_{lm}K_{l+1/2}(\kappa r)\right)Y_{lm}(\theta,\phi). \tag{5.17}$$

Note that $I_{l+1/2}(z) \to \infty$ and $K_{l+1/2}(z) \to 0$ as $z \to \infty$. Moreover, $K_{l+1/2}(z)/\sqrt{z} \sim e^{-z}/z$ as $z \to \infty$ [91], so that for large separations the electrostatic potential decreases towards zero in a Yukawa-like manner.

In eqs. (5.15)-(5.17) above, $\{A_{lm}\}$, $\{B_{lm}\}$, $\{C_{lm}\}$, $\{D_{lm}\}$, $\{E_{lm}\}$ and $\{F_{lm}\}$ are sets of coefficients, whose values must be determined by implementing the appropriate boundary conditions between regions I, II and III. These boundary conditions on the spherical surfaces are the following:

1. The potential must remain finite at the origin:

$$\Phi_\alpha^{\mathrm{I}}(\mathbf{r}=0) < \infty \Rightarrow B_{lm} = 0 \tag{5.18}$$

2. The potential must vanish at infinity:

$$\lim_{r\to\infty}\Phi_\alpha^{\mathrm{III}}(\mathbf{r}) = 0 \Rightarrow E_{lm} = 0 \tag{5.19}$$

3. In the absence of surface charges, the normal component of the displacement field and the tangential component of the electric field must be continuous at the interface separating regions I and II, *i.e.* at $r = R$; if $\hat{\mathbf{n}}$ denotes the unit normal to the sphere of radius R centered at the origin:

$$\hat{\mathbf{n}}\cdot(\mathbf{D}_{\mathrm{II}} - \mathbf{D}_{\mathrm{I}})\,|_{r=R} = 0 \tag{5.20}$$

$$\hat{\mathbf{n}}\times(\mathbf{E}_{\mathrm{II}} - \mathbf{E}_{\mathrm{I}})\,|_{r=R} = 0 \tag{5.21}$$

In terms of the potential $\Phi_\alpha(\mathbf{r})$ in the two regions, eq. (5.20) may be re-expressed as:

$$\epsilon_2 \left.\frac{\partial\Phi^{\mathrm{II}}_\alpha(\mathbf{r})}{\partial r}\right|_{r=R} = \epsilon_1 \left.\frac{\partial\Phi^{\mathrm{I}}_\alpha(\mathbf{r})}{\partial r}\right|_{r=R} \tag{5.22}$$

Similarly, eq. (5.21) may be re-expressed in terms of the partial derivatives of $\Phi^{\mathrm{I}}_\alpha(\mathbf{r})$ and $\Phi^{\mathrm{II}}_\alpha(\mathbf{r})$ with respect to the polar and azimuthal coordinates θ and ϕ. However these derivatives affect only the spherical harmonics and produce sets of linearly independent functions. Therefore, the θ and ϕ-derivatives lead to the same relations for the coefficients A_{lm}, C_{lm} and D_{lm}, and only the θ-derivatives will be required to express the boundary condition (5.21):

$$\left.\frac{\partial\Phi^{\mathrm{II}}_\alpha(\mathbf{r})}{\partial \theta}\right|_{r=R} = \left.\frac{\partial\Phi^{\mathrm{I}}_\alpha(\mathbf{r})}{\partial \theta}\right|_{r=R} \tag{5.23}$$

4) Similar boundary conditions hold at the interface between regions II and III, *i.e.*, at $r = \sigma$:

$$\epsilon_3 \left.\frac{\partial\Phi^{\mathrm{III}}_\alpha(\mathbf{r})}{\partial r}\right|_{r=\sigma} = \epsilon_2 \left.\frac{\partial\Phi^{\mathrm{II}}_\alpha(\mathbf{r})}{\partial r}\right|_{r=\sigma} \tag{5.24}$$

$$\left.\frac{\partial\Phi^{\mathrm{III}}_\alpha(\mathbf{r})}{\partial \theta}\right|_{r=\sigma} = \left.\frac{\partial\Phi^{\mathrm{II}}_\alpha(\mathbf{r})}{\partial \theta}\right|_{r=\sigma} \tag{5.25}$$

5.3.2 Solving the electrostatic problem

General solution

The explicit solution of the potential $\Phi_\alpha(\mathbf{r})$ is obtained by substituting the boundary conditions (5.18), (5.19), (5.22)-(5.25) in the general solution (5.15), (5.16) and (5.17) appropriate for the three regions I, II and III. We consider two cases: case A, where all three permittivities are assumed to be the same, *i.e.*, $\epsilon_1 = \epsilon_2 = \epsilon_3 = \epsilon$, and case B where $\epsilon_1 \neq \epsilon_2 \neq \epsilon_3 \neq \epsilon_1$. The implementation of the boundary conditions in the latter case is most easily achieved by the introduction of image charges associated with the co- and counterion charge distribution. The case of a single charge in the neighbourhood of a dielectric sphere was recently studied analytically [104]. The present work considers the situation of a many-body solution. It is easily verified that in the case $\epsilon_1 = \epsilon_2 \neq \epsilon_3$, the length scale R drops out of all expressions, and becomes hence irrelevant.

It proves convenient to introduce the following dimensionless ratios: $\delta = R/\sigma < 1$ and $\zeta = r'/R < 1$, the relative permittivities $\epsilon_{21} = \epsilon_2/\epsilon_1$, $\epsilon_{31} = \epsilon_3/\epsilon_1$ and $\epsilon_{32} = \epsilon_3/\epsilon_2$, as well as the following quantity:

$$\begin{aligned}(2l+1)\mathcal{B}_l(\epsilon_1,\epsilon_2,\epsilon_3,\delta) &= \frac{1}{\sqrt{\kappa\sigma}}K_{l+1/2}(\kappa\sigma)\left[(l+1)\,\delta^l\,(1-\epsilon_{21})+\delta^{-(l+1)}\left[l+(l+1)\,\epsilon_{21}\right]\right]\\ &+ \frac{1}{\sqrt{\kappa\sigma}}\left[lK_{l+1/2}(\kappa\sigma)-(\kappa\sigma)K_{l+3/2}(\kappa\sigma)\right]\times\\ &\times \left[(\epsilon_{32}-\epsilon_{31})\,\delta^l-\left(\epsilon_{32}+\epsilon_{31}\frac{l+1}{l}\right)\delta^{-(l+1)}\right]. \end{aligned} \tag{5.26}$$

Moreover, let $\mathbf{n}'$ and $\mathbf{n}$ be the unit vectors pointing to the source and the observation points, $\mathbf{r}'$ and $\mathbf{r}$, respectively. The full solution of the electrostatic problem is then given by:

Case I ($\epsilon_1=\epsilon_2=\epsilon_3=\epsilon$)

For $r\le\sigma$:

$$\Phi_\alpha(\mathbf{r})=\frac{Z_\alpha e}{\epsilon\sigma}\left[\frac{\sigma}{|\mathbf{r}-\mathbf{r}'|}-\frac{\kappa\sigma}{1+\kappa\sigma}+\sum_{l=1}^{\infty}\left(\frac{r'}{\sigma}\right)^l\left(\frac{r}{\sigma}\right)^l\frac{K_{l-1/2}(\kappa\sigma)}{K_{l+3/2}(\kappa\sigma)}P_l(\mathbf{n}'\cdot\mathbf{n})\right]. \tag{5.27}$$

For $r\ge\sigma$:

$$\Phi_\alpha(\mathbf{r})=\frac{Z_\alpha e}{\epsilon\sigma}\left[\frac{\exp\left[-\kappa(r-\sigma)\right]}{1+\kappa\sigma}\frac{\sigma}{r}+\sum_{l=1}^{\infty}(2l+1)\left(\frac{r'}{\sigma}\right)^l\frac{K_{l+1/2}(\kappa r)}{K_{l+3/2}(\kappa\sigma)}\frac{1}{\kappa\sigma}\sqrt{\frac{\sigma}{r}}P_l(\mathbf{n}'\cdot\mathbf{n})\right]. \tag{5.28}$$

Case II ($\epsilon_1\neq\epsilon_2\neq\epsilon_3\neq\epsilon_1$)

$$\Phi_\alpha(\mathbf{r})=\begin{cases}\frac{Z_\alpha e}{\epsilon_1}\frac{1}{|\mathbf{r}-\mathbf{r}'|}+A_0^{(\alpha)}+\sum\limits_{l=1}^{\infty}A_l^{(\alpha)}r^lP_l(\mathbf{n}'\cdot\mathbf{n}) & \text{for}\quad 0\le r\le R\\ C_0^{(\alpha)}+\frac{D_0^{(\alpha)}}{r}+\sum\limits_{l=1}^{\infty}\left(C_l^{(\alpha)}r^l+D_l^{(\alpha)}r^{-(l+1)}\right)P_l(\mathbf{n}'\cdot\mathbf{n}) & \text{for}\quad R\le r\le\sigma\\ F_0^{(\alpha)}\frac{\exp(-\kappa r)}{r}+\sum\limits_{l=1}^{\infty}F_l^{(\alpha)}\frac{K_{l+1/2}(\kappa r)}{\sqrt{\kappa r}}P_l(\mathbf{n}'\cdot\mathbf{n}) & \text{for}\quad \sigma\le r\end{cases} \tag{5.29}$$

where $P_l(\mathbf{n}'\cdot\mathbf{n})$ denotes the Legendre polynomial of order l and the coefficients $A_l^{(\alpha)}$, $C_l^{(\alpha)}$, $D_l^{(\alpha)}$ and $F_l^{(\alpha)}$ are given by:

$$A_0^{(\alpha)} = \frac{Z_\alpha e}{\epsilon_1 R}\left(\frac{1}{\epsilon_{21}}-1\right)+\frac{Z_\alpha e}{\epsilon_2\sigma}\left[\frac{1}{\epsilon_{32}(1+\kappa\sigma)}-1\right] \tag{5.30}$$

$$C_0^{(\alpha)} = \frac{Z_\alpha e}{\epsilon_2\sigma}\left[\frac{1}{\epsilon_{32}(1+\kappa\sigma)}-1\right] \tag{5.31}$$

$$D_0^{(\alpha)} = \frac{Z_\alpha e}{\epsilon_2} \tag{5.32}$$

$$F_0^{(\alpha)} = \frac{Z_\alpha e}{\epsilon_3}\frac{\exp(\kappa\sigma)}{1+\kappa\sigma}, \tag{5.33}$$

while for $l \neq 0$:

$$A_l^{(\alpha)} = \frac{Z_\alpha e}{\epsilon_1 R}\left(\frac{\zeta}{R}\right)^l \tag{5.34}$$
$$\times \left\{\frac{K_{l+1/2}(\kappa\sigma)[(l+1)\delta^l + l\delta^{-(l+1)}] + \epsilon_{32}[lK_{l+1/2}(\kappa\sigma)-(\kappa\sigma)K_{l+3/2}(\kappa\sigma)](\delta^l-\delta^{-(l+1)})}{l\sqrt{\kappa\sigma}\mathcal{B}_l}-1\right\}$$

$$C_l^{(\alpha)} = \frac{Z_\alpha e}{\epsilon_1 R}(2l+1)\sigma^{-l}\zeta^l\frac{(l+1)K_{l+1/2}(\kappa\sigma)+\epsilon_{32}[lK_{l+1/2}(\kappa\sigma)-(\kappa\sigma)K_{l+3/2}(\kappa\sigma)]}{l\sqrt{\kappa\sigma}\mathcal{B}_l} \tag{5.35}$$

$$D_l^{(\alpha)} = \frac{Z_\alpha e}{\epsilon_1 R}\sigma^{l+1}\zeta^l\frac{lK_{l+1/2}(\kappa\sigma)-\epsilon_{32}[lK_{l+1/2}(\kappa\sigma)-(\kappa\sigma)K_{l+3/2}(\kappa\sigma)]}{l\sqrt{\kappa\sigma}\mathcal{B}_l} \tag{5.36}$$

$$F_l^{(\alpha)} = \frac{Z_\alpha e}{\epsilon_1 R}(2l+1)\frac{\zeta^l}{l\mathcal{B}_l}. \tag{5.37}$$

Note that in deriving eqs. (5.27)-(5.37), summations over the azimuthal index m involving products of the spherical harmonics $Y^*_{lm}(\theta',\phi')Y_{lm}(\theta,\phi)$ have been carried out explicitly by making use of the addition theorem [48]

$$\sum_{m=-l}^{l} Y^*_{lm}(\theta',\phi')Y_{lm}(\theta,\phi) = \frac{2l+1}{4\pi}P_l(\mathbf{n}'\cdot\mathbf{n}). \tag{5.38}$$

We further remark that in the limit where the charge $Z_\alpha e$ is at the centre of the spherical protein ($r' = 0$), spherical symmetry is recovered, *i.e.*, all contributions for $l \geq 1$ vanish, and it is immediately seen from the above results that the electrostatic potential reduces, for $r > \sigma$, to the familiar DLVO form:

$$\Phi_0(r) = \frac{Ze}{\epsilon_3(1+\kappa\sigma)} \frac{e^{-\kappa(r-\sigma)}}{r}. \tag{5.39}$$

This holds in both cases A and B, i.e., irrespective of the presence or absence of dielectric discontinuities. The latter do, however, significantly affect the form of the potential $\Phi_\alpha(\mathbf{r})$ as soon as the charge $Z_\alpha e$ moves away from the centre.

The far field

The strong anisotropy of the electrostatic field persists all the way to the far field limit, $\kappa r \gg 1$. To demonstrate this, we now focus on the case in which all permittivities are equal, eq. (5.28). We consider a single embedded charge in the colloid and hence, without loss of generality, we can choose $\mathbf{n}'$ to lie on the z-axis, in which case $\mathbf{n}' \cdot \mathbf{n} = \cos\theta$. The asymptotic behaviour of the field for $\kappa r \gg 1$ can be now analyzed by making use of the general property of the spherical Bessel functions [91]:

$$\frac{K_{l+1/2}(z)}{\sqrt{z}} = \sqrt{\frac{\pi}{2}} \frac{\exp(-z)}{z} \left(1 + O(z^{-1})\right). \tag{5.40}$$

Keeping only the dominant term for $z \equiv \kappa r \gg 1$ in eq. (5.40) and substituting back in eq. (5.28), we obtain for the far-field the expression:

$$\Phi_\alpha(\mathbf{r}) \cong \frac{Z_\alpha e}{\epsilon} \frac{\exp(-\kappa r)}{r} \left[\frac{\exp(\kappa\sigma)}{1+\kappa\sigma} + \sqrt{\frac{\pi}{2}} \frac{1}{(\kappa\sigma)^{3/2}} \sum_{l=1}^{\infty} (2l+1)\eta^l \frac{P_l(\cos\theta)}{K_{l+3/2}(\kappa\sigma)} \right], \tag{5.41}$$

where $\eta = r'/\sigma$. As can be seen from eq. (5.41) above, the far-field maintains the form of a screened electrostatic (Yukawa) potential with the Debye screening length κ^{-1} setting the length scale. However, the 'charge renormalization factor' acquires an explicit angle-dependence that *persists* to arbitrarily large distances. This angle-dependence is expressed by the term in the square brackets in eq. (5.41), which we call $f(\theta)$.

In fig. 5.3 we show results for the function $f(\theta)$ for several values of η. A very strong anisotropy is apparent, with $f(\theta)$ varying by as much as a factor 5, depending on whether the far field is considered in the direction of the embedded charge ($\theta = 0$) or opposite to it ($\theta = \pi$). The same conclusions hold also for the case of unequal permittivities but here we limit ourselves to the simpler case where no dielectric discontinuity is present. Finally, we note that if one performs an angular average of the far-field expression, eq. (5.41), then all $l \neq 0$-terms vanish by virtue of the orthogonality of the Legendre polynomials and the isotropic limit is recovered. However, in a proper statistical-mechanical treatment of the problem, it is *not* the potential that

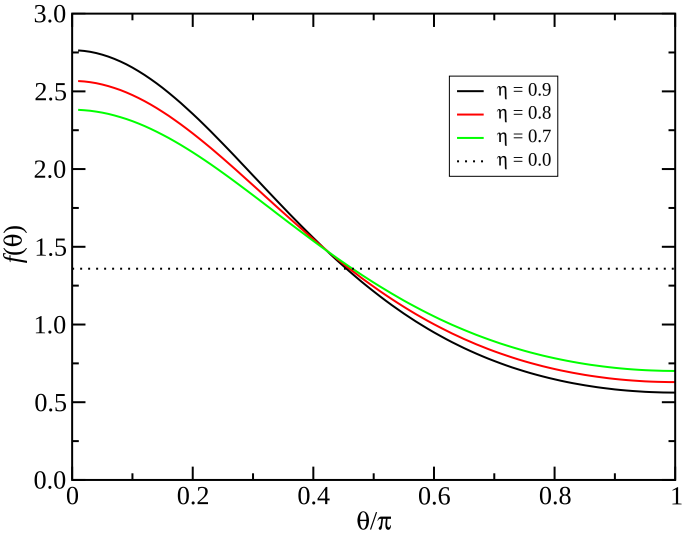

Figure 5.3: The function $f(\theta)$ [term in square brackets in eq. (5.41)] that expresses the angle-dependence of the far field due to a single charge embedded in a spherical colloid. Results for three different eccentricities of the embedded charge, $\eta = 0.9$, 0.8 and 0.7 are shown, together with the result valid for a charge in the centre of the colloid (dotted line, $\eta = 0$). The value of the screening parameter is chosen to be $\kappa\sigma = 1$.

must be angularly averaged but rather the Boltzmann factor. In other words, one can define a spherically symmetric effective potential $\Psi_\alpha(r)$ through the relation

$$\exp[-\beta\Psi_\alpha(r)] = \frac{1}{4\pi}\int \mathrm{d}\Omega\, \exp[-\beta\Phi_\alpha(\mathbf{r})], \tag{5.42}$$

where Ω denotes the solid angle in 3 spatial dimensions and $\beta = (k_B T)^{-1}$. As can be seen from eq. (5.41), in this case the $l \neq 0$-terms will contribute in the integration and the effective interaction potential $\Psi_\alpha(r)$ does not coincide with that from a single charge embedded at the centre of the colloidal particle.

5.3.3 Results for specific charge patterns

The results of section 5.3.2 will now be illustrated for some specific charge patterns. For each such pattern the total electrostatic potential $\Phi(\mathbf{r})$ outside the protein sphere is the sum of the individual contributions $\Phi_\alpha(\mathbf{r})$ from each of the n sites:

$$\Phi(\mathbf{r}) = \sum_{\alpha=1}^{n} \Phi_\alpha(\mathbf{r}) \tag{5.43}$$

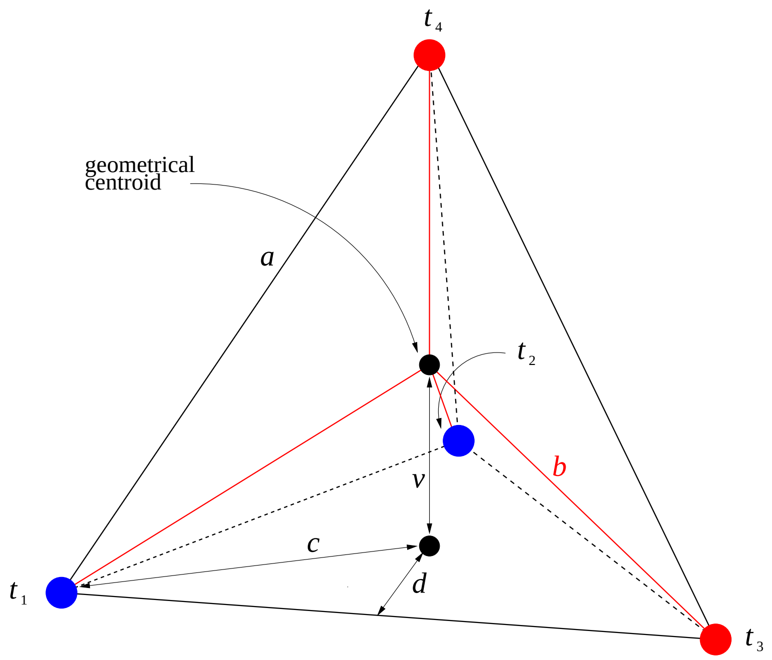

Figure 5.4: Three dimensional representation of a tetrahedron, depicting the quantities relevant to the physical problem at hand.

We present numerical implementations of eqs. (5.28) and (5.29) corresponding to case A with $\epsilon_1 = \epsilon_2 = \epsilon_3 = \epsilon = 80$ (dielectric permittivity of water under normal conditions), and to case B, where we chose $\epsilon_1 = \epsilon_2 = 2$ and $\epsilon_3 = \epsilon = 80$. The following three charge distributions will be considered: (1) a neutral tetrahedral distribution of two positive and two negative charges at 4 vertices of a regular tetrahedron, the geometric centroid of which coincides with the centre of the sphere; (2) a tetrahedral distribution with four identical charges at the four vertices; (3) a random distribution of 10 charges. The corresponding results are presented and discussed in the following three subsections.

Neutral tetrahedron

The tetrahedral charge distribution is schematically shown in fig. 5.4. For this charge arrangement, we construct a system of Cartesian coordinates as follows. The origin of the axes is positioned at the geometrical centre of the tetrahedron. The z-axis runs along the direction connecting the origin with the charge located at the vertex t_4, whereas the x-axis runs parallel to the direction of the segment c in fig. 5.4. The orientation of the y-axis is then determined by the right-hand rule. A three-dimensional representation of the tetrahedral arrangement within the

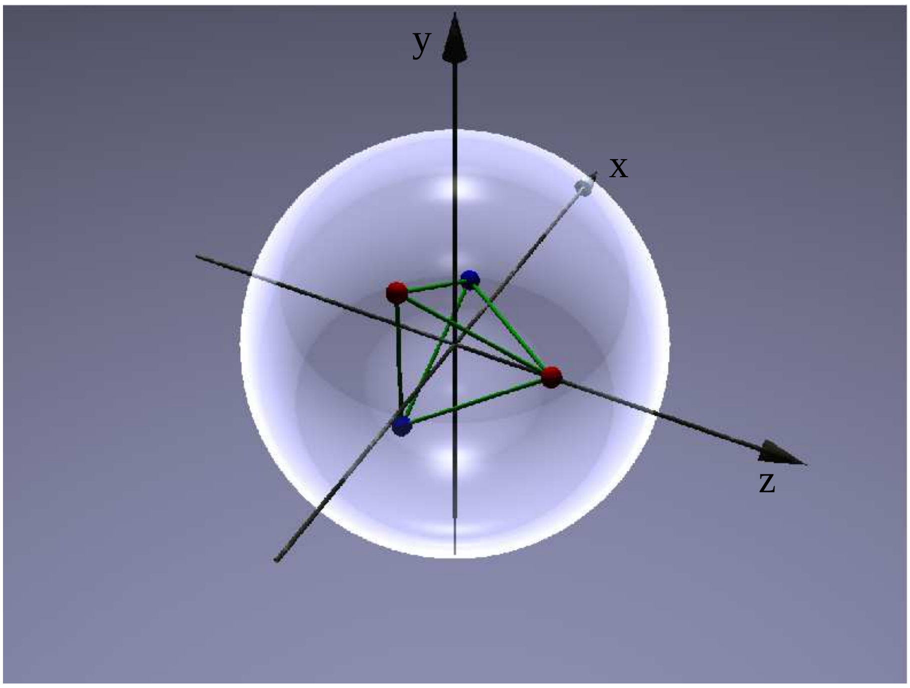

Figure 5.5: Three dimensional representation of a spherical protein carrying a tetrahedral charge distribution inside. The chosen orientation of the Cartesian axes is also shown.

confining sphere, showing also the Cartesian coordinates, is plotted in fig. 5.5. Let a be the edge size of the regular tetrahedron, b the distance from its centre to any of its vertices and v the distance from its centre to any of its faces. Moreover, let c be the distance from a vertex to the centre of any of the faces in which this vertex participates, and d the distance from the centre of a face to the opposite edge, as shown in fig. 5.4. All these distances can be expressed in terms of a, namely

$$b = \frac{a\sqrt{6}}{4}; \qquad v = \frac{a\sqrt{6}}{12}; \qquad c = \frac{a\sqrt{3}}{3}; \qquad d = \frac{a\sqrt{3}}{6}.$$

In what follows, we refer to b as the *eccentricity* of the charge distribution.
The positions of the four vertices, t_i, $i = 1, 2, 3, 4$, are given in Cartesian and spherical polar coordinates by the relations:

$$\begin{aligned}
t_1 &= & (c, 0, -v) & = (b, \arccos[-1/3], 0);\\
t_2 &= & (-d, -a/2, -v) & = (b, \arccos[-1/3], 4\pi/3);\\
t_3 &= & (-d, +a/2, -v) & = (b, \arccos[-1/3], 2\pi/3);\\
t_4 &= & (0, 0, b) & = (b, 0, 0).
\end{aligned}$$

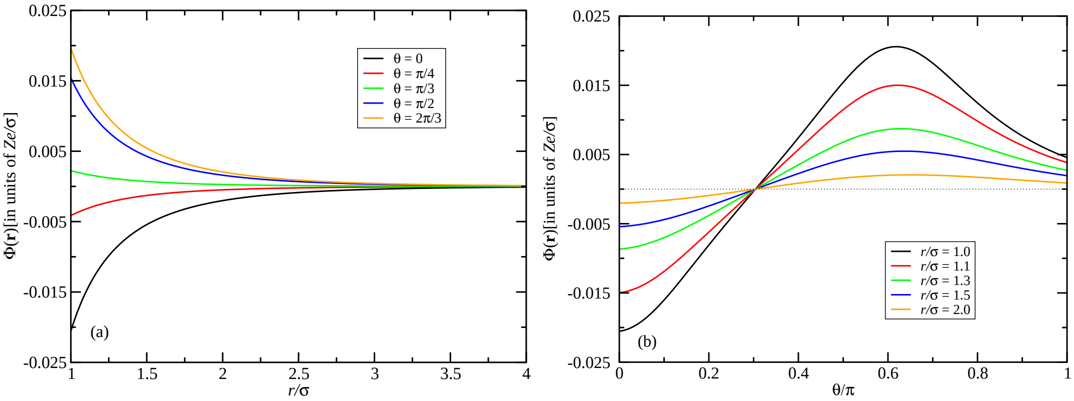

Figure 5.6: The screened electrostatic potential $\Phi(\mathbf{r})$ of a neutral tetrahedron in region III, at fixed azimuthal angle $\phi = 0$, and for $\epsilon_1 = \epsilon_2 \neq \epsilon_3$. The potential is shown as a function of (a) the distance r and (b) the polar angle θ. The eccentricity is $b = 0.5\sigma$ in both cases.

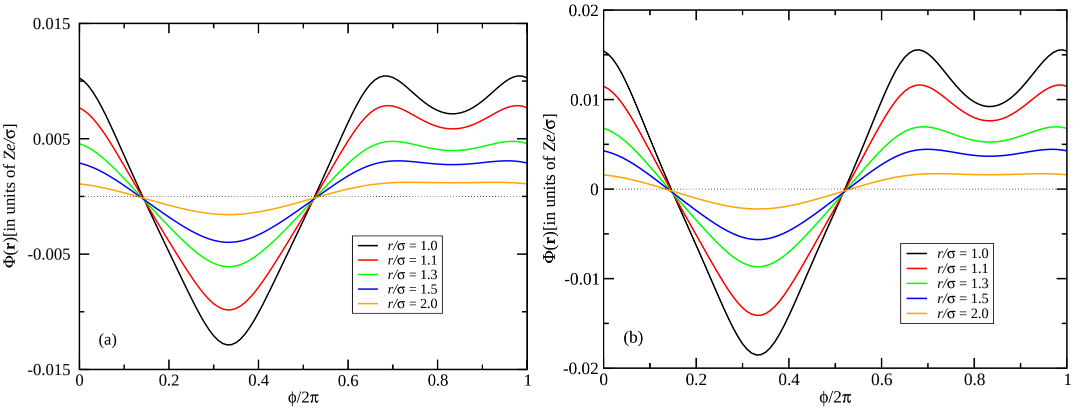

Figure 5.7: Same as fig. 5.6 but now as a function of the azimuthal angle ϕ at fixed polar angle $\theta = \pi/2$. (a) $\epsilon_1 = \epsilon_2 = \epsilon_3$; (b) $\epsilon_1 = \epsilon_2 \neq \epsilon_3$ in units of Ze/σ. The eccentricity is $b = 0.5\sigma$.

First we place at each of the vertices t_1 and t_2 a positive charge Ze and at the vertices t_3 and t_4 opposite charges, $-Ze$, and we calculate the screened electrostatic potential outside the sphere of radius R. The net charge is zero but all charges of the vertices have the same magnitude Z. Since we focus explicitly on the case $\epsilon_1 = \epsilon_2$, R drops out and only the length scales b and σ remain in the final expressions.

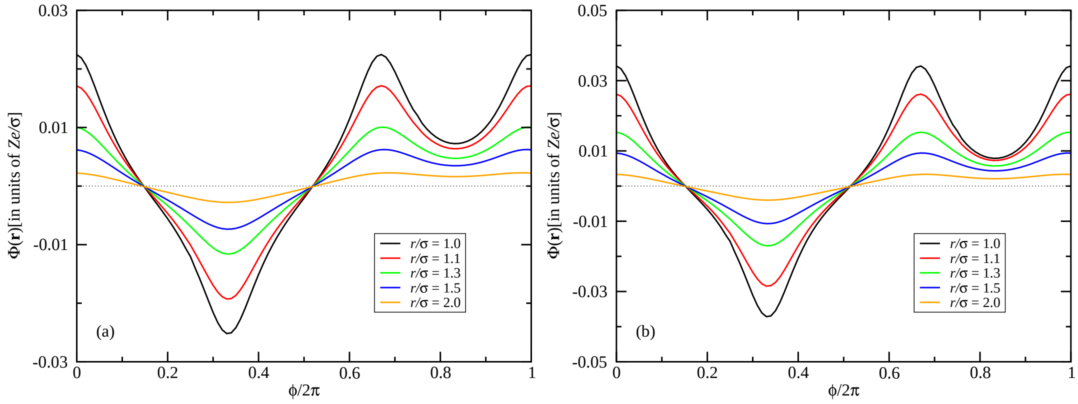

Figure 5.8: Same as fig. 5.7 but for eccentricity $b = 0.8\sigma$.

Explicit calculations were carried out for $b = 0.5\sigma$ and 0.8σ. The convergence of the series (5.28) and (5.29) in Legendre polynomials depends on the ratio b/σ, and is slower as this ratio increases. Results for the reduced potential $\Phi^*(\mathbf{r}) = \Phi(\mathbf{r})/(Ze/\sigma)$ are plotted as functions of θ, ϕ or r in figs. 5.6, 5.7 and 5.8. The anisotropy of the potential is seen to be strong, and to increase with the ratio b/σ, as expected. At the equatorial plane of the sphere ($\theta = \pi/2$, see fig. 5.7), a significant substructure develops, pointing to the possibility of preferentially 'trapping' test ions at particular positions and orientations of the asymmetrically charged sphere. Although the overall shape of the potential is not affected by going from case A ($\epsilon_1 = \epsilon_2 = \epsilon_3$) to case B ($\epsilon_1 = \epsilon_2 < \epsilon_3$), the amplitudes increase significantly in the latter case. A significant enhancement of the structure and amplitudes is also observed when the charges are positioned farther away from the centre, as can be readily seen by comparing figs. 5.8, pertinent to $b = 0.8\sigma$, with fig. 5.7 corresponding to the case $b = 0.5\sigma$.

Charged Tetrahedron

We consider next a tetrahedral distribution similar to the former one, except that all four charges are now of equal sign, thus adding up to a total charge $4Ze$. Results under conditions similar to the neutral case, are shown in figs. 5.9 and 5.10. Note once more the development of a significant angular substructure as well as the periodicity with an angle $\phi_0 = 2\pi/3$ for the case depicted in fig. 5.10. This arises from the symmetric arrangement of the three equal charges at the vertices of the equilateral triangle that forms one of the faces of the tetrahedron.

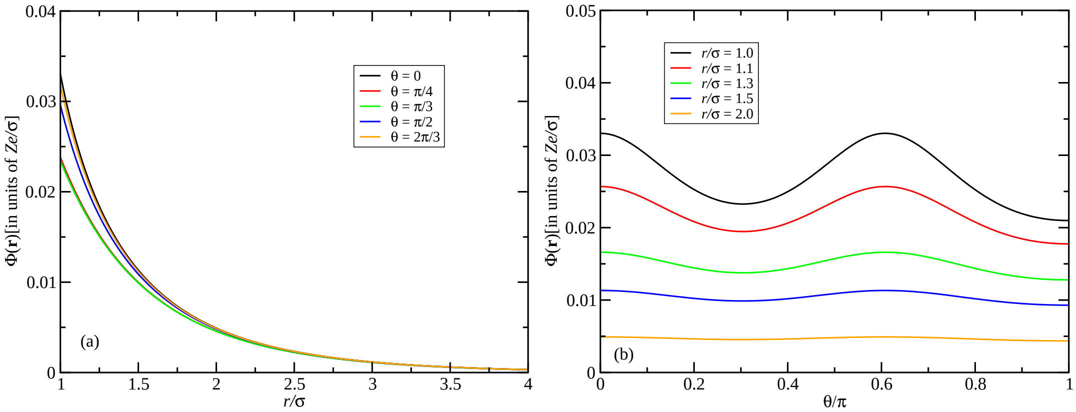

Figure 5.9: The screened electrostatic potential $\Phi(\mathbf{r})$ in region III, arising from a tetrahedron carrying four equal positive charges at its vertices, and for $\epsilon_1 = \epsilon_2 \neq \epsilon_3$. The azimuthal angle is fixed at $\phi = 0$. The potential is shown as a function of (a) the distance r and (b) the polar angle θ. The eccentricity is $b = 0.5\sigma$ in both cases.

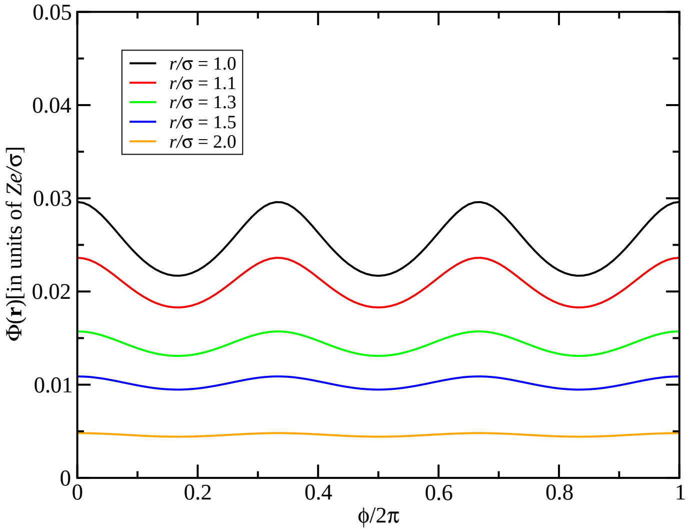

Figure 5.10: The screened electrostatic potential $\Phi(\mathbf{r})$ of a charged tetrahedron at $\theta = \pi/2$ and for $\epsilon_1 = \epsilon_2 \neq \epsilon_3$. The potential is shown in region III and as a function of the azimuthal angle ϕ. The eccentricity is $b = 0.5\sigma$.

Random charge distribution

Charge patterns in proteins are generally far from regular. For that reason we present in this section results for a random distribution of ten charges $\pm e$. The coordinates

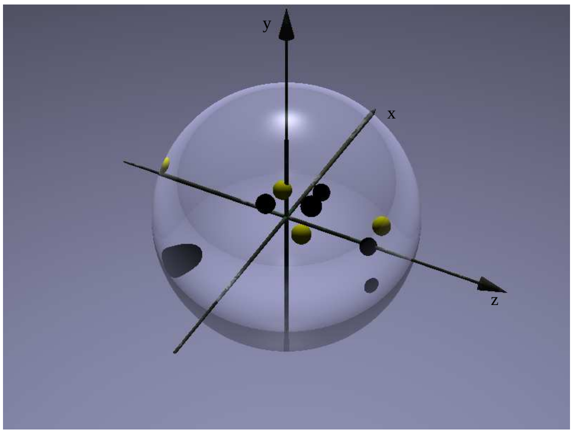

Figure 5.11: Three dimensional representation of a randomly generated charge distribution. The dark spheres denote positive charges and the light spheres negative ones.

and signs of those 10 charges were generated randomly inside the protein sphere. The polar coordinates of the 10 charges and their signs are listed in table 5.1, and the resulting charge distribution is pictured in the 3d representation of fig. 5.11. Representative plots of the resulting potential $\Phi(\mathbf{r})$ are shown in figs. 5.12 and 5.13. The variations of the potential are seen to differ considerably from those calculated for tetrahedral charge distributions.

	r'_α/σ	θ'_α	ϕ'_α	sign
1	0.458	0.941	1.83	+
2	0.126	2.87	1.37	+
3	0.490	0.381	6.19	−
4	0.139	1.12	5.05	−
5	0.864	2.26	5.14	+
6	0.763	0.355	3.39	+
7	0.709	2.92	2.08	−
8	0.183	1.67	1.62	−
9	0.500	0.0166	4.01	+
10	0.345	1.66	5.76	+

Table 5.1: Spherical polar coordinates of 10 charges whose positions and algebraic signs have been generated randomly.

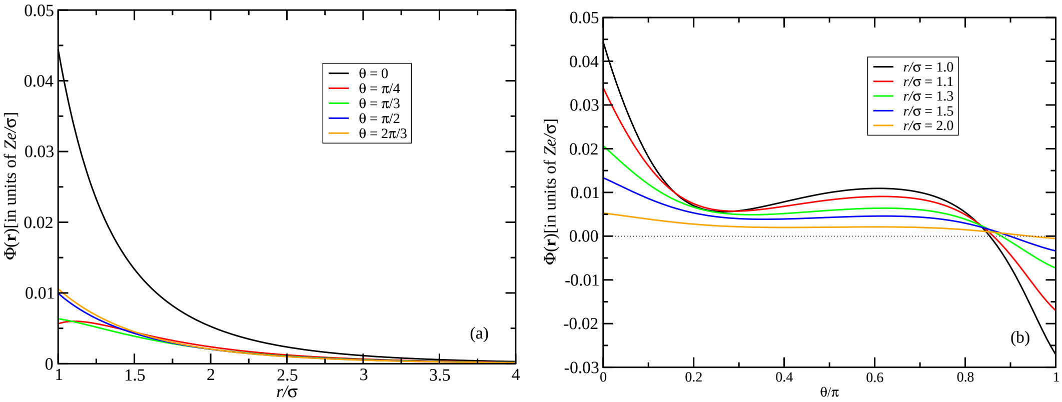

Figure 5.12: The screened electrostatic potential $\Phi(\mathbf{r})$ in region III, arising from the random charge distribution of Table 5.1 at $\phi = 0$, and for $\epsilon_1 = \epsilon_2 \neq \epsilon_3$. The potential is shown as a function of (a) the distance r and (b) the polar angle θ.

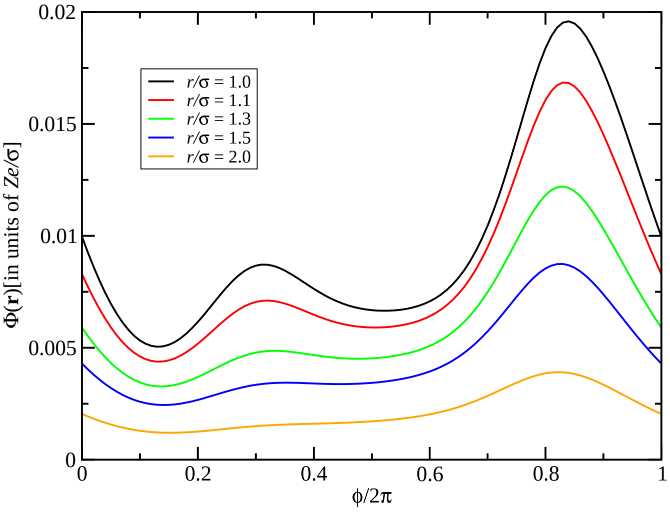

Figure 5.13: Same as fig. 5.12 but now at fixed polar angle $\theta = \pi/2$ and as a function of the azimuthal angle ϕ.

5.3.4 Conclusions

We have shown how the standard DLVO theory for the potential around a spherical particle carrying a spherically symmetric charge distribution can be generalised to arbitrary discrete charge patterns within LPB theory. The total potential generated by an arbitrary charge distribution in the presence of co- and counterions is simply the sum of the contributions from each charged site within the sphere. The present chapter provides a general expansion of the potential in spherical harmonics, which may be applied to any distribution of discrete charges within the particle. Since each charge in the pattern is screened individually the linearisation of Poisson-Boltzmann theory is better justified because the charge associated with each site is small (typically an elementary charge).

The potentials which we have calculated are strongly anisotropic and very sensitive to details of the protein charge pattern. Contrary to the case of a spherically symmetric charge distribution of the particle, the potential generated by a non-spherical, discrete distribution of sites depends on the relative dielectric permittivities of the particle, the spherical exclusion zone around the particle, and the bulk solvent. The anisotropy of the potential extends to the far field region, contrary to naïve expectations.

Chapter 6

Multivalent Counterion-condensation-induced Collapse of End-grafted Polyelectrolyte Chains

We address in this chapter to the situation of polyelectrolyte chains with charging fraction $f = 1$ and end-grafted to a planar surface in the presence of multivalent counterions. Our theory is based on a variational free energy that is written as a sum of electrostatic, polymer, and entropic contributions. Using Poisson-Boltzmann theory for the electrostatics and a mean-field term for the occurring bridging effect, we minimize the free energy with respect to the chain length and the number of counterions. The shrinking of the chain length with increasing electrostatic attraction of the monomeric units finally results into a collapsed state reminiscent of a first-order phase transition.

6.1 Introduction

Polyelectrolytes (PEs) are polymer chains with ionizable groups. Immersed in a polar solvent, these groups dissociate into the solvent leaving behind an equally, but oppositely charged backbone. PEs have recently attracted a great deal of interest [105–107] due to numerous biological and technological applications. Proteins and DNA are the most prominent representatives of PEs in the realm of biology. PEs play a key role in the context of hydrosolubility and solution thickening. Sulfonated polystyrene and polyacrylic acid, two other PEs, find application in diapers as superabsorbers. Attached to a surface, PEs prevent colloids from flocculation [108]. Furthermore, they can be used in surface modification for adhesion and lubrication problems.

In this chapter, we discuss the particular case of polyelectrolytes end-grafted to a planar solid surface. While charge stabilization prevents colloids from flocculation and aggregation, this methods turns out to be extremely sensitive to dissolved salts or other electrolytes. The addition of even small salt concentrations leads to a strong screening effect of the repulsive Coulombic interactions and a final break-down of the stabilization. Therefore, there is an increasing demand of investigating steric methods to stabilize colloidal dispersions against flocculation which are less sensitive to Debye screening. Steric stabilization is achieved by attaching a brush of flexible polymers to each particle enhancing their stability against flocculation [33, 109]. Therefore, there is a growing interest in the theoretical understanding of end-grafted polymers.

The end-grafting from solution onto an impenetrable substrate may be experimentally achieved by the use of block copolymers exploiting their amphilic character. The block copolymer is assembled by one block avoiding the solvent and therefore sticking to the wall whereas the other block is well-solvated and extends to the solvent. Alternately, polymer chains can be tethered onto a substrate by chemically active end groups which covalently bind to the surface.

PE chains end-grafted to a surface have been extensively studied by theory [33–41] as well as by experiment [42–45]. In contrast to neutral brushes, PE chains entail the electrostatic Coulomb force which is theoretically more difficult to handle. Pioneering work has been done by de Gennes [110] and Alexander [111], providing simple scaling laws for neutral end-grafted polymer chains. They show that the chains are strongly stretched at high grafting densities when immersed in a good solvent. The same holds true even for a poor solvent [112, 113]. These findings have been confirmed by low-angle neutron scattering [114–116]. This stretching behavior is mainly due to the short-ranged excluded volume effect.

The effect of counterion condensation has been predicted by Oosawa [117] in 1971 and numerically confirmed for rigid rods [118] as well as for flexible polymers in solution [119, 120]. The counterion condensation of highly charged PEs has been investigated in dilute and semidilute solution [121]. Simple scaling arguments are used to predict the chain collapse below a critical temperature. Based on the Alexander-de-Gennes approximation [111] and using mean-field Poisson-Boltzmann (PB) theory for the electrostatics, the weak- and strong-charging regimes have been investigated by scaling arguments [33]. For strongly charged brushes the chain length L is given by balancing the chain elasticity and the counterion osmotic pressure, satisfying $L \sim N$, where N is the degree of polymerization. Also using a step function profile and PB theory, the PE brush collapse has been studied by means of a free energy minimization [38]. The brush is seen to shrink with decreasing solvent quality. For weak charging the collapse occurs continuously below the θ-point whereas a first-order transition to the collapsed state has been found for a moderate charging fraction.

Mean-field PB theory neglects counterions fluctuations. A Debye-Hückel free energy [47] and a field theory [126] have been proposed in order to account for this fluctuation effect. Both theories find a first-order phase transition from the highly charged regime to the collapsed state.

In this chapter, we address to the collapse of end-grafted PE chains in the presence of multivalent counterions encouraged by a multivalent counter-ion-induced collapse of star-branched PEs observed in experiment and computer simulations [46]. Our theory is based on a variational free energy. The latter is written as a sum of electrostatic, polymer, and entropic contributions. The incorporation of the cumbersome long-ranged Coulomb interaction is tackled by a simple mean-field term. The multivalence of the counterions induces an attractive interaction between adjacent chains, the so-called *bridging* effect. We incorporate this additional effect by a simple mean-field term. The free energy is then minimized with respect to the different species of counterions and the chain length with the state of minimal energy being the physical stable one.

The rest of the chapter is organized as follows: in sec. 6.2 we review the PB theory of a charged interface in equilibrium with oppositely charged counterions (sec. 6.2.1) and then calculate the free energy of that system (sec. 6.2.2). Counterions exploring the exterior of the PE brush region can be assumed to discern the interior as a charged surface at position $z = L$ and therefore can be described in mean-field PB theory. Then we discuss the free energy of neutral polymers in sec. 6.3.1 and of polyelectrolytes in sec. 6.3.2. Sec. 6.4 contains a brief description of the simulated annealing algorithm used to minimize the free energy. In sec. 6.5, the results are presented and discussed. Finally, we draw our conclusions in sec. 6.6. As the free energy involves some delicate calculations, we present this technical part in Appendix D and in Appendix E.

6.2 Review

6.2.1 Poisson-Boltzmann theory around a single interface

We consider a single planar interface at position z in contact with a polar solvent as depicted in fig. 6.1. The surface has an uniform, fixed charge density

$$\sigma = \sigma_0 \delta(z). \tag{6.1}$$

We assume that the neutralizing monovalent counterions are arranged in the solvent according to the Boltzmann distribution. At this point, we specialize to the case of no added electrolyte and neglect the contribution of water ionization to the Debye screening. The Poisson-Boltzmann equation is the mean-field description of the

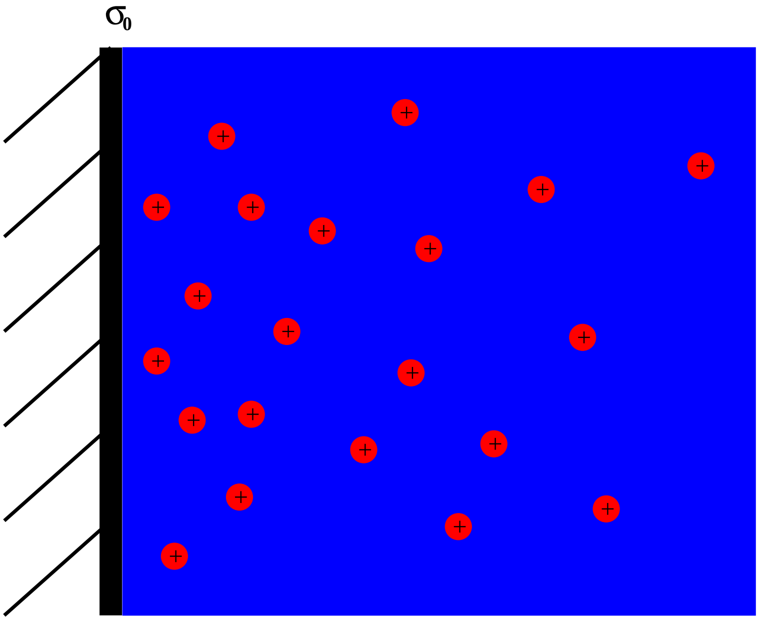

Figure 6.1: An interface with charge density σ_0 in equilibrium with oppositely charge counterions.

spatial counterion distribution. It is obtained by combining Poisson's equation of electrostatics

$$\mathrm{div}\mathbf{D}(\mathbf{r}) = 4\pi e\rho(\mathbf{r}) \tag{6.2}$$

where $\mathbf{D}(\mathbf{r})$ is the electric displacement, with the Boltzmann weighting for the counterion density, *i.e.*,

$$\rho(\mathbf{r}) = \rho_0 e^{-e\Psi(\mathbf{r})/T} \tag{6.3}$$

where ρ_0 is a constant determined by global charge neutrality

$$\int \mathrm{d}\mathbf{r}\, \rho_0 e^{-e\Psi/T} = \int \mathrm{d}\mathbf{r}\, \sigma \tag{6.4}$$

and $\Psi(\mathbf{r})$ is the potential at point $\mathbf{r}$. It is convenient to use dimensionless variables: $\psi \equiv e\Psi/T$ for the potential and $z \equiv x/\lambda$ for the length scale where x is the perpendicular distance from the surface into the solvent and λ is the Gouy-Chapman length which will be determined later. In terms of these variables, the Poisson-Boltzmann equation is

$$\frac{\mathrm{d}^2\psi}{\mathrm{d}z^2} = -4\pi l[\rho_0 e^{-\psi} - \sigma_0\delta(z)] \tag{6.5}$$

with the Bjerrum length l given by $l = e^2/(\epsilon T)$ where e is the electronic charge, ϵ is the dielectric constant of the solvent, and T is the temperature in energy units. This second-order nonlinear differential equation is solved by the counterion distribution

$$\rho(z) = [2\pi l(z+\lambda)^2]^{-1}. \tag{6.6}$$

Note that the counterions are effectively localized within a distance λ from the charged surface. Indeed, it is useful to consider the counterions as an ideal gas confined to a sheath of thickness of the order of the Gouy-Chapman length.
The Gouy-Chapman length can be easily derived by imposing the charge neutrality constraint, yielding

$$\lambda = \frac{1}{\sigma_0 \pi l}. \tag{6.7}$$

Using eq. (6.6), the electrostatic potential can be written as

$$\psi(z) = 2\ln[(z+\lambda)\sqrt{2\pi l \rho_0}]. \tag{6.8}$$

Note that the electric field which is given by $E(\mathbf{r}) = -\nabla\psi(\mathbf{r})$ decays to zero as $z \to \infty$.

6.2.2 Free energy around a single interface

In this section, we calculate the free energy of a system consisting of fixed charges and mobile counterions of number densities $\rho_{\mathrm{f}}(\mathbf{r})$ and $\rho(\mathbf{r})$, respectively. The derivation is quite general and does not restrict to a special spatial geometry. Assuming the counterions as a dilute, ideal gas, the free energy can be written as

$$\begin{aligned}\frac{F}{T} &= \int \mathrm{d}\mathbf{r}\, \rho(\mathbf{r})[\ln[\rho(\mathbf{r})v_0] - 1] + \frac{e^2}{2\epsilon}\int \mathrm{d}\mathbf{r}\,\mathrm{d}\mathbf{r}'\frac{\rho(\mathbf{r})\rho(\mathbf{r}')}{|\mathbf{r}-\mathbf{r}'|} \\ &\quad -\frac{e^2}{\epsilon}\int \mathrm{d}\mathbf{r}\,\mathrm{d}\mathbf{r}'\frac{\rho(\mathbf{r})\rho_{\mathrm{f}}(\mathbf{r}')}{|\mathbf{r}-\mathbf{r}'|} + \frac{e^2}{2\epsilon}\int \mathrm{d}\mathbf{r}\,\mathrm{d}\mathbf{r}'\frac{\rho_{\mathrm{f}}(\mathbf{r})\rho_{\mathrm{f}}(\mathbf{r}')}{|\mathbf{r}-\mathbf{r}'|},\end{aligned} \tag{6.9}$$

with v_0 being the volume per counterion. The first terms in eq. (6.9) accounts for the entropic countribution of the counterions, the second term is repulsion among the counterions, the third is the attraction between counterions and fixed charges, and the last terms is the repulsion of the fixed charges.
Charge conservation implies

$$\int \mathrm{d}\mathbf{r}\, \rho(\mathbf{r}) = -\int \mathrm{d}\mathbf{r}\, \rho_{\mathrm{f}}(\mathbf{r}). \tag{6.10}$$

For convenience, we define the potentials

$$\psi(\mathbf{r}) = \int \mathrm{d}\mathbf{r}'\, \frac{\rho(\mathbf{r}')}{|\mathbf{r}-\mathbf{r}'|}, \tag{6.11}$$

$$\psi_{\mathrm{f}}(\mathbf{r}) = \int \mathrm{d}\mathbf{r}'\, \frac{\rho_{\mathrm{f}}(\mathbf{r}')}{|\mathbf{r}-\mathbf{r}'|}. \tag{6.12}$$

Now, we minimze the grand potential G under the constraint of charge conservation with respect to $\rho(\mathbf{r})$

$$\frac{G}{T} = \frac{F}{T} - \mu \int \mathrm{d}\mathbf{r}\rho(\mathbf{r}), \tag{6.13}$$

yielding

$$\rho(\mathbf{r}) = \rho_0 \exp(-l\psi_\mathrm{t}) \tag{6.14}$$

where $\rho_0 \equiv e^\mu/v_0$ and $\psi_\mathrm{t} \equiv \psi + \psi_\mathrm{f}$. We substitute this result, eq. (6.14), back into the free energy, eq. (6.9), and we obtain[1]

$$\frac{F}{T} = \frac{1}{2} \int \mathrm{d}\mathbf{r}[\rho(\mathbf{r}) + \rho_\mathrm{f}(\mathbf{r})][\ln(\rho(\mathbf{r})v_0) - 1]. \tag{6.15}$$

Now, we are able to calculate the free energy of a charged interface in equilibrium with Boltzmann distributed counterions. The interface may have the charge density $\rho_\mathrm{f} = \sigma_0\delta(z)$ and the counterion distribution $\rho(\mathbf{r})$ is given by eq. (6.6) as derived in the former section. Plugging these two equations into the free energy expression, eq. (6.15), we obtain[2]

$$\frac{F}{T} = \frac{d^2\sigma_0}{2}\left[\ln\left[\frac{\pi}{2} l\sigma_0^2 v_0\right] - 2\right], \tag{6.16}$$

where d is a unit length. The last equation describes the free energy of a charged surface with surrounding counterions which obey a Boltzmann distribution. The free energy contains the electrostatic contributions among counterions themselves and the interaction between the surface and the counterions. The entropy of the counterions is assumed to be that of an ideal gas.

6.3 Theory

6.3.1 Neutral polymers

In order to elucidate the role of polymer elasticity, we briefly review the situation of neutral polymers end-grafted to a planar surface. The geometry is sketched in fig. 6.2. For simplicity, we consider monodisperse polymers of degree of polymerization N. They are end-grafted to a planar surface with a fixed mean grafting density d^{-2}. The solvent quality is described in terms of the Flory-Huggins free energy per unit volume [127]

$$\frac{Fa^3}{T} = \frac{1}{2}\tau\phi_\mathrm{m}^2 + \frac{1}{6}w\phi_\mathrm{m}^3 + \cdots \tag{6.17}$$

---

[1] For a detailed calculation see Appendix D.

[2] For a detailed calculation see Appendix E.

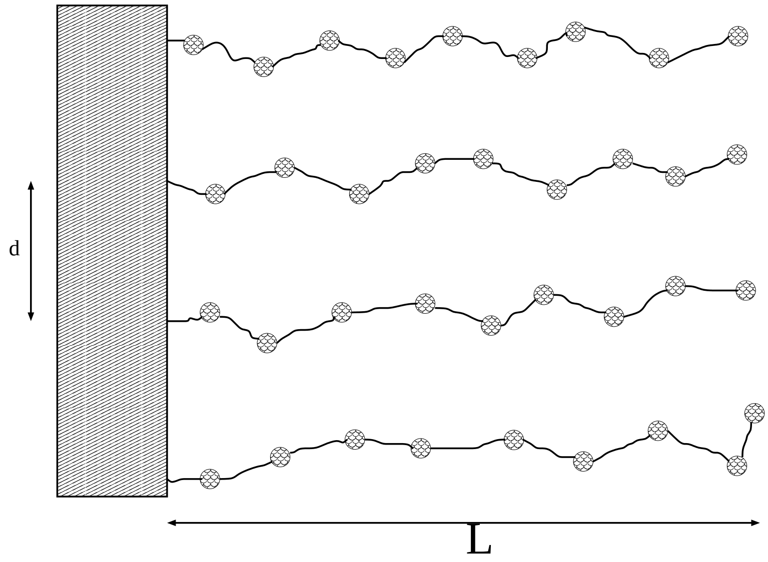

Figure 6.2: Neutral polymer chains end-grafted to a planar surface with grafting spacing d and brush thickness L

where a denotes the monomer dimension; τ is the dimensionless excluded-volume parameter, which is positive for good solvents and negative for poor solvents; ϕ_{m} is the polymer volume fraction; and w is the third virial coefficient which is typically positive and of order unity. It is related to the chain flexibility and may thus be varied by chemical modification of the polymer (change of side groups etc.). We explicitly emphasize the missing of the linear terms in the virial expansion in eq. (6.17). This term is related to the translational entropy of the chains which are end-grafted in our case.

The chains are extended in the form of a brush of thickness L. They are balanced by the excluded volume interaction trying to swell the chain and their elasticity tending to shrink their extent. If a Gaussian polymer has an end-to-end distance L, it stores the elastic energy $(1/2)kL$. The constant k assumes the role of a spring constant, and is given for a random walk chain by $k = T/(Na^2)$. Apparently, this contribution tries to decrease the thickness of the polymer brush. In mean-field theory, the osmotic pressure is given by [128]

$$P = \phi_{\mathrm{m}} \left(\frac{\mathrm{d}F}{\mathrm{d}\phi_{\mathrm{m}}} \right) - F = \frac{T}{a^3} \left(\frac{1}{2}\tau\phi_{\mathrm{m}}^2 + \frac{1}{3}w\phi_{\mathrm{m}}^3 + \cdots \right) \tag{6.18}$$

Provided that all of the grafted chains are stretched to an identical length L, static equilibrium is governed by

$$P = \frac{kL}{d^2} \tag{6.19}$$

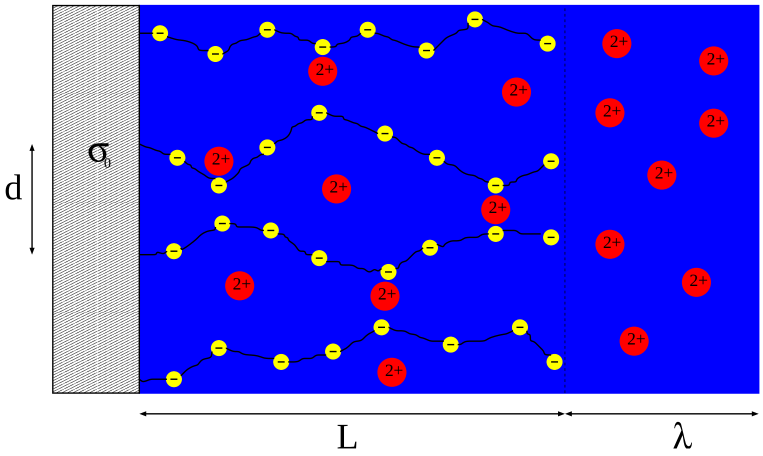

Figure 6.3: End-grafted PE chains in the presence of multivalent counterions with mean grafting spacing d and brush thickness L. The interface bears a surface charge σ_0 and the *free* counterions can move freely within the Gouy-Chapman layer of length λ.

If the monomers are uniformly distributed through the brush region, $\phi_{\rm m} = N_{\rm m}a^3/(Ld^2)$, several regimes can be distinguished depending on the magnitude of τ relative to w and the entropic elasticity.

6.3.2 Polyelectrolytes

Now, we turn to the case of PE chains end-grafted to a planar surface. When immersed in a polar solvent, *e.g.* water, the ionizable groups dissociate into the solvent, leaving behind a charged polymer in coexistence with its dissolved counterions. The counterions are partitioned into three different states: $N_{\rm t}$ *trapped* counterions: these are confined to move freely within the brush. $N_{\rm c}$ *condensed* counterions: they are recombined along the polymer chain. Finally, $N_{\rm f}$ *free* counterions: these are allowed to explore the whole region outside the brush. They are located in the region $L < z < L + \lambda$. The numbers of the three different counterion species cannot independently varied, in fact they obey the overall charge neutrality constraint

$$N_{\rm m} = zN_{\rm c} + zN_{\rm t} + zN_{\rm f} \tag{6.20}$$

with z denoting the valence of the counterions.
Each monomer unit is assumed to bear a ionizable group, therefore rendering the system to the highly charged regime. The monomer units are strictly monovalent while the counterions are allowed to be multivalent. The geometry is depicted in

fig. 6.3 for counterions of valency two. Recombined multivalent counterions can attract the oppositely charged monomer units of another chain. This occurrence is referred to as *bridging* effect.

The free energy of that system can be written in mean-field theory as:

$$\begin{aligned}\frac{Fa^3}{T} &= \frac{1}{2}\tau\phi_{\mathrm{m}}^2 + \frac{1}{6}w\phi_{\mathrm{m}}^3 + \frac{1}{2}\frac{L}{N_{\mathrm{m}}a^2}\frac{a^3}{Ld^2} + \phi_{\mathrm{t}}(\ln[\phi_{\mathrm{t}}] - 1) \\ &\quad + \left(\frac{\phi_{\mathrm{m}}}{z} - \phi_{\mathrm{c}}\right)\ln\left[\frac{\phi_{\mathrm{m}}}{z} - \frac{\phi_{\mathrm{c}}}{\phi_{\mathrm{m}}}\right] + \phi_{\mathrm{c}}\ln\left[\frac{\phi_{\mathrm{c}}}{\phi_{\mathrm{m}}}\right] - \epsilon\phi_{\mathrm{c}} \\ &\quad - g\phi_{\mathrm{c}}(\phi_{\mathrm{m}} - \phi_{\mathrm{c}}) + \frac{N_{\mathrm{f}}a^3}{2d^2}\left(\ln\left[\frac{\pi}{2}N_{\mathrm{f}}^2\frac{l}{d}\left(\frac{a}{d}\right)^3\right] - 2\right). \qquad (6.21)\end{aligned}$$

We recover the second and third virial terms as well as the elasticity term as the first three contribution to the free energy in eq. (6.21). These terms have been extensively discussed in sec. 6.3.1 in the context of neutral polymer chains.

The following three terms represent the entropic contributions stemming from the different species of counterions. Assuming that the *trapped* and *condensed* counterions are uniformly distributed over the brush region, their volume fraction can be written as $\phi_{\mathrm{t}} = N_{\mathrm{t}}a^3/(Ld^2)$ and $\phi_{\mathrm{c}} = N_{\mathrm{c}}a^3/(Ld^2)$, respectively. Since the *trapped* counterions can move freely within the brush, an ideal entropic contribution can be assigned to them. The terms $\phi_{\mathrm{c}}\ln[\phi_{\mathrm{c}}/\phi_{\mathrm{m}}]$ and $(\phi_{\mathrm{m}}/z - \phi_{\mathrm{c}})\ln[\phi_{\mathrm{m}}/z - \phi_{\mathrm{c}}/\phi_{\mathrm{m}}]$ are associated to the entropy of the counterions in the bound and unbound state, respectively.

The last three terms in eq. (6.21) account for the electrostatic interaction. The exact treatment of the Coulomb interaction between *condensed* counterions and monomers is an intricate challenge and analytically as well as numerically difficult to handle. Therefore, we address this task in a simple mean-field approach by the term $-\epsilon\phi_{\mathrm{c}}$ for accounting for an energy win by recombination. The value of ϵ governs the degree of the interaction between counterions and monomers. Large ϵ-values favor a stronger binding of the counterions to the monomers and lead to an earlier collapsed state due to the resulting lack of repulsion between the monomer units.

In the presence of multivalent counterions a bridging between the different chains may occur. This effect leads to a further decrease of the free energy and is analytically incorporated by the mean-field term $-g\phi_{\mathrm{c}}(\phi_{\mathrm{m}} - \phi_{\mathrm{c}})$ with g being a constant controlling the strength of the bridging. A strong bridging, *i.e.*, large g, should lead to an earlier collapse compared to lower g-values.

The last term in eq. (6.21) represents the electrostatic and entropic contribution of the *free* counterions. They discern the interior of the brush region as a charged surface with the dividing plane at $z = L$ and the charge density $\sigma = N_{\mathrm{f}}/d^2$. Using the results of sec. 6.2.1 and sec. 6.2.2, we get the specific form of the last term in eq. (6.21).

Using the introduced step-function profiles of the counterions confined to the brush and inserting the charge neutrality constraint, the free energy γ per unit area becomes

$$\begin{aligned}\frac{\gamma d^2}{T} &= \frac{1}{2}\tau N_{\mathrm{m}}^2\frac{a}{L}\left(\frac{a}{d}\right)^2+\frac{1}{6}wN_{\mathrm{m}}^3\left(\frac{a}{L}\right)^2\left(\frac{a}{d}\right)^4+\frac{1}{2N_{\mathrm{m}}}\left(\frac{L}{a}\right)^2\\ &+N_{\mathrm{t}}\left(\ln\left[N_{\mathrm{t}}\frac{a}{L}\left(\frac{a}{d}\right)^2\right]-1\right)+N_{\mathrm{c}}\ln\left[\frac{N_{\mathrm{c}}}{N_{\mathrm{m}}}\right]\\ &+\left(\frac{N_{\mathrm{m}}}{z}-N_{\mathrm{c}}\right)\ln\left[\frac{1}{z}-\frac{N_{\mathrm{c}}}{N_{\mathrm{m}}}\right]-\epsilon N_{\mathrm{c}}-gN_{\mathrm{c}}(1-N_{\mathrm{c}})\frac{a}{L}\left(\frac{a}{d}\right)^2\\ &+\frac{N_{\mathrm{m}}/z-N_{\mathrm{c}}-N_{\mathrm{t}}}{2}\left(\ln\left[\left(\frac{N_{\mathrm{m}}}{z}-N_{\mathrm{c}}-N_{\mathrm{t}}\right)^2\frac{\pi}{2}\left(\frac{a}{d}\right)^3\frac{l}{d}\right]-2\right).\end{aligned} \tag{6.22}$$

Minimizing eq. (6.22) with respect to the number of *trapped* counterions yields

$$N_{\mathrm{t}}=\left(\frac{N_{\mathrm{m}}}{z}-N_{\mathrm{c}}\right)\Big/\left(1+\sqrt{\frac{d}{l}\frac{2}{\pi}\frac{a}{d}\frac{a}{L}}\right). \tag{6.23}$$

This result can be plugged in turn in the free energy expression eq. (6.22) to eliminate N_{t}. The free energy has now been cast into a numerically amenable form depending only on two unkowns, namely the number of *condensed* counterions N_{c} and the chain length L.

6.4 Tools: simulated annealing

The task of multidimensional minimization poses an intricate and complex problem. If there is no initial guess close to the solution available, every conventional, downhill algorithm may get stuck in a local minimum and it is not capable of finding the global one. In this section, we review the basic principles of the simulated annealing (SA) algorithm. It avoids getting trapped in a local minimum by allowing once in a while uphill steps as well. Rather than presenting a detailed mathematical and numerical analysis, we exhibit its underlying principles by establishing a connection to statistical physics and refer the reader to the literature [122–124] for a more rigorous analysis.

Annealing is the physical process of heating up a solid until it melts, followed by cooling it down until it crystallizes into a state with a perfect lattice. Practice shows that the cooling must be done carefully in order not to get trapped in locally optimal structures with crystal imperfections.

The optimization problem can be understood as a many-body system which ground state can be found by the Metropolis algorithm [125] that can be used to provide an efficient simulation of a collection of atoms in equilibrium at a given temperature. In each step of this algorithm, an atom is given a random displacement and the resulting change in the free energy is computed. If the energy after the displacement is lower than the energy before, the displacement is accepted and the configuration with the displaced atom is the starting point for the next step. If the energy is higher after the displacement, the new configuration will be accepted with a certain probability dictated by the Boltzmann weight. By repeating these basic steps and slowly decreasing the temperature, the system gravitates towards its ground state of lowest energy.

In the realm of combinatorial optimization, the function to be minimized, usually called the cost function or objective function, corresponds to the energy. Using the cost function instead of the energy and defining a configuration by a set of its parameters, a population of configurations can be easily generated at a fixed temperature. In that case the temperature serves as a control parameter and is measured in units of the cost function. The minimization proceeds as follows: the system is 'melted' at a high effective temperature and then carefully 'cooled down'. At each temperature equilibrium is established by the procedure described above for the many-body system. The possibilty of uphill steps with a Boltzmann probability avoids the cost function to get stuck in a local minimum. Note that the lower the temperature of the sytem is, the less likely is any significant uphill step. Finally, the function reaches its ground state. Precondition for finding the global minimum is a sufficiently slow cooling process. It can be shown that the algorithm finds asymptotically the global minimum. Due to finite computional time, there is no guarantee that the algorithm finally succeeds, but a sufficently slow cooling has been proven to furnish good results.

We have used the SA algorithm to minimize the free energy, eq. (6.22). To ensure that we did not miss the global minimum due to the asymptotic constraint, we have plotted the free energy for a couple of test parameters. No more than two minima could be observed in these cases. Since these both minima are of almost identical magnitude close to the phase transition, we computed the free energy for both in that region and directly compared them to each other.

6.5 Results and Discussion

In this section, we discuss the numerical results of the theory presented in the previous paragraph. We consider PE chains with a fixed charging fraction $f = 1$. They contain $N = 1000$ monomeric units each and they are end-grafted to a planar surface with chain concentration d^{-2} with $d = 10a$ and a being the typical monomer extent. The charge of the PE chains is neutralized by counterions which we allow to have a fixed valency z. We assume a θ-solvent, *i.e.*, the short-ranged excluded-

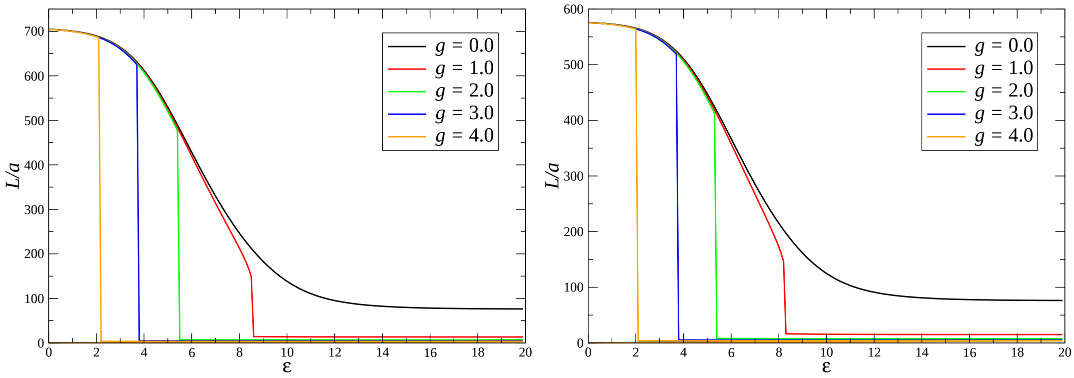

Figure 6.4: Scaled chain length L/a versus the parameter ϵ (a) for valency $z = 2$ and (b) for valency $z = 3$ for different values of the bridging parameter g.

volume repulsion between the monomers is not taken into account.

We minimize the free energy, eq. (6.22), with respect to the chain length L and the number of *condensed* counterions. The state with the lowest free energy affirms the physically stable one with an associated chain length and counterion distribution. The results for counterion valencies $z = 2$ and $z = 3$ are shown in fig. 6.4. We show the scaled chain length L/a in dependence of parameter ϵ controlling the strength of the recombination between monomers and counterions. These results have been calculated for different g-values controlling the bridging effect. The bridging effect does not occur for $g = 0$ and becomes stronger for increasing g.

In the absence of *condensed* counterions, *i.e.*, $\epsilon = 0$, the chains are stretched into a rod-like shape. In that case all monomers are charged and adjacent monomeric units try to keep away from each other as far as possible resulting in an extended state. But only for the monovalent situation the chain length is given by its maximum value $L \simeq Na$. For multivalent counterions, the osmotic pressure of the counterions is lower and therefore the chains are less stretched. We provide a simple scaling argument for that situation. The elasticity force is given by

$$f_{\text{el}} = \frac{L}{N_{\text{m}} a^2 d^2}, \tag{6.24}$$

and the osmotic pressure is

$$f_{\text{os}} = \frac{N_{\text{m}}}{z d^2 L}. \tag{6.25}$$

The balance of these both terms leads to:

$$L \simeq \frac{Na}{\sqrt{z}}, \tag{6.26}$$

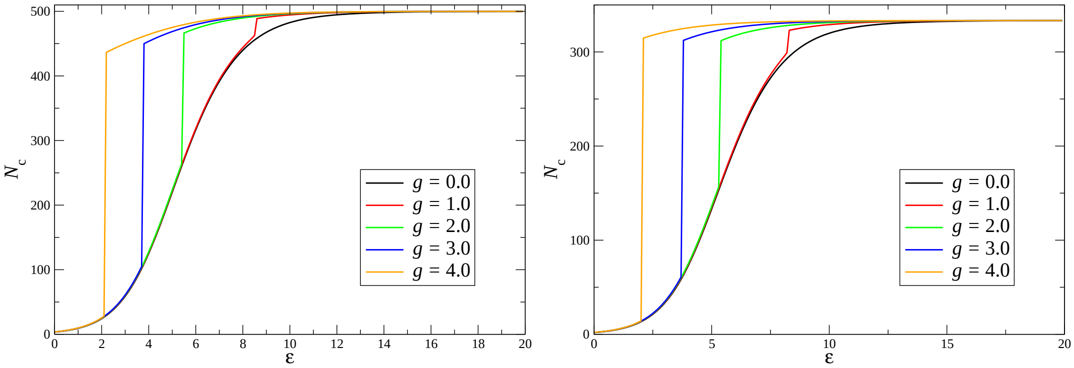

Figure 6.5: Number of *condensed* counterions versus the parameter ϵ (a) for valency $z = 2$ and (b) for valency $z = 3$ for different values of the bridging parameter g.

resulting in a shrinking of the chain length with increasing counterion valency. Indeed, the scaling approximation for the chain length furnishes $L/a \simeq 707$ and $L/a \simeq 577$ for $z = 2$ and $z = 3$, respectively. These results are in perfect agreement the numerical findings in fig. 6.4(a) and fig. 6.4(b). The conformation of the PE chains is mainly determined by the competition between the counterion entropy and the electrostatic interaction between counterions and monomers. The system tries to preserve local charge neutrality at the expense of mixing of counterions which is increased if they can explore larger volumes. A stronger interaction between the opposite charges, *i.e.*, a larger ϵ value, leads to a larger number of *condensed* counterions as can be seen in fig. 6.5. The number of *condensed* counterions is plotted versus ϵ for two different valencies. For non-zero g-values the curve jumps discontinuously at exactly the same ϵ as it does in the plot of the chain length. Finally, the number of *condensed* counterions saturates at N_m/z.

By increasing the number of *condensed* counterions the chains becomes less charged and their length does shrink. Just for the case without bridging, *i.e.*, $g = 0$, the brush collapses in a continuous way. Without bridging the brush does not totally collapse, but rather levels off to a finite, non-zero value. This value is dictated by the balance of the third virial term,

$$\frac{F_\mathrm{3rd}}{T} = \frac{1}{6} w \frac{N_\mathrm{m}^3}{d^6 L^2}, \tag{6.27}$$

and the elasticity energy of the chain,

$$\frac{F_\mathrm{el}}{T} = \frac{L^2}{N_\mathrm{m} a^2 d^2}, \tag{6.28}$$

resulting in:

$$L = w^4 N_\mathrm{m} \frac{\sqrt{a}}{d}. \tag{6.29}$$

Substituting the corresponding numerical values into the latter equation amounts to a chain length of order 10^2 which is in agreement with the values in fig. 6.4.
In the presence of bridging, the collapse occurs discontinuously reminiscent of a first-order phase transition. The brush length jumps abruptly to a lower value. Recombined multivalent counterions attract oppositely charged monomers enhancing the shrinking of the chain length and finally leading to the collapse. We observe an earlier brush collapse for increasing g, *i.e.*, a stronger attraction between adjacent chains. But the collapse appears nearly independent of the investigated valencies.

6.6 Conclusions

We have shown in this chapter that for highly charged PE chains end-grafted to a planar surface a chain collapse is observed in the presence of multivalent counterions. The phase transition is first-order and in agreement with previous results [47].

Chapter 7

Summary and Outlook

The thesis at hand contributes to elucidate the role of magnetic and electrostatic interactions in the realm of soft condensed matter. We specifically focused on colloidal particles and polyelectrolyte chains. Thereby, we direct our attention to three different systems: superparamagnetic particles in two dimensions, colloids with asymmetric charge distributions, and polyelectrolyte chains end-grafted to a planar wall.
The main focus of this works lies on the investigation of mixtures of two-dimensional superparamagnetic particles exposed to an external magnetic field directed perpendicular to the plane [130]. We have analyzed the fluid structure by liquid integral equation theory and Brownian dynamics simulation. We observed a clustering of the smaller particles in the voids of the bigger ones. We were able to characterize the pattern formation by tools from integral geometry, namely the Euler characteristic. The clusters turned out to be rather diffuse and possess a percolating sponge-like topology with a significant number of holes. The clustering behavior can be traced back to the non-additivity of the system, *i.e.*, the cross-interaction is less repulsive than the sum of the two direct interactions. We could confront our theoretical findings to direct space experimental data and we found a perfect agreement with them [49].
The one-component system of the superparamagnetic particles has been studied under the influence of a tilted magnetic field [131]. The particles align themselves into the direction of the in-plane component of the magnetic field. The local ordering of the particles becomes more inhomogeneous with increasing tilt angle. As a direct extension of this work, the two-component case with tilted magnetic field and the consequential pattern formation might be investigated. More generally for this project, it would be interesting to study the viscosity and the propagation of light in partially clustered structures in order to extract their specific material properties. It is further tempting to shock-freeze the clustered structure and use it as a bicontinuous device of controlled, random nano-porosity.
The second part of this work deals with colloidal particles of asymmetric charge

pattern [132]. We were able to extend the classic DLVO theory strictly holding for a spherosymmetric charge distribution to the case of a single colloid with an elementary charge displaced from its center. Solving linearized Poisson-Boltzmann theory, we have derived analytical expressions for the electrostatic potential around the particle. Special charge arrangements have been considered explicitly as representative examples. Due to the superposition principles, our results may be applied to any distribution of discrete charges within the colloid. The next step will be to calculate the microion-averaged, effective pair potential between two proteins carrying identical charge patterns, as a function of the distance between the two proteins, and the mutual orientation of their charge patterns. The fulfillment of this task will be the subject of future work.

The third project revolves around polyelectrolyte chains end-grafted to a planar surface in the presence of multivalent counterions [133]. We explicitly address to the attraction of neighboring chains mediated by the rebinding of the multivalent counterions while treating the electrostatics in mean-field Poisson-Boltzmann theory. The free energy consisting of polymeric, entropic and electrostatic contributions is minimized in order to characterize the state of the system. We find a transition from the extended to the collapsed state reminiscent of a first-order phase transition. Our results are expected to be relevant to ongoing experimental studies of PE brushes. In the future, we will extend our framework to the case of two opposing surfaces with end-grafted PE chains. An approach similar to this work is applicable and may lead to further insight of colloid stabilization by end-grafted PE chains.

Appendix A

Two-dimensional Fourier Transform

In this appendix, we derive an algorithm, following Caillol *et al.* [84], to calculate the Fourier transform (FT) in two dimensions accurately and fast. In contrast to the three-dimensional case, the occurring integrals cannot easily be reduced to a simple one-dimensional integral. We define the 2d FT in polar coordinates for a radial symmetric function $f(r)$ as follows

$$\tilde{f}(k) = \int_0^{2\pi} \mathrm{d}\varphi \int_0^{\infty} \mathrm{d}r \; r \exp[ikr\cos(\varphi)] f(r). \tag{A.1}$$

Taking into account the following definition of the Bessel transform of zero order:

$$J_0(z) = \frac{1}{2\pi} \int_0^{2\pi} \mathrm{d}\phi \exp(\pm iz\cos\varphi), \tag{A.2}$$

we can rewrite equation (A.1) by using the relation (A.2):

$$\tilde{f}(k) = 2\pi \int_0^{\infty} \mathrm{d}r \; r J_0(kr) f(r), \tag{A.3}$$

which is called the Hankel transform. The task of calculating the 2d Fourier transform now has formally reduced to the calculation of the Hankel transform.
First, we introduce new variables which are connected to the old ones by the following relation

$$\begin{aligned} r &= \exp(\rho) \\ k &= \exp(K) \end{aligned} \tag{A.4}$$

Passing over to the new coordinates, equation (A.3) reads as:

$$\tilde{f}(\exp[K]) = \exp(-K)\int_{-\infty}^{\infty} \mathrm{d}\rho\ \exp(\rho) f(\exp[\rho]) \exp(\rho + K) J_0(\exp[\rho + K]). \quad (A.5)$$

The right-hand side of equation (A.5) can be rewritten as a convolution type integral:

$$\tilde{f}(\exp[K]) = 4\pi \exp(-K)\mathrm{Re}\int_{0}^{\infty} \mathrm{d}t\ \Phi(t) M(t) \exp(iKt), \quad (A.6)$$

where

$$\Phi(t) = \frac{1}{2\pi}\int_{-\infty}^{\infty} \mathrm{d}\rho \exp(\rho) f(\exp[\rho]) \exp(it\rho) \quad (A.7)$$

and

$$M(t) = \frac{1}{2\pi}\int_{-\infty}^{\infty} \mathrm{d}\rho \exp(\rho) J_0(\exp[\rho]) \exp(-it\rho). \quad (A.8)$$

The latter integral $M(t)$ can be calculated analytically, see [84].

We split the integral $\Phi(t)$ into two parts and shift the boundaries of the second part:

$$\begin{aligned} \Phi(t) &= \frac{1}{2\pi}\int_{-\infty}^{\rho_m} \mathrm{d}\rho \exp(\rho) f(\exp[\rho]) \exp(it\rho) + \\ & \frac{1}{2\pi}\exp(it\rho_m)\int_{0}^{\infty} \mathrm{d}\rho \exp(\rho + \rho_m) f(\exp[\rho + \rho_m]) \exp(it\rho). \end{aligned} \quad (A.9)$$

For $|\rho_m|$ sufficiently large ($\rho_m < 0$), we can assume that f is constant for $\rho < \rho_m$. Therefore, the first integral on the the right-hand side of equation (A.9), $\Phi_1(t)$, can be calculated analytically, yielding:

$$\Phi_1(t) = \frac{1}{2\pi}\exp(\rho_m) f(\exp[\rho_m]) \frac{\exp(it\rho_m)}{1 + it}. \quad (A.10)$$

The second integral on the right-hand side of equation (A.9) can be calculated by a fast Fourier transform (FFT) technique.

In conclusion, we could rewrite the Hankel transform eq. (A.1) by means of a simple coordinate transform (eq. (A.4)) into a convolution type integral eq. (A.5). Transforming to Fourier space, it decomposes into the product of two integrals, eqs. (A.7) and (A.8). One of them can be calculated analytically, whereas the other can be calculated by a FFT. Going back to real space by the inverse FFT yields the desired Hankel transform.

Appendix B

The Euler Characteristic for Quadratic Lattices

Consider a quadratic lattice (lattice constant l) for which some elementary plaquettes (pixels, i.e., squares of edge length l) are occupied and some are empty. The resulting spatial pattern is represented by the configuration $[u] = \{u(i,j)\}$ of the main text, with $u(i,j) = 0\,(1)$ denoting a full (empty) site. In principle, the resulting Euler characteristic of the pattern can be calculated by employing the property of sub-additivity, eq. (3.14). There are three types of closed sets participating in the pattern, coded as follows: 2-cells (square plaquettes), 1-cells (edges of length l) and 0-cells (points). Due to the discrete geometry, 2-cells can only intersect on 1- or 0-cells and 1-cells only on 0-cells. We denote the Euler characteristic of a D-cell, $D \leq d = 2$, (D is the topological dimension of the cell) as X_D. Evidently, it holds $X_D = 1$ for all three cells described above.

In calculating $X[u]$ via eq. (3.14), track of all intersections must be kept. In order to simplify the calculation and completely avoid intersections, we now introduce the *open cell* $\breve{C}$ of any closed cell C, defined as $\breve{C} = C \setminus \partial C$, where ∂C is the boundary of C. For example, every closed square can be figured as the union of the disjoint collection of its interior, its open edges and its point vertices, whereby there is no distinction between open and close points. The Euler characteristic of an *open* convex cell $\breve{X}_D$ is given by [78]:

$$\breve{X}_D = (-1)^D. \tag{B.1}$$

Thus, $\breve{X}_2 = 1$ for an open square, $\breve{X}_1 = -1$ for an open edge and $\breve{X}_0 = 1$ for the vertices. Since a closed square is the disjoint union of the open interior, the four open edges and the four vertices, the above considerations together with eq. (3.14) consistently give

$$X_2 = 1 + 4 \times (-1) + 4 \times 1 = 1, \tag{B.2}$$

whereas for a closed line segment (edge), which can be seen as the union of the open segment and the two endpoints, we again consistently obtain

$$X_1 = -1 + 2 \times 1 = 1. \tag{B.3}$$

Evidently, the computational advantage of working with open sets on a discrete lattice is that all intersections vanish and the sub-additivity of eq. (3.14) becomes strict additivity. Let, therefore, $N_D[u]$ be the number of open D-cells present in any configuration $[u]$. Eqs. (3.14) and (B.1) above imply that the Euler characteristic $X[u]$ is a linear superposition:

$$X[u] = \sum_{D=0}^{2} \breve{X}_D N_D[u] = N_0[u] - N_1[u] + N_2[u]. \tag{B.4}$$

It is straightforward to show that the quantities $N_D[u]$ are given by the expressions:

$$N_2[u] = \sum_i \sum_j [1 - u(i,j)]\,; \tag{B.5}$$

$$N_1[u] = \sum_i \sum_j \{2 - u(i,j)\,[u(i+1,j) + u(i,j+1)]\}\,; \tag{B.6}$$

$$N_0[u] = \sum_i \sum_j [1 - u(i,j)u(i+1,j)u(i,j+1)u(i+1,j+1)]\,. \tag{B.7}$$

Eq. (3.16) of the main text immediately follows from eqs. (B.4)-(B.7) above.

Appendix C

Hankel Transform of the Expansion Coefficient

In the this appendix, we show a strict derivation of the interconnection between the coefficients of the series expansion in real and reciprocal space. Performing the Fourier transform of the direct correlation function $c(r)$ leads to the following lines:

$$\begin{aligned}\tilde{c}(\mathbf{k}) &= \int \mathrm{d}^2 r\, c(\mathbf{r}) \exp(i\mathbf{kr}) \qquad \text{(C.1)}\\ &= \int \mathrm{d}^2 r \sum_m c_m(r) \exp(-im\theta_R) \exp[ikr\cos(\theta_R - \theta_K)]\\ &= \sum_m \int_0^\infty \mathrm{d}r r c_m(r) \int_0^{2\pi} \mathrm{d}\theta_R \exp[-im(\theta_R-\theta_K)] \exp[ikr\cos(\theta_R-\theta_K)] \exp(-im\theta_K)\\ &= \sum_m \exp(-im\theta_K) \int_0^\infty \mathrm{d}r\, r c_m(r) \underbrace{\int_0^{2\pi} \mathrm{d}\theta_R \exp[-im(\theta_R-\theta_K)] \exp[ikr\cos(\theta_R-\theta_K)]}_{I(kr)}.\end{aligned}$$

We put $x \equiv \theta_R - \theta_K$, and substitute

$$I(kr) = \int_{-\theta_K}^{2\pi-\theta_K} \mathrm{d}x \exp(-imx) \exp(ikr\cos x), \tag{C.2}$$

using the 2π-periodicity of the integrand, we write

$$I(kr) = \int_0^{2\pi} \mathrm{d}x \exp(-imx) \exp(ikr\cos x) \equiv 2\pi i^m J_m(kr). \tag{C.3}$$

Then, we can write the Fourier transform as:

$$\begin{aligned}\tilde{c}(k) &= \sum_m \exp(-im\theta_K) 2\pi i^m \int_0^\infty \mathrm{d}r r c_m(r) J_m(kr) \\ &= \sum_m \tilde{c}_m(k) \exp(-im\theta_K)\end{aligned} \tag{C.4}$$

with

$$\tilde{c}_m(k) = 2\pi i^m \int_0^\infty \mathrm{d}r r c_m(r) J_m(kr). \tag{C.5}$$

Similarly, we obtain

$$c_m(r) = (2\pi)^{-1} i^m \int_0^\infty \mathrm{d}k k \tilde{c}_m(k) J_m(kr). \tag{C.6}$$

The coefficients in real and reciprocal space can be transformed into each other by a simple Hankel transform of $0th$-order.

Appendix D

Free Energy Calculation - Part I

Here, we explicitly show the calculation for substituting eq. (6.14) into eq. (6.9):

$$\begin{aligned}
\frac{F}{T} &= \int \mathrm{d}\mathbf{r}\rho(\mathbf{r})[\ln[\rho(\mathbf{r})v_0]-1]+\frac{1}{2}\rho(\mathbf{r})l\psi(\mathbf{r})+\rho(\mathbf{r})l\psi_{\mathrm{f}}(\mathbf{r})-\frac{1}{2}\rho_{\mathrm{f}}(\mathbf{r})l\psi_{\mathrm{f}}(\mathbf{r}) \\
&= \int \mathrm{d}\mathbf{r}\rho(\mathbf{r})[\ln[\rho(\mathbf{r})v_0]-1]+\frac{1}{2}\rho(\mathbf{r})l[\psi(\mathbf{r})+\psi_{\mathrm{f}}(\mathbf{r})]-\frac{1}{2}\rho_{\mathrm{f}}(\mathbf{r})l\psi(\mathbf{r}) \\
&\quad -\frac{1}{2}\rho_{\mathrm{f}}(\mathbf{r})l\psi_{\mathrm{f}}(\mathbf{r}) \\
&= \int \mathrm{d}\mathbf{r}\rho(\mathbf{r})[\ln[\rho(\mathbf{r})v_0]-1]-\frac{1}{2}\rho(\mathbf{r})\ln\left[\frac{\rho(\mathbf{r})}{\rho_0}\right]-\frac{1}{2}\rho_{\mathrm{f}}(\mathbf{r})l[\psi(\mathbf{r})+\psi_{\mathrm{f}}(\mathbf{r})] \\
&= \int \mathrm{d}\mathbf{r}\rho(\mathbf{r})[\ln[\rho(\mathbf{r})v_0]-1]-\frac{1}{2}\rho(\mathbf{r})\ln[\rho(\mathbf{r})v_0]+\frac{1}{2}\rho(\mathbf{r})\ln[e^{\mu}] \\
&\quad +\frac{1}{2}\rho_{\mathrm{f}}(\mathbf{r})\ln\left[\frac{\rho(\mathbf{r})}{\rho_0}\right] \\
&= \int \mathrm{d}\mathbf{r}\rho(\mathbf{r})[\ln[\rho(\mathbf{r})v_0]-1]-\frac{1}{2}\rho(\mathbf{r})\ln[\rho(\mathbf{r})v_0]+\frac{1}{2}\rho(\mathbf{r})\mu \\
&\quad +\frac{1}{2}\rho_{\mathrm{f}}(\mathbf{r})\ln\left[\frac{\rho(\mathbf{r})}{\rho_0}\right]-\frac{1}{2}\rho_{\mathrm{f}}(\mathbf{r})\mu \\
&= \frac{1}{2}\int \mathrm{d}\mathbf{r}[\rho(\mathbf{r})+\rho_{\mathrm{f}}(\mathbf{r})][\ln[\rho(\mathbf{r})v_0]-1],
\end{aligned}$$

where we have used in the last two lines the constraint of charge neutrality, eq. (6.10).

Appendix E

Free Energy Calculation - Part II

We explicitly plug the charge density $\rho_\mathrm{f} = \sigma_0\delta(z)$ of the interface and the counterion distribution eq. (6.6) into the free energy, eq. (6.15):

$$\frac{F}{T} = \underbrace{\frac{1}{2}\int \mathrm{d}\mathbf{r}\rho_\mathrm{f}(\mathbf{r})[\ln[\rho(\mathbf{r})v_0]-1]}_{F_\mathrm{I}/T} + \underbrace{\frac{1}{2}\int \mathrm{d}\mathbf{r}\rho(\mathbf{r})[\ln[\rho(\mathbf{r})v_0]-1]}_{F_\mathrm{II}/T}$$

We calculate the first part

$$\begin{aligned}
\frac{F_\mathrm{I}}{T} &= \frac{1}{2}\int \mathrm{d}\mathbf{r}\rho_\mathrm{f}(\mathbf{r})[\ln[\rho(\mathbf{r})v_0]-1] \\
&= \frac{d^2}{2}\int_0^\infty \mathrm{d}z\sigma_0\delta(z)\left[\ln\left[\frac{1}{2\pi l}\frac{v_0}{(z+\lambda)^2}\right]-1\right] \\
&= \frac{d^2}{2}\left(\frac{\sigma_0}{2}\ln\left[\frac{1}{2\pi l}\frac{v_0}{\lambda^2}\right]-\frac{\sigma_0}{2}\right) \\
&= \frac{d^2}{4}\left(\ln\left[\frac{\pi}{2}lv_0\sigma_0^2\right]-1\right)
\end{aligned}$$

The calculation of the second part is straightforward, too

$$\begin{aligned}
\frac{F_\mathrm{II}}{T} &= \frac{1}{2}\int \mathrm{d}\mathbf{r}\rho(\mathbf{r})[\ln[\rho(\mathbf{r})v_0]-1] \\
&= \frac{d^2}{2}\int_0^\infty \mathrm{d}z\frac{1}{2\pi l}\frac{1}{(z+\lambda)^2}\left[\ln\left[\frac{1}{2\pi l}\frac{v_0}{(z+\lambda)^2}\right]-1\right]
\end{aligned}$$

We substitute $x = \sqrt{2\pi l}(z + \lambda)$

$$\begin{aligned}
\frac{F_{\mathrm{II}}}{T} &= \frac{d^2}{2} \int_{\sqrt{2\pi l}\lambda}^{\infty} \mathrm{d}z \frac{1}{\sqrt{2\pi l}} \frac{1}{x^2} \left[\ln \left[\frac{1}{x^2} \right] - 1 \right] \\
&= \frac{d^2}{2} \frac{1}{\sqrt{2\pi l}} \left[\frac{3}{x} - \frac{\ln \left[\frac{v_0}{x^2} \right]}{x} \right]_{\sqrt{2\pi l}\lambda}^{\infty} \\
&= -\frac{d^2}{2} \frac{1}{\sqrt{2\pi l}} \left[\frac{3}{\sqrt{2\pi l}\lambda} - \frac{\ln \left[\frac{v_0}{2\pi l \lambda^2} \right]}{\sqrt{2\pi l}\lambda} \right] \\
&= \frac{d^2}{2} \frac{1}{\sqrt{2\pi l}} \left[\pi l \sigma_0 \ln \left[\frac{\pi}{2} l \sigma_0^2 \right] - 3\pi l \sigma_0 \right] \\
&= \frac{d^2}{4} \sigma_0 \left[\ln \left[\frac{\pi}{2} l \sigma_0^2 \right] - 3 \right]
\end{aligned}$$

We obtain the total free energy by combining the both parts

$$\frac{F}{T} = \frac{F_{\mathrm{I}}}{T} + \frac{F_{\mathrm{II}}}{T} = \frac{d^2}{4} \sigma_0 \left[2 \ln \left[\frac{\pi}{2} l \sigma_0^2 v_0 \right] - 4 \right]$$

$$\Rightarrow \frac{F}{T} = \frac{d^2}{2} \sigma_0 \left[\ln \left[\frac{\pi}{2} l \sigma_0^2 v_0 \right] - 2 \right].$$

Bibliography

[1] R. J. Hunter, *Foundations of Colloid Science*, vol.I, (Clarendon Press, Oxford, 1986).

[2] S. A. Safran and N. A. Clark, eds., *Physics of Complex and Supermolecular Fluids* (Wiley Interscience, New York, 1987).

[3] W. B. Russel, D. A. Saville, and W. R. Schowalter, *Colloidal Dispersions* (Cambridge University Press, Cambridge, 1989).

[4] C. N. Likos, in *Jülich, Session B, Computional Condensed Matter Physics*(37th IFF Spring School, 2006), ed. by S. Blügel, G. Gompper, E. Koch, H. Müller-Krumbhaar, R. Spatschek, R. G. Winkler.

[5] W. G. McMillan and J. E. Mayer, J. Chem. Phys **13**, 276 (1945).

[6] J. G. Kirkwood and F. P. Buff, J. Chem. Phys. **19**, 774 (1951).

[7] W. van Megen and I. Snook, Adv. Coll. Interface Sci. **21**, 119 (1984).

[8] C. N. Likos, Phys. Rep. **348**, 267 (2001).

[9] V. A. Bloomfield, Curr. Opin. Struct. Biol. **6**, 334 (1996).

[10] W. M. Gelbart, R. F. Bruinsma, P. A. Pincus, and V. A. Parsegian, Phys. Today **53**, 38 (2000).

[11] H.-A. Kurzhals and H. Reuter, Chemie Ingenieur Technik **45**, 491 (1973).

[12] P. F. W. Strengers, editor, Blut, Spektrum, 1996.

[13] J. Dhont, *An Introduction to Dynamics of Colloids* (Elsevier, Amsterdam, 1996).

[14] K. Zahn, A. Wille, G. Maret, S. Sengupta, P. Nielaba, Phys. Rev. Lett. **90**, 155506 (2003).

[15] A. Wille, F. Valmont, K. Zahn, G. Maret, Europhys. Lett. **57**, 219 (2002).

[16] H. H. Grünberg, P. Keim, K. Zahn, and G. Maret, Phys. Rev. Lett. **93**, 255703 (2004).

[17] K. Zahn, R. Lenke, G. Maret, Phys. Rev. Lett. **82**, 2721 (1999).

[18] C. Eisenmann, P. Keim, U. Gasser, and G. Maret, J. Phys.: Condens. Matter **16**, S4095 (2004).

[19] C. Eisenmann, U. Gasser, P. Keim, and G. Maret, Phys. Rev. Lett. **93**, 105702 (2004).

[20] K. Zahn, G. Maret, Phys. Rev. Lett. **85**, 3656 (2000).

[21] K. Zahn, J. M. MendezAlcaraz, and G. Maret, Phys. Rev. Lett. **79**, 175 (1997).

[22] B. Rinn, K. Zahn, P. Maass, and G. Maret, Europhys. Lett. **23**, 673 (1993).

[23] H. König, R. Hund, K. Zahn, and G. Maret, Eur. Phys. J. E **18**, 287 (2005).

[24] T. Kondo, K. Tsumuraya, M. S. Watanabe, J. Chem. Phys. **93**, 5182 (1990).

[25] H. Miyagawa, Y. Hiwatari, B. Bernu, J. P. Hansen, J. Chem. Phys. **88**, 3879 (1988).

[26] M. Kollmann, R. Hund, B. Rinn, G. Nagele, K. Zahn, H. Konig, G. Maret, R. Klein, J. K. G. Dhont, Europhys. Lett. **58**, 919 (2002).

[27] V. A. Froltsov, C. N. Likos, H. Löwen, C. Eisenmann, U. Gasser, P. Keim, and G. Maret, Phys. Rev. E **71**, 031404 (2005).

[28] V. A. Froltsov, R. Blaak, C. N. Likos, and H. Löwen, Phys. Rev. E **68**, 061406 (2003).

[29] B. M. Mladek, D. Gottwald, G. Kahl, M. Neumann, and C. N. Likos, Phys. Rev. Lett. **96**, 045701 (2006).

[30] C. N. Likos, Nature **440**, 433 (2006).

[31] various articles online as well as in the national press of Germany and Austria

[32] A. Jusufi, C. N. Likos, and M. Ballauff, Colloid. Polym. Sci. **282** (8), 910 (2004).

[33] P. A. Pincus, Macromolecules **24**, 2912 (1991).

[34] S. J. Miklavic, and S. Marcelja, J. Phys. Chem. **92**, 6718 (1988).

[35] S. Misra, S. Varanasi, and P. P. Varanasi, Macromolecules **22**, 5173 (1989).

[36] O. V. Borisov, T. M. Birshtein, and E. B. Zhulina, J. Phys. II **1**, 521 (1991).

[37] E. B. Zhulina, O. V. Borisov, and T. M. Birshtein, J. Phys. II **2**, 63 (1992).

[38] R. S. Ross, and P. A. Pincus, Macromolecules **25**, 2177 (1992).

[39] J. Wittmer, and J.-F Joanny, Macromolecules **26**, 2691 (1993).

[40] O. V. Borisov, E. B. Zhulina, and T. M. Birshtein, Macromolecules **27**, 4795 (1994).

[41] E. B. Zhulina, and O. V. Borisov, J. Chem. Phys. **107**, 5952 (1997).

[42] Y. Mir, P. Auvroy, and L. Auvray, Phys. Rev. Lett **75**, 2863 (1995).

[43] P. Guenoun, A. Schlachli, D. Sentenac, J. M. Mays, and J. J. Benattar, Phys. Rev. Lett. **74**, 3628 (1995).

[44] H. Ahrens, S. Förster, and C. A. Helm, Macromolecules **30**, 8447 (1997).

[45] H. Ahrens, S. Förster, and C. A. Helm, Phys. Rev. Lett. **81**, 4172 (1998).

[46] Y. Mei, K. Lauterbach, M. Hoffmann, O. V. Borisov, M. Ballauff, and A. Jusufi, Phys. Rev. Lett. **97**, 158301 (2006).

[47] F. S. Csajka, R. R. Netz, C. Seidel, and J.-F. Joanny, Eur. Phys. J. E **4**, 505 (2001).

[48] J. D. Jackson, *Classical Electrodynamics*, second edition, (Wiley, New York, 1975).

[49] N. Hoffmann, F. Ebert, C. N. Likos, H. Löwen, and G. Maret, Phys. Rev. Lett. **97**, 078301 (2006).

[50] For a recent review, see e.g., J.-P. Hansen, and H. Löwen, Ann. Rev. Phys. Chem. **51**, 209 (2000).

[51] J.-P. Hansen and I. R. McDonald, *Theory of Simple Liquids* (Academic Press, London, 1986), second ed.

[52] J.-L. Barrat and J.-P. Hansen, *Basic Concepts for Simple and Complex Liquids* (University Press, Cambridge, 2003) first ed.

[53] C.N. Likos and Ch. Mayer, private correspondence, 2003.

[54] M. P. Allen, and D. J. Tildesley, *Computer Simulation of Liquids* (Clarendon Press, Oxford, 1987).

[55] J. Lekner, Physica A **176**, 485 (1991).

[56] A. Lang, C. N. Likos, M. Watzlawek, and H. Löwen, J. Phys.: Condens. Matter **12**, 5087 (2002).

[57] S. van Teeffelen, C. N. Likos, N. Hoffmann, and H. Löwen, Europhys. Lett. **75**, 583 (2006).

[58] K. Zahn, and G. Maret G, Current Opinion in Colloid and Interface Science **4**, 60 (1999).

[59] H. Löwen, J. Phys.: Condensed Matter **13**, R415 (2001).

[60] V. A. Froltsov, C. N. Likos, and H. Löwen, J. Phys.: Condens. Matter **16**, S4103 (2004).

[61] H. Löwen, R. Messina, N. Hoffmann, C. N. Likos, C. Eisenmann, P. Keim, U. Gasser, G. Maret, R. Goldberg, and T. Palberg, J. Phys.: Condens. Matter **17**, S3379 (2005).

[62] R. Finken, A. A. Louis, and J.-P. Hansen, Phys. Rev. E **61**, R1028 (2000).

[63] A. J. Archer, C. N. Likos, and R. Evans, J. Phys.: Condens. Matter **11**, 12031 (2002), and references therein.

[64] R. P. Sear, and W. M. Gelbart, J. Chem. Phys. **110**, 4582 (1999).

[65] A. J. Archer, C. N. Likos, and R. Evans, J. Phys.:Condens. Matter **16**, L297 (2004).

[66] G. Malescio, and G. Pellicane, Nature Materials **2**, 97 (2003).

[67] A. Imperio, and L. Reatto, J. Phys.: Condens. Matter **16**, S3769 (2004).

[68] A. Imperio, and L. Reatto, J. Chem. Phys. **124**, 164712 (2006).

[69] G. Stell, J. Stat. Phys. **78**, 197 (1995).

[70] W. T. Góźdź, and R. Evans, J. Chem. Phys. **118**, 3702 (2003).

[71] M. Seul, and D. Andelman, Science **267**, 476 (1995).

[72] T. Stirner, and J. Sun, Langmuir **21**, 6636 (2005).

[73] Y. Liu, W.-R. Chen, and S.-H. Chen, J. Chem. Phys. **122**, 044507 (2005).

[74] B. M. Mladek, D. Gottwald, G. Kahl, M. Neumann, and C. N. Likos, Phys. Rev. Lett. **96**, 045701 (2006).

[75] S. Mossa, F. Sciortino, P. Tartaglia, and E. Zaccarelli, Langmuir **20**, 10756 (2004).

[76] F. Sciortino, S. Mossa, E. Zaccarelli, and P. Tartaglia, Phys. Rev. Lett. **93**, 055701 (2004).

[77] R. P. Sear, S.-W. Chung, G. Markovich, W. M. Gelbart, and J. R. Heath, Phys. Rev. E **59**, R6255 (1999).

[78] C. N. Likos, K. R. Mecke, and H. Wagner, J. Chem. Phys. **102**, 9530 (1995).

[79] K. R. Mecke, and D. Stoyan, in *Statistical Physics and Spatial Statistics, the Art of Analyzing and Modeling Spatial Structures and Pattern Formation* (Springer Lecture Notes in Physics **554**, Springer, Berlin, 2000).

[80] DYNABEADS M-450, uncoated; Deutsche Dynal GmbH, Postfach 111965, D-20419 Hamburg, Germany.

[81] F. J. Rogers and D. A. Young, Phys. Rev. A **30**, 999 (1984).

[82] C. N. Likos, and N. W. Ashcroft, J. Chem. Phys. **97**, 9303 (1992).

[83] T. Biben and J.-P. Hansen, J. Phys.: Condens. Matter **3**, F65 (1991).

[84] J. M. Caillol, D. Levesque, and J. J. Weiss, Mol. Phys. **44**, 733 (1981).

[85] A. Stradner, H. Sedgwick, F. Cardinaux, W. C. K. Poon, S. U. Egelhaaf, and P. Schurtenberger, Nature **432**, 492 (2004).

[86] R. Roth and R. Evans, Europhys. Lett. **53**, 271 (2001).

[87] N. W. Ashcroft, and D. D. Langreth, Phys. Rev. **156**, 685 (1967).

[88] H. N. W. Lekkerkerker, W. C. K. Poon, P. N. Pusey, A. Stroobants, and P. B. Warren, Europhys. Lett. **20**, 559 (1992).

[89] P. H. Fries and G. N. Patey, J. Chem .Phys. **82**, 429 (1985).

[90] F. Lado, J. Comput. Phys. **8** , 417 (1971).

[91] M. Abramowitz and I. A. Stegun, *Handbook of Mathematical functions* (Dover Publications, Inc., New York, 1972).

[92] J. Li, J. Comput. Anal. Appl. **183**, 29 (2005).

[93] F. Lado, Mol. Phys. **2**, 283 (1982).

[94] E. J. W. Verwey, and J. T. G. Overbeek, *Theory of the Stability of Lyophobic Colloids* (Amsterdam: Elsevier, 1948).

[95] See, e.g., J. Dzubiella, and J.-P. Hansen, J. Chem. Phys. **119**, 1204 (2003).

[96] E. Allahyarov, H. Löwen, J.-P Hansen, and A. A. Louis, Phys. Rev. E **67**, 051404 (2003).

[97] D. G. Rowan, J.-P. Hansen, and E. Trizac, Mol. Phys. **98**, 1369 (2000).

[98] E. Trizac, L. Bocquet, R. Agra, J.-J Weis, and M. Aubouy, M., J. Phys.: Condens. Matter **14**, 9339 (2002).

[99] B. J Yoon, and A. M. Lenhoff, J. Phys. C **96**, 3130 (1992).

[100] D. J. Roush, D. S. Gill, and R. C. Wilson, Biophys. J. **66**, 1290 (1994).

[101] M. L. Grant, J. Phys. Chem. B **105**, 2858 (2001).

[102] R. B. McClurg, and C. F. Zukoski, J. Colloid Interface Sci. **208**, 529 (1998).

[103] A. Striolo, D. Bratko, J. Z. Wu, N. Elvassore, H. W. Blanch, and J. M. Prausnitz, J. Chem. Phys. **116**, 7733 (2002).

[104] R. Messina, J. Chem. Phys. **117**, 11062 (2002).

[105] A. Jusufi, C. N. Likos, and H. Löwen, J. Chem. Phys. **116**, 11011 (2002).

[106] H. Schiessel, and P. A. Pincus, Macromolecules **31**, 7953 (1998).

[107] N. V. Brilliantov, D. V. Kuznetsov, and R. Klein, Phys. Rev. Lett. **81**, 1433 (1998).

[108] D. H. Napper, *Polymeric Stabilization of Colloidal Dispersions* (Academic Press, New York, 1983).

[109] X. Guo, and M. Ballauff, Langmuir **16**, 8719 (2000).

[110] P.-G. de Gennes, Macromolecules **13**, 1069 (1980).

[111] S. Alexander, J. Phys. **38**, 983 (1977).

[112] T. M. Birshtein, and E. B. Zhulina, Polymer **25**, 1453 (1984).

[113] O. V. Borisov, E. B. Zhulina, and T. M. Birshtein, Polym. Sci. USSR (Engl. Transl.) **30**, 772 (1988).

[114] P. Auroy, L. Auvray, and L. Leger, J. Phys.: Condens. Matter **2**, SA317 (1992).

[115] P. Auroy, L. Auvray, and L. Leger, Phys. Rev. Lett. **66**, 719 (1991).

[116] P. Auroy, L. Auvray, and L. Leger, Macromolecules **24**, 2523 (1991).

[117] F. Oosawa, *Polyelectrolytes* (Marcel Dekker, New York, 1971).

[118] N. Grønbech-Jensen, R. J. Mashl, R. F. Bruinsma, and W. M. Gelbart, Phys. Rev. Lett. **78**, 2477 (1997).

[119] M. J. Stevens, and K. Kremer, J. Chem. Phys. **103**, 1669 (1995).

[120] R. G. Winkler, M. Gold, and P. Reineker, Phys. Rev. Lett. **80**, 3731 (1998).

[121] H. Schiessel, and P. A. Pincus, Macromolecules **25**, 2177 (1992).

[122] S. Kirkpatrick, C. D. Gelatt, and M. P. Vecchi, Science **220**, 671 (1983).

[123] E. Aarts, and J. Korst, *Simulated Annealing and Boltzmann Machines* (Anchor Press, Tiptree, 1989).

[124] P. J. M. van Laarhoven, and E. Aarts, *Simulated Annealing: Theory and Applications* (D. Reidel Publishing Company, Dordrecht, 1987).

[125] N. Metropolis, A. Rosenbluth, M. Rosenbluth, A. Teller, E. Teller, J. Chem. Phys. **21**, 1087 (1953).

[126] C. D. Santangelo, and A. W. C. Lau, Eur. Phys. J. E **13**, 335 (2004).

[127] P.-G. deGennes, *Scaling Concepts in Polymer Physics* (Cornell University Press, Ithaca, 1979).

[128] M. Doi, *Introduction to Polymer Physics* (Clarendon Press, Oxford, 1996).

[129] J. N. Israelachvili, *Intermolecular and Surface Forces* (Academic Press, London, 1985).

[130] N. Hoffmann, C. N. Likos, and H. Löwen, J. Phys.: Condens. Matter **18**, 10193 (2006).

[131] N. Hoffmann, C. N. Likos, and H. Löwen, (in preparation) (2006).

[132] N. Hoffmann, C. N. Likos, and J.-P. Hansen, Mol. Phys. **102**, 857 (2004).

[133] N. Hoffmann, and P. A. Pincus, (in preparation) (2006).

Acknowledgments

I would like to deeply thank the various people who, during the last three years in which this work lasted, provided me with useful and helpful assistance. Without their care and consideration, this this would likely not have matured.

It is a great pleasure to express my respect and sincere gratitude to Prof. C. N. Likos for his immense support and guidance during the course of this work. He is the best adviser and teacher I could wished for, and clearly always had my best interest in mind. His enthusiasm and hard-working nature has inspired everyone in our group, but especially me. I cannot thank him enough for being patient and understanding whenever I approached him with any doubts or queries. I thank him for his keen interest in my academic as well as in my personal welfare.

I am extremely grateful to Prof. H. Löwen for the opportunity to work at his institute. He was always actively involved in my ongoing work and our discussions had have benefited me immensely. His ideas and advice have contributed to the success of this work.

I thank Prof. P. A. Pincus for hosting and supervising me at his institute in Santa Barbara, USA. It has been a tremendous learning experience for me to work with him.

I want to express my sincere thank to Prof. J.-P. Hansen for a great collaboration and numerous discussions on many conferences. It was a honor to work with him.

I have been fortunate to have had excellent colleagues I have worked with. I thank them for a number of answered questions and a congenial working atmosphere.

I owe special thank to Ch. Mayer and M. Konieczny with whom I was honored to share the office during my Ph. D. stint. Innumerous fruitful discussions have significantly contributed to a successful completion of this work. I am glad to call them my friends.

I have wonderful friends who have enriched my life in many different respects and never made me realize how the past three years have flown by. I always could rely on them.

Most important, I thank my family for all their love and support that they had given to me. They have always kept me grounded and encouraged me through all my career.

I gratefully acknowledge for financial support from the DAAD giving me the opportunity to work partly in the USA.

Die hier vorgelegte Dissertation habe ich eigenständig und ohne unerlaubte Hilfe angefertigt. Die Dissertation wurde in der vorgelegten oder in ähnlicher Form noch bei keiner anderen Institution eingereicht. Ich habe bisher keine erfolglosen Promotionsversuche unternommen.

Düsseldorf, den 01.12.2006

(Norman Hoffmann)